A Search for Third Generation Leptoquarks in $p\bar{p}$ Collisions at $\sqrt{s} = 1.8$ TeV

A thesis presented

by

Thomas Patrick Baumann

to

The Department of Physics

in partial fulfillment of the requirements

for the degree of

Doctor of Philosophy

in the subject of

Physics

Harvard University

Cambridge, Massachussetts

May, 1996

A Search for Third Generation Leptoquarks
in $p\bar{p}$ Collisions at $\sqrt{s} = 1.8$ TeV

Thomas Patrick Baumann

Adviser: Melissa E. B. Franklin

Abstract

This thesis presents the results of a search for third generation leptoquarks in 72 pb^{-1} of $p\bar{p}$ collisions at $\sqrt{s} = 1.8$ TeV. The data were collected at the Collider Detector at Fermilab (CDF) during the 1992–1995 Collider runs. Leptoquarks (LQ) are spin-0 or spin-1 particles which couple both to a quark and a lepton. Third generation leptoquarks are assumed to be produced in pairs and each to decay to a tau lepton + b quark with a branching ratio β. The signature for leptoquarks investigated here is two taus plus two jets. Events with tau pairs are identified by the presence of a collimated high momentum jet, a high momentum electron or muon, and missing energy close to the lepton and transverse to the beam. At least two jets are required to reduce the background from QCD production of Z° bosons with associated jets and $Z^\circ \to \tau^+\tau^-$. No evidence for a leptoquark signal is observed. Upper limits on $\sigma(p\bar{p} \to \mathrm{LQ}\,\overline{\mathrm{LQ}}) \times \beta^2$ are obtained as a function of M_{LQ} for scalar and vector leptoquarks. Using theoretical predictions for leptoquark pair production cross sections, scalar leptoquarks are excluded for $M_{LQ} < 94$ GeV/c^2, non-gauge vector leptoquarks are excluded for $M_{LQ} < 165$ GeV/c^2, and gauge vector leptoquarks are excluded for $M_{LQ} < 220$ GeV/c^2 for $\beta = 100\%$ at the 95% C.L. Non-gauge vector leptoquarks are excluded for $M_{LQ} < 120$ GeV/c^2, and gauge vector leptoquarks are excluded for $M_{LQ} < 178$ GeV/c^2 for $\beta = 50\%$ at the 95% C.L. The data do not constrain scalar leptoquarks for $\beta = 50\%$ at the 95% C.L.

Contents

Acknowledgements xiv

1 Introduction and Theory 1

1.1 Aspects of the Standard Model 2

1.2 Leptoquark Theory 5

1.2.1 Overview 5

1.2.2 Leptoquark Couplings 6

1.2.3 Leptoquark Search Channel 8

1.2.4 Experimental Constraints on Leptoquarks 11

1.2.5 Bounds from Direct Searches 11

1.2.6 Indirect Bounds 12

1.2.7 Leptoquark Production 14

1.2.8 Pair Production Cross Section 17

2 The CDF Experiment 22

2.1 The Accelerators 22

2.2 Overview of the CDF Detector 24

2.3 Tracking Systems 28

2.4 Calorimeters 30

2.5 Muon Systems 36

2.6 Trigger 42

3 Data Reconstruction and Lepton Identification **47**

3.1 Calorimeter Energy 48

3.2 Jet Reconstruction 48

3.2.1 Jet Clustering Algorithm 48

3.3 Central Electrons 49

3.3.1 Electron Clustering Algorithm 50

3.3.2 Electron Variable Definitions 51

3.3.3 Electron Fiducial Region 52

3.3.4 Energy Corrections 55

3.3.5 Electron Identification Criteria and Efficiencies 57

3.4 Central Muons 58

3.4.1 Muon Variable Definitions 61

3.4.2 Muon Identification Criteria and Efficiencies 62

3.5 Hadronic Tau Reconstruction: Taujets 68

3.5.1 Taujet Variable Definitions 69

3.5.2 Taujet Fiducial Region 71

3.5.3 Taujet Identification Requirements 72

3.6 Neutrino Reconstruction 73

4 Leptoquark Search **83**

4.1 Data Sets 83

4.2 Lepton + Taujet Selection 83

4.3 Isolation Requirements 85

4.4 $Z \rightarrow ee$ and $Z \rightarrow \mu\mu$ Removal 86

4.5 $\not\!\!E_t$ Direction: Di-tau Selection 91

4.6 Number of Jets: Leptoquark Selection 98

4.7 Features of the Di-tau Candidate Sample 100

5 Background Estimation **109**

5.1 Overview of Method 109
5.2 Background Estimates from Monte Carlo Simulations 112
5.2.1 $Z \rightarrow \tau\tau + \geq n$ Jets 115
5.2.2 Drell Yan: $\gamma^* \rightarrow \tau\tau$ 116
5.2.3 Top Quark Pair Production 116
5.2.4 Diboson Production: WW, WZ, ZZ 117
5.2.5 Bottom Quark Pair Production 118
5.2.6 W + Jets Production, $W \rightarrow \ell\nu$ 119
5.2.7 Summary of Backgrounds 121
5.3 Assumptions in the Method 122

6 Signal Efficiencies and Systematic Errors **125**
6.1 Signal Efficiency 125
6.1.1 Acceptance for Scalar Leptoquarks Pairs 127
6.1.2 Acceptance for Vector Leptoquarks Pairs 128
6.1.3 Lepton Identification and Trigger Efficiencies 137
6.2 Systematic Errors 141
6.2.1 Initial State Radiation 141
6.2.2 Choice of Q^2 Scale 142
6.2.3 Energy Scale Uncertainty 143
6.2.4 Integrated Luminosity 143
6.2.5 Structure Functions 144
6.2.6 Tau Branching Ratios 144
6.2.7 Sample Statistics 144
6.2.8 ε-Scaling Procedure for Vector Leptoquarks 145
6.2.9 Total Systematic Error 145

7 Results **147**
7.1 Bounds on Leptoquark Cross Section 147

7.2 Bounds on Leptoquark Mass 149

8 Conclusions **155**

Bibliography **157**

List of Figures

1.1 Triangle anomaly 3
1.2 The lowest-order Feynman diagrams for leptoquark-fermion couplings 5
1.3 Leptoquark-induced proton decay 6
1.4 Flavor-changing neutral current decay of K^- induced by leptoquarks 6
1.5 Leptoquark-induced corrections to the $Z \to f\bar{f}$ vertex 14
1.6 The lowest order Feynman diagrams for single leptoquark production in qg collisions 16
1.7 The leading order Feynman diagrams for $gg \to LQ\overline{LQ}$, continuum . . 16
1.8 The leading order Feynman diagrams for $q\bar{q} \to LQ\overline{LQ}$, continuum . . 17
1.9 Theoretical cross sections for scalar and vector leptoquark pair production 20
1.10 Feynman diagrams for resonant leptoquark pair production 21

2.1 A schematic of the Tevatron and associated accelerators 23
2.2 Isometric view of the CDF Detector 25
2.3 Quarter view of the CDF Detector 26
2.4 A schematic of the Central Tracking Chamber (CTC) endplate 29
2.5 The calorimeter tower projective segmentation 31
2.6 A cutaway view of a central calorimeter wedge 32
2.7 Schematic view of a central wedge, showing the Central Muon Chambers (CMU) 37
2.8 A cross section of a single CMU tower 39

2.9 A schematic map of the CDF cental muon coverage 40
2.10 A schematic view of a 15° wedge of the Central Muon Extension (CMX) 41

3.1 Central electron identification variables from $Z \rightarrow ee$ events in Run 1A data 53
3.2 Central electron identification variables from $Z \rightarrow ee$ events in Run 1B data 54
3.3 CEM tower response map 55
3.4 Muon isolation in simulated $b\bar{b}$ events 60
3.5 Central muon (CMU/P) identification variables from $Z \rightarrow \mu\mu$ events in Run 1A data 63
3.6 Central muon (CMU/P) identification variables from $Z \rightarrow \mu\mu$ events in Run 1B data 64
3.7 Central muon (CMX) identification variables from $Z \rightarrow \mu\mu$ events in Run 1B data 65
3.8 Distributions of hadronic tau (taujet) identification variables from simulated leptoquark events 74
3.9 Distributions of hadronic tau (taujet) identification variables from simulated leptoquark events 75
3.10 Distributions of hadronic tau (taujet) identification variables from jets in a lepton + jet control sample (data) 76
3.11 Distributions of hadronic tau (taujet) identification variables from jets in a lepton + jet control sample (data) 77
3.12 Efficiencies of the taujet identification criteria for control sample jets (data) and for jets from simulated hadronic tau decays 78
3.13 Efficiencies of the taujet identification criteria for control sample jets (data) and for jets from simulated hadronic tau decays 79
3.14 Efficiencies of the taujet identification criteria for control sample jets (data) and for jets from simulated hadronic tau decays 80

4.1 Lepton Isolation distributions in lepton + taujet events in data and simulated leptoquark events 87
4.2 Taujet Isolation distributions in lepton + taujet events in data and simulated leptoquark events 88
4.3 Mass of lepton and leading taujet track: $Z \rightarrow ee$ and $Z \rightarrow \mu\mu$ Removal 89
4.4 $\not\!\!E_t$ distributions from leptoquark, $Z \rightarrow \tau\tau$, and W + jets MC, and in the lepton + taujet data 92
4.5 $\Delta\phi(\ell, \not\!\!E_t)$ distributions from leptoquark, and $Z \rightarrow \tau\tau$, and W + jets MC 93
4.6 $S/\sqrt{B}$ versus maximum $\Delta\phi(\ell, \not\!\!E_t)$: Di-tau selection 95
4.7 $\Delta\phi(\ell, \not\!\!E_t)$ distributions in the lepton + taujet data 96
4.8 Taujet track multiplicity after the di-tau selection, data and MC . . . 98
4.9 Two diagrams for $\mathcal{O}(\alpha_s)$ Z production 99
4.10 The leading jet E_t distributions in simulated $Z \rightarrow \tau\tau$ and leptoquark events 101
4.11 The jet multiplicity in simulated $Z \rightarrow \tau\tau$ and leptoquark events 101
4.12 Inclusive jet multiplicity and leading jet E_t in di-tau candidate events 103
4.13 Kinematic quantities of $Z \rightarrow \tau\tau$ candidates I 105
4.14 Kinematic quantities of $Z \rightarrow \tau\tau$ candidates II 106
4.15 Kinematic quantities of $Z \rightarrow \tau\tau$ candidates III 107
4.16 Kinematic quantities of $Z \rightarrow \tau\tau$ candidates IV 108

5.1 $\not\!\!E_t$ distributions in simulated leptoquark events, SS lepton + taujet data, and two data samples dominated by QCD-multijet events . . . 113
5.2 Two diagrams for $\mathcal{O}(\alpha_s)$ W production 120

6.1 The lepton plus taujet selection efficiencies from simulated scalar leptoquark events 130
6.2 The efficiencies of the leptoquark selection criteria determined from simulated scalar leptoquark events 131

6.3 The total acceptance for scalar leptoquark pairs determined from simulated leptoquark events 132
6.4 Generator-level η and p_t of scalar and vector leptoquarks 134
6.5 The efficiency for finding a Level 2 jet associated with an offline jet . 138
6.6 The clustering efficiency for the Level 2 16 GeV central electron trigger 138

7.1 Theoretical cross section and experimental bounds for leptoquark pair production assuming $\beta = \mathrm{BR}(\mathrm{LQ} \to \tau b) = 100\%$. 153
7.2 Theoretical cross section and experimental bounds for leptoquark pair production assuming $\beta = \mathrm{BR}(\mathrm{LQ} \to \tau b) = 50\%$. 154

List of Tables

1.1 The three generations of fermions 2

1.2 The $Z^\circ \to f\bar{f}$ vertex factors in the Standard Model. 4

1.3 The major tau decay channels and the world average branching ratios. 9

3.1 Electron identification requirements 56

3.2 Electron identification efficiencies from the $Z \to ee$ samples 58

3.3 Muon identification criteria 62

3.4 Central muon identification efficiencies from the $Z \to \mu\mu$ samples. . . 66

3.5 Taujet identification requirements and efficiencies from simulated leptoquark events ($M_{LQ} = 125$ GeV/c^2) 71

4.1 Integrated luminosities of inclusive lepton samples 84

4.2 The breakdown by track multiplicity of lepton + taujet events passing $\Delta\phi(\ell, \not\!\!E_t) < 50^\circ$ 97

4.3 Lepton plus taujet yield in data 102

5.1 Lepton plus taujet sources 110

5.2 Estimates for opposite-sign lepton plus taujet events 122

5.3 The excess of opposite-sign lepton + taujet events 123

6.1 Lepton plus taujet selection efficiencies for simulated scalar leptoquark pairs 129

6.2 The efficiencies of the leptoquark requirements from simulated scalar leptoquark events 129
6.3 Scale factors for vector leptoquark efficiencies 136
6.4 Identification efficiencies for isolated leptons determined from $Z \to \ell\ell$ data 136
6.5 Level 2 Lepton Trigger Efficiencies 139
6.6 Detection efficiency for scalar leptoquarks 141
6.7 Systematic uncertainties 146

7.1 Summary of scalar and vector leptoquark results. 150

Acknowledgements

I am amazed that I have writer's block even at this point in my thesis. There. Now that I'm over that hurdle, I would like to acknowledge and thank the efforts of the CDF Collaboration and Fermilab physicists and technical staff for making this work possible. An enormous debt of gratitude goes to my advisor, Melissa Franklin. Her encouragement and guidance throughout my graduate years were invaluable. Melissa, Jaco Konigsberg, Colin Gay, and Jorge Trocóniz taught me a tremendous amount of physics. I thank each of them deeply.

Graduate school would have been bleak without the friends I've made along the way. Georgios Archontis and Fotis Ptohos (especially) were there from the beginning, and I hope they will continue to be so in the future. Peter Hurst was and is a phenomenon. Young-Kee Kim and Tom Imbo always welcomed me with warm hospitality. My fellow Harvard/CDFer's are great for a laugh, some drinks, good food, ...: Rowan Hamilton, Colin Jessop, Tom Dignan, Andrew Gordon, David Kestenbaum, Jorge Trocóniz, and the rest of the Greek triumvirate, Georgios Michail and Maria Spiropulu ($\kappa o \lambda o \kappa \eta \theta \omega \kappa \epsilon \phi \tau \epsilon \delta \epsilon \varsigma$, pardon my French). The good humor and determination of Robin Coxe is awe inspiring.

The people at HEPL make the lab a pleasant place to work. A special thanks goes to George Brandenburg who initiated me into the CDF group. The rest of the HEPL staff are always there for conversation, refreshments, and encouragement.

Two gems must not go unmentioned: Alma Karas who coached me in volleyball and bridge; and Carol Davis who often lent an ear and a comfy chair.

Eva, John, Mark and Erika remain close despite the years and miles.

Lastly but most importantly, I must thank my wonderful family for their unconditional support and love during my stint on the East Coast. Mom, Dad, Mike, Maggie, Christine, Whitney, Kathy, Pat, Jessica, Ali, Tim, Eddie, Ann, Scott, Ryan, Josh, Jeremy, Mary, Bert, Julia, and Audrey all helped to keep things in perspective. We'll have to find a substitute destination for the "annual trips to Boston."

Chapter 1

Introduction and Theory

Symmetries exist in many forms in nature. Symmetries play a profound role in physical laws and the interactions they govern. Conservation laws in physics are attributable to symmetries within a physical system. There are several examples of this in classical physics. Rotational symmetry within a system implies that angular momentum is conserved. Similarly, in a system symmetric under translations in time, energy is conserved. This thesis explores the possibility of a symmetry between quarks and leptons.

Quarks and leptons are elementary spin-$\frac{1}{2}$ particles (fermions). The fermions can be grouped into three generations or families. These are listed by increasing mass in Table 1.1. The leptons, electrons e, muons μ, taus τ, and the associated neutrinos ν_e, ν_μ, ν_τ, carry integer values of electric charge charge, while the quarks, up u, down d, charm c, strange s, bottom b, and top t, carry fractional electric charge. Quarks carry an additional degree of freedom called color, which is labeled red, green, or blue. Ordinary matter (protons, neutrons, atoms) is made up of first generation fermions, e, u, d, while the heavier quarks, c, s, b, t, exist only as unstable matter which decays into the lighter quarks or leptons.

Particles interact through the four known forces: the strong, electromagnetic, weak, and gravitational forces. The strong force mediates interactions between par-

Fermions, Spin-$\frac{1}{2}$			
Leptons			Q
$\begin{pmatrix} \nu_e \\ e \end{pmatrix}$	$\begin{pmatrix} \nu_\mu \\ \mu \end{pmatrix}$	$\begin{pmatrix} \nu_\tau \\ \tau \end{pmatrix}$	$\begin{matrix} 0 \\ -1 \end{matrix}$
Quarks			
$\begin{pmatrix} u \\ d \end{pmatrix}$	$\begin{pmatrix} c \\ s \end{pmatrix}$	$\begin{pmatrix} t \\ b \end{pmatrix}$	$\begin{matrix} \frac{2}{3} \\ -\frac{1}{3} \end{matrix}$

Table 1.1: The three generations of fermions

ticles which carry color. It acts over a short range to bind quarks into baryon (qqq), and meson ($q\bar{q}$) bound states. Mesons and baryons are known collectively as hadrons. The strong force is also responsible for the nuclear force which binds protons and neutrons to form nuclei. The electromagnetic force mediates interactions between charged particles. Electrons and nuclei are held together by the electromagnetic force which is responsible for the chemical and physical properties of bulk matter. The quarks and leptons are subject to the weak force which governs such processes as the beta decay of neutrons and the decays of long-lived hadrons like charged pions or kaons. Gravity is the weakest of the four forces and is negligible in the interactions between particles at accelerator energies.

1.1 Aspects of the Standard Model

The strong interaction is described by the theory of Quantum Chromodynamics (QCD) [1]. The electromagnetic and weak interactions are described by the Glashow–Weinberg–Salam theory of electroweak processes [2, 3, 4]. Together these theories are known collectively as the Standard Model. In the Standard Model, all interactions be-

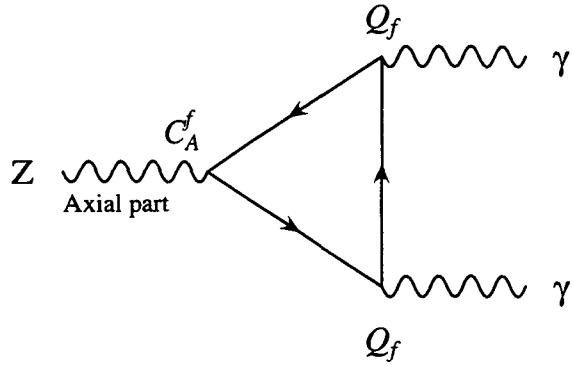

Figure 1.1: An example of a fermion triangle which could cause anomaly. The fermion axial coupling to the Z,c_A^f, is given by T_L^3, the third component of weak isospin. Q_f is the fermion charge. The sum over each generation of fermions for this diagram must vanish for the electroweak theory to be renormalizable.

tween particles derive from *local gauge symmetries* [5] and are mediated by the gauge bosons[1]. QCD is based on the symmetry group SU(3). The eight massless gluons (g) are the gauge bosons of QCD. The electroweak theory is based on an SU(2)×U(1) symmetry. Through the Higgs mechanism of spontaneous symmetry breaking [6], the gauge fields of the electroweak theory are separated into the massless photon (γ) and the massive W^+, W^-, and Z° bosons. In its simplest form, the spontaneous symmetry breaking requires the existence of a spin-0 neutral Higgs boson (H°). The Higgs boson together with the quarks, leptons, gauge bosons make up the fundamental particles of the Standard Model. So far there is no experimental evidence for the Higgs boson.

The quarks and leptons interact with each other indirectly through the gauge bosons. But there are no direct couplings with a quark, a lepton, and a boson in the Standard Model (as in Figure 1.2). However, there is an apparent symmetry between the quark and lepton sectors. The three families of leptons are paired with three families of quarks. This serves a purpose apart from aesthetics; it keeps the electroweak theory renormalizable. The integral represented by the Feynman diagram in

[1]Bosons are particles which have integer spin. The gauge bosons have spin-1.

Fermions	T_L^3	Q_f	c_A^f	c_V^f
ν_e, ν_μ, ν_τ	$\frac{1}{2}$	0	$\frac{1}{2}$	$\frac{1}{2}$
e^-, μ^-, τ^-	$-\frac{1}{2}$	-1	$-\frac{1}{2}$	$-\frac{1}{2}+2\sin\theta_W$
u, c, t	$\frac{1}{2}$	$\frac{2}{3}$	$\frac{1}{2}$	$\frac{1}{2}-\frac{4}{3}\sin\theta_W$
d, s, b	$-\frac{1}{2}$	$-\frac{1}{3}$	$-\frac{1}{2}$	$-\frac{1}{2}+\frac{2}{3}\sin\theta_W$

Table 1.2: The $Z^\circ \rightarrow f\bar{f}$ vertex factors in the Standard Model. The terms c_A^f and c_V^f are the axial-vector and vector couplings in the weak neutral current. c_A^f is given by T_L^3, the third component of weak isospin. c_V^f is given by $T_L^3 - 2\sin^2\theta_W Q_f$ where $\sin\theta_W$ is the weak mixing angle, and Q_f is the fermion charge.

Figure 1.1 diverges in a manner that can spoil the renormalizability of the Standard Model. This is called an anomaly. However, each fermion contributes a term proportional to $c_A^f Q_f^2$ to the integral, where c_A^f is the axial coupling of the weak neutral current and Q_f is the charge. The values of c_A^f and Q_f for the fermions are listed in Table 1.2. Therefore each generation of fermions contributes a term proportional to

$$\left[\frac{1}{2}N_c\left(+\frac{2}{3}\right)^2 - \frac{1}{2}N_c\left(-\frac{1}{3}\right)^2 + \frac{1}{2}(0)^2 - \frac{1}{2}(-1)^2\right] = 0 \qquad (1.1)$$

where $N_c = 3$ is the number of colors. So for three doublets of quarks and three doublets of leptons, the integral vanishes due to the cancellations among the fermions. This remarkable feature suggests a deeper connection between quarks and leptons. It would seem plausible then to have a higher symmetry which encompasses both the quark and lepton sectors. Theories based on such a symmetry would naturally contain transitions between quarks and leptons, mediated by particles called leptoquarks. This thesis describes a search for third generation leptoquarks which couple to the tau lepton and bottom quark.

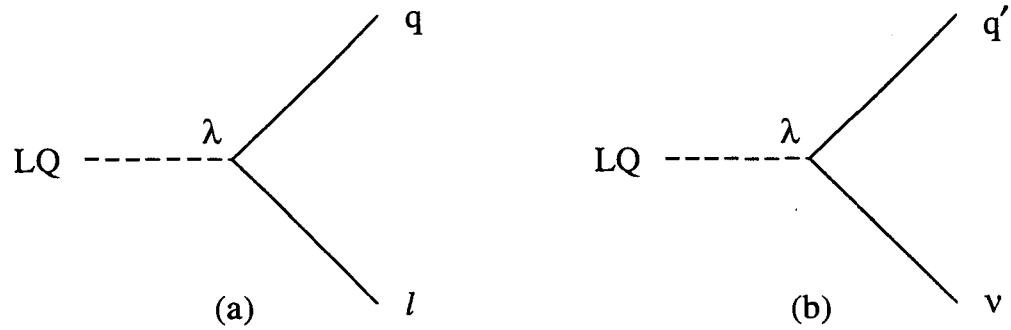

Figure 1.2: The coupling of leptoquarks to quark and lepton pairs. The Yukawa coupling strength is given by λ. The leptoquark quantum numbers determine the direction of the arrows on the fermion lines. In this analysis, leptoquarks which couple to $\tau^- b$ or $\tau^- \bar{b}$ pairs are considered.

1.2 Leptoquark Theory

1.2.1 Overview

"Leptoquark" is a generic term for color-triplet bosons which couple both to a quark and a lepton (Figure 1.2). Although leptoquarks are not predicted by the Standard Model, they appear in many extensions to the Standard Model which join the quark and lepton sectors at a more fundamental level. In grand unification models (GUT's) [7, 8], leptoquarks may couple both to $q\ell$ and qq' pairs and mediate proton decay (Figure 1.3) and flavor changing neutral current (FCNC) processes [19]. The predicted masses of such bosons are on the order of the unification scale, 10^{15} GeV for SU(5) GUT's. In models of compositeness [9, 10, 11], some or all of the "elementary" particles in the Standard Model are composed of a common set of constituents called preons. The preons can combine to form scalar or vector leptoquarks. In various hybrids of technicolor [12, 13, 14], leptoquarks appear as scalar bound states of a technilepton and a techniquark. The coupling strength of this type of leptoquark to ordinary matter is generally proportional to mass, so the leptoquark decays preferen-

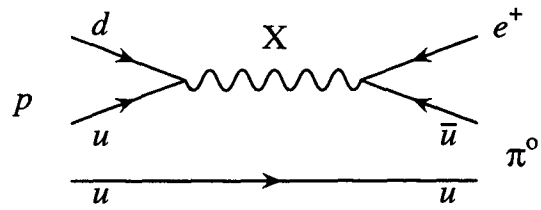

Figure 1.3: One of the Feynman diagrams describing the proton decay reaction, $p \to e^+\pi^\circ$, predicted by SU(5) grand unified theories. The decay is mediated by the X boson which has leptoquark and diquark couplings.

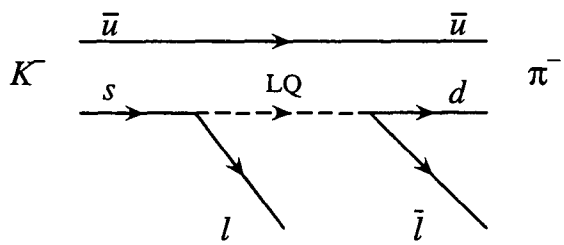

Figure 1.4: The flavor-changing neutral current decay, $K^- \to \pi^-\ell\bar{\ell}$, can be induced by leptoquarks which couple to more than one generation of quarks. Such leptoquarks are constrained to be very massive by the experimental bounds for this process.

tially to third generation fermions. [2]

1.2.2 Leptoquark Couplings

The theories mentioned above make specific predictions about leptoquark masses, couplings and quantum numbers. In most cases, the leptoquarks in these theories are either too massive to be directly observed at accelerator experiments or indirectly constrained by experimental limits on rare processes.

[2]In general, we refer to third generation leptoquarks as those coupling to third generation quarks and third generation leptons (and similarly for first and second generation leptoquarks). In the few cases where we discuss leptoquarks which couple to different generations of leptons and quarks, the generation of the leptoquark is that of the lepton.

Alternatively one can consider leptoquarks independent of any specific model. One approach is to formulate the most general lagrangian for fermion-leptoquark couplings that respects the Standard Model symmetries SU(3)×SU(2)×U(1) [31]. The resulting leptoquarks have a variety of quantum numbers: spin 0 or 1; electric charge $\frac{1}{3}$, $\frac{2}{3}$, $\frac{4}{3}$ or $\frac{5}{3}$; weak isospin 0, $\frac{1}{2}$ or 1. In this analysis, leptoquarks with spin 0 and 1 and $|Q| = \frac{2}{3}$ and $\frac{4}{3}$ are considered. These are quantum numbers of leptoquarks which couple to $\tau^- b$ or $\tau^- \bar{b}$.

Leptoquarks decay via the diagrams in Figure 1.2. Depending on the leptoquark quantum numbers, both or only one of the channels may be allowed. In this analysis, leptoquarks coupling to $\tau^- b$ or $\tau^- \bar{b}$ are considered. A third generation leptoquark with charge $\frac{4}{3}$ can decay only to $\tau^- b$. A charge-$\frac{2}{3}$ leptoquark may decay to $\tau^- \bar{b}$ and in some cases $\nu_\tau \bar{t}$ [31]. The latter decay mode may be kinematically forbidden leptoquarks if $M_{LQ} < M_{top}$.

The partial decay widths into each mode are given by Equations 1.2 and 1.3

$$\Gamma(\text{scalar}) = \frac{1}{16\pi}\lambda^2 M_{LQ} \tag{1.2}$$

$$\Gamma(\text{vector}) = \frac{1}{24\pi}\lambda^2 M_{LQ} \tag{1.3}$$

for $M_{LQ} \gg M_\ell, M_q$. It is assumed $\lambda \gtrsim 10^{-7}$ so that the leptoquarks decay within the detector volume. This is not a severe assumption since for an electroweak coupling strength, $\lambda = \frac{e}{\sin\theta_W} \sim 0.7$. The branching fraction $\beta \equiv BR(\text{LQ} \to \ell^\pm q)$ is given by

$$\beta = \frac{\Gamma(\text{LQ} \to \ell^\pm q)}{\Gamma_{tot}} \tag{1.4}$$

where Γ_{tot} is the total width into the available LQ decay channels. The possible branching ratios are $\beta = 0, 50\%$, or 100%, for $M_{LQ} \gg M_\ell, M_q$. If both leptoquark decay channels are open ($\nu\bar{t}$ and $\tau^-\bar{b}$), the $\nu\bar{t}$ channel will be phase-space suppressed for $M_{LQ} \sim m_{top}$. Therefore the branching fraction $\beta = BR(\text{LQ} \to \tau^-\bar{b})$ will be

somewhat larger than 50%. For generality, values of the branching ratio other than 50% and 100% will also be considered in this analysis.

Direct searches for leptoquarks at e^+e^- and $p\bar{p}$ colliders have concentrated on signatures for LQ pairs. For first and second generation leptoquarks ($\ell = e, \mu$), the possible LQ $\overline{\text{LQ}}$ final states are

	LQ $\overline{\text{LQ}}$ Decay Products	LQ $\overline{\text{LQ}}$ Signature
(i)	$q \quad \nu \quad \bar{q} \quad \bar{\nu}$	$jet + jet + \not{E}_t$
(ii)	$q \quad \ell^{\pm} \quad q' \quad \nu$	$jet + \ell^{\pm} + jet + \not{E}_t$
(iii)	$q \quad \ell^+ \quad \bar{q} \quad \ell^-$	$jet + \ell^+ + jet + \ell^-$

The quarks from the leptoquark decays fragment into a jets of hadrons. The neutrinos pass through the experimental apparatus undetected, so their presence is inferred by an imbalance of detected energy, denoted by $\not{E}_t$ or $\not{p}$, missing transverse energy or missing momentum respectively.[3] For third generation leptoquarks, if $M_{LQ} < M_{top}$ only signatures (i) and (iii) are kinematically accessible. The signatures when $M_{LQ} > M_{top}$ are complicated by the decays of the top quark — this scenario is not addressed here. In this analysis, third generation leptoquarks pairs decaying to τb or $\tau\bar{b}$ producing a $\tau^+\tau^-$ *jet jet* signature are considered.

1.2.3 Leptoquark Search Channel

In first and second generation leptoquark searches, the $\ell^+\ell^-$ final state is observed directly in the detector. The $\tau^+\tau^-$ *jet jet* leptoquark signature must be further specified by the tau decay modes (see Table 1.2.2). By charge conservation, the decay products of the tau must contain an odd number of charged particles, or "prongs". The world averages of the 1-prong, 3-prong, and 5-prong branching fractions are $(84.2 \pm 0.6)\%$, $(14.25 \pm 0.25)\%$, and $(0.00101 \pm 0.00011)\%$, respectively. For the purposes here, the $\tau^+\tau^-$ final states are most conveniently classified by dilepton,

[3]Experiments at $p\bar{p}$ colliders use the missing energy transverse to the beam, $\not{E}_t$, since the center-of-mass frame of the hard scatter cannot be uniquely determined when neutrinos are involved. In contrast, the center-of-mass frame at e^+e^- colliders corresponds to the lab frame. Therefore the total missing momentum, $\not{p}$, is known.

Decay Mode	World Average Branching Fractions, %
$\tau^- \rightarrow e^- \bar{\nu}_e \nu_\tau$	17.88 ± 0.18
$\tau^- \rightarrow \mu^- \bar{\nu}_\mu \nu_\tau$	17.46 ± 0.25
$\tau^- \rightarrow \pi^- \nu_\tau$	11.3 ± 0.4
$\tau^- \rightarrow K^- \nu_\tau$	0.67 ± 0.05
$\tau^- \rightarrow K^{*-} \nu_\tau$	1.45 ± 0.12
$\tau^- \rightarrow \rho^- \nu_\tau$	25.0 ± 0.4
$\tau^- \rightarrow \pi^+\pi^-\pi^- \nu_\tau + \geq 1\,\pi^\circ$	5.53 ± 0.30
$\tau^- \rightarrow \pi^-\pi^\circ\pi^\circ \nu_\tau$	9.31 ± 0.34
$\tau^- \rightarrow \pi^+\pi^-\pi^- \nu_\tau$	8.39 ± 0.31

Table 1.3: The major tau decay channels and the world average branching ratios [40]. The in tau decay Monte Carlo used in this analysis (TAUOLA [91, 92]), the last two decay modes are identified with $\tau^- \rightarrow a_1^- \nu_\tau$. The τ^+ decay modes are the charge conjugates of the modes listed above.

lepton + hadrons, and all hadronic final states. The total branching fractions for these final states are listed below, where τ_h corresponds to any hadronic decay mode of the tau.

$\tau\tau$ Final States	Σ Branching Fraction
ee, $\mu\mu$, $e\mu$	~ 13 %
$\mu\ \tau_h$, $e\ \tau_h$	~ 46 %
$\tau_h\ \tau_h$	~ 41 %

The $\mu\tau_h$ and $e\tau_h$ final states are chosen for this analysis. There are several reasons for this. The electron or muon provide a means to trigger on the leptoquark event. These *inclusive* electron and muon triggers are vital to studying high-p_t physics at hadron colliders and are described in the next chapter. With an electron or muon from the $\tau^+\tau^-$ pair, the dilepton or lepton + hadrons final states are the remaining possibilities. The lepton + hadrons channel is chosen because it has a larger branching fraction than the dilepton channel. Furthermore, the lepton + hadron final state has characteristics which distinguish it from background processes. In the LQ rest frame, the τ and b emerge with momentum $\sim M_{LQ}/2$. The tau mass is 1.78 GeV/c^2, and the leptoquarks considered in this analysis have masses $M_{LQ} \gtrsim 45$ GeV/c^2 (see the next section). Therefore, the hadronic tau decay products will form a highly collimated jet of particles, and typically only one or three of these are charged. These properties are used to select hadronic tau decays and reject jets from quarks and gluons (see Section 3.5). Furthermore, the characteristics of the leptonic decays are used to select leptons from tau decays. The leptonic tau decays contain two neutrinos, while the hadronic decays contain only one. Thus, the total momentum carried by the neutrinos will on average lie along the lepton direction more often than that of the hadronic tau. These features are summarized in the signature for third generation leptoquarks below:

Signature for $p\bar{p} \rightarrow$ LQ $\overline{\text{LQ}} \rightarrow \tau^+\tau^-\ b\ \bar{b}$

1. An energetic lepton. As mentioned above, this triggers the LQ $\overline{\text{LQ}}$ event

2. An energetic, collimated jet of hadrons with one or three charged particles. This is to select jets preferentially from hadronic taus rather than from quarks or gluons.

3. Total neutrino momentum, $\vec{p}$, close to the lepton direction. This selects leptons from tau decays, and thus events containing $\tau^+\tau^-$ pairs.

4. Additional jets in the event. This selects events with leptoquark pairs.

The search for events with this signature is presented in Chapter 4.

1.2.4 Experimental Constraints on Leptoquarks

1.2.5 Bounds from Direct Searches

The CDF and DØ Collaborations report the highest mass bounds on first and second generation scalar leptoquarks. The DØ searches [20, 21] are based on 15 pb^{-1} of data using the $\ell^+\ell^-$ *jet jet* and $\ell\nu$ *jet jet* channels. The 95% Confidence Level (C.L.) mass limits on first generation leptoquarks are 133 (120) GeV/c^2 for $\beta = BR(\mathrm{LQ} \rightarrow \ell q) = 100\%(50\%)$. The DØ limits on second generation leptoquarks are 111 (89) GeV/c^2 for $\beta = 100\%(50\%)$. The CDF leptoquark searches employ only the $\ell^+\ell^-$ *jet jet* signature. The CDF 95% C.L. mass limits on first generation leptoquarks [22] are 113 (80) GeV/c^2 for $\beta = 100\%(50\%)$ with 4.1 pb^{-1} of data. The limits on second generation leptoquarks based on 67 pb^{-1} of data [23] are 180 (141) GeV/c^2 for $\beta = 100\%(50\%)$.

Leptoquarks may be produced at electron-proton colliders, but the production cross sections depend not only on the leptoquark mass but also directly on the unknown q-ℓ-LQ coupling strength. The ZEUS Collaboration [24] reports mass limits (95% C.L.) for first generation leptoquarks with coupling strength $\lambda \sim \sqrt{4\pi\alpha_{EM}}$. For leptoquarks with left-handed (right-handed) couplings, the mass limits are 168 (176) GeV/c^2, respectively. More recent results from the H1 Collaboration [25] ex-

clude first generation leptoquarks with masses up to 275 GeV/c^2 for with a similar coupling strength, depending on the leptoquark type.

The LEP e^+e^- experiments [26, 27, 29, 28], search for scalar leptoquark pairs from Z° decays. The mass bounds for first and second generation leptoquarks are lower than those from the $p\bar{p}$ collider experiments. However the LEP experiments set the highest mass limits for leptoquarks coupling to third generation fermions. The decays LQ $\rightarrow t\nu$ and $t\tau$ are kinematically inaccessible and are not treated in the LEP analyses. The L3 and OPAL Collaborations search for a $\tau^+\tau^-$ *jet jet* final state. L3 excludes a charge $\frac{2}{3}$ leptoquark (LQ $\rightarrow \tau^+ b$ with $BR = 100\%$) with $M < 41.6$ GeV at 95% C.L. OPAL allows leptoquark couplings which mix fermion families (LQ $\rightarrow \nu_\tau q$ with $q \neq t, b$). Therefore, the τ $\not{p}$ *jet jet* signature is also included in the search. The OPAL limits depend on the leptoquark type and on the branching fraction into $\tau^\pm$. The excluded masses are $M < 41.4$ - 45.8 GeV for BR(LQ $\rightarrow \tau$) = 100%, and $M < 43.2$ - 46.1 GeV for BR(LQ $\rightarrow \tau$) = 50%. The ALEPH Collaboration restricts its third generation leptoquark search to charge $\frac{1}{3}$ leptoquark pairs with no family mixing (LQ $\rightarrow b\nu_\tau$ with BR = 100%). Searching for a dijet and monojet final state, ALEPH's mass bound is $M > 45$ GeV at the 95% confidence level. The DELPHI Collaboration does not consider third generation leptoquarks in its searches.

1.2.6 Indirect Bounds

Most efforts to indirectly constrain leptoquarks have concentrated on the first and second generations [32, 33, 35, 18]. A survey of leptoquark bounds presented by Davidson, et al. [17] has considered leptoquarks coupling to third family fermions excluding the top quark (the analysis predates the top mass measurement). Thus the constraints derived for third generation leptoquarks also involve couplings to first or second generation fermions as well. For example, the experimental bounds on $B \rightarrow \tau^+\tau^- X$ are used to derive the constraints on leptoquark couplings and masses

in Equation 1.5.

$$\lambda_{31}\lambda_{33} < 0.01\left(\frac{M_{LQ}}{100\ \text{GeV}}\right)^2 \tag{1.5}$$

The subscripts on the couplings denote the lepton and quark family, respectively. Similar bounds from other processes are presented in Ref. [17]. However only leptoquarks with couplings to the other fermion families are constrained. In the remainder of this section, the indirect bounds on leptoquarks which couple exclusively to third generation fermions are considered.

Leptoquarks can affect the physics at LEP in next-to-leading-order processes. In contrast to the direct searches, this is sensitive to leptoquarks coupling to the top quark. In fact, only the leptoquarks which couple to top are significantly constrained by the indirect LEP searches.

Two groups [15, 16] have calculated the *scalar* leptoquark contributions to LEP observables. The leptoquark quantum numbers and couplings to fermions are those considered in Ref. [31] and the leptoquark couplings to the gauge bosons follow from SU(2)×U(1) invariance. Both analyses assume that only one $SU(2)_L$ multiplet of leptoquarks exists and that leptoquarks within the same multiplet are mass degenerate.

Leptoquarks appreciably affect LEP physics only through corrections to the $Zf\bar{f}$ vertex (Figure 1.5). The magnitude of the corrections is enhanced by powers of fermion masses involved. As a consequence, loops containing the top quark make the dominant contribution. The constraints for a given leptoquark type depend on the mass and coupling strength. For a coupling strength $\lambda = \frac{e}{\sin\theta_W}$, the lowest allowed mass for a leptoquark coupling to top can range from 200 GeV/c^2 to 550 GeV/c^2. The bounds depend somewhat on the values of Standard Model parameters used. The uncertainties in the strong coupling $\alpha_s(M_Z^2)$ and the Higgs mass M_H affect the leptoquark bounds the most. The leptoquarks which do not couple to the top quark are unbounded unless the coupling is strong ($\lambda^2 = 4\pi$). For example, the charge-$\frac{4}{3}$ leptoquark which couples only to τb with an electroweak coupling strength is uncon-

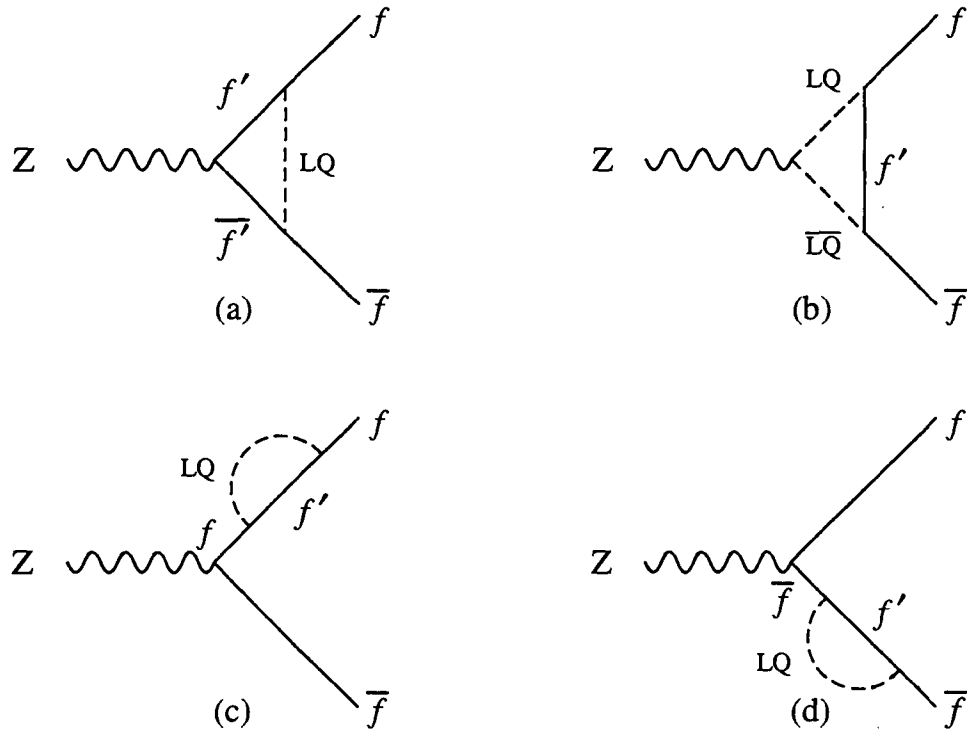

Figure 1.5: The leading order leptoquark-induced diagrams contributing to the $Z \rightarrow f\bar{f}$ vertex corrections.

strained by these analyses.

The direct and indirect leptoquark searches do not consider *vector* leptoquarks explicitly. Also the indirect searches do not address the possible effects of other exotics associated with the leptoquarks, eg. the additional gauge bosons in extended technicolor theories [14].

1.2.7 Leptoquark Production

At hadron colliders, leptoquarks can be produced singly or in pairs. Single LQ production cross section in $p\bar{p}$ collisions is directly proportional to λ^2, the q-ℓ-LQ coupling strength. In contrast, continuum LQ pair production in $p\bar{p}$ collisions has only a negligible dependence on λ (provided λ is not large). In addition to continuum pair

production, some technicolor theories contain resonant production mechanisms for third generation LQ pairs.

Single LQ Production

The single production of leptoquarks occurs at lowest order in gq collisions via the Feynman diagrams in Figure 1.6. The total cross section is proportional to the square of the unknown Yukawa coupling λ. Since a single leptoquark plus its associated lepton emerge from the hard collision, this process leads to different final states than pair-produced leptoquarks. The single production of leptoquarks is expected to be suppressed relative to the pair production, provided the q-ℓ-LQ is not large. Moreover, the suppression is larger for third generation leptoquarks since the incident quarks in in Figure 1.6 must be a t or b quark. The small probability to find t or b quarks in the sea suppresses the cross section for single production. This is seen by considering the single production of second generation leptoquarks. For second generation leptoquarks, the incident quarks are c or s quarks. Assuming $\lambda^2/4\pi = 0.1\,\alpha_{EM}$, the single production cross section for second generation leptoquarks is suppressed by a factor of $\sim 150\ (250)$ relative to the pair cross section for $M_{LQ} = 200\,(50)$ GeV/c^2 [30]. Since the parton distributions for sea t and b quarks are smaller than that of c or s quarks, this suppression is expected to be larger for third generation leptoquarks. Therefore this source of leptoquarks is not considered here.

LQ Pair Production: Continuum

The pair production of leptoquarks occurs at tree-level by the diagrams in Figures 1.7-1.8. The q-ℓ-LQ coupling enters only in the diagram with t-channel lepton exchange. As in the single production case, the contribution from this diagram is suppressed since the incident quarks are b or t for leptoquarks coupling to the third generation. This diagram is omitted to simplify the calculations.

The pair production cross section depends on the leptoquark spin through the

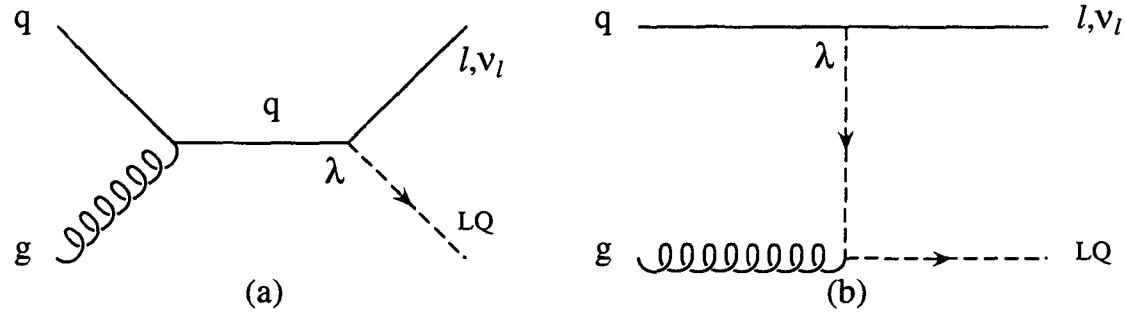

Figure 1.6: The lowest order Feynman diagrams for single leptoquark production in gq collisions. The LQ type is determined by the (anti-)fermion flavors involved. For third generation leptoquarks, $q = t$ or b.

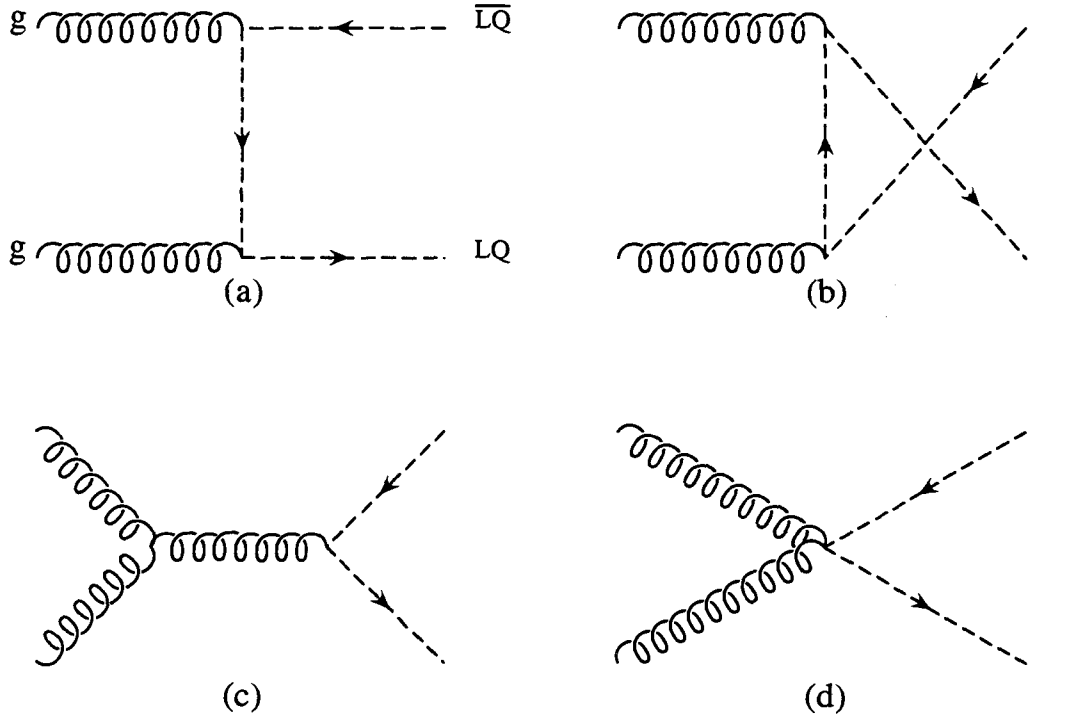

Figure 1.7: The leading order diagrams for LQ pair production in gg collisions.

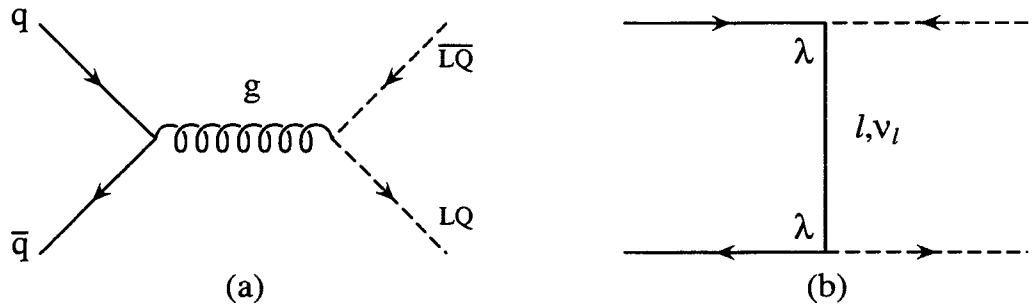

Figure 1.8: The leading order diagrams for LQ pair production in $q\bar{q}$ collisions. In diagram b, the LQ type determines the incident quark flavors and t-channel lepton.

g-g-LQ-LQ and g-LQ-LQ couplings. The scalar case [34] is simpler since couplings are completely "fixed" – there are no free parameters or assumptions to make. However, the couplings for vector leptoquarks are model dependent.

The procedure to derive the vector leptoquark couplings to gluons is as follows [38, 39]. In theories containing vector leptoquarks, the leptoquarks are most likely the gauge bosons of some larger symmetry group. The leptoquark couplings to the gluon are then fixed by gauge invariance. In the case that the leptoquarks are composite particles, the leptoquarks can acquire anomalous couplings to the gluon. One such coupling is an anomalous chromomagnetic moment usually described in the literature by the parameter κ. Two values of κ are considered here: $\kappa = 1$ which corresponds to the "non-anomalous" or gauge theory case, and $\kappa = 0$ which corresponds to a non-gauge vector leptoquark boson. The choice $\kappa = 0$ is convenient since the pair production cross section for fixed M_{LQ} contains a minimum near $\kappa = 0$.

1.2.8 Pair Production Cross Section

The cross section for a $p\bar{p}$ collision to result in a final state $\mathcal{F}$ is calculated by separating the process into the hard-scattering or *partonic* cross section and the probability for finding the hard scattering partons within the proton or anti-proton. This is

expressed as

$$\sigma_{tot}(p\bar{p} \to \mathcal{F}) = \sum_{a,b} \int_0^1 dx_a \int_0^1 dx_b \; \hat{\sigma}_{ab}(a\,b \to \mathcal{F}) \cdot \Big[f_p^a(x_a, q^2) f_{\bar{p}}^b(x_b, q^2) + f_p^b(x_b, q^2) f_{\bar{p}}^a(x_a, q^2) \Big] \tag{1.6}$$

where the sum is over parton types ($a, b = u,\ \bar{u},\ d,\ \bar{d} \ldots t,\ \bar{t},\ g$), x is the longitudinal momentum fraction of the parton, $\hat{\sigma}_{ab}$ is the partonic cross section, and $f_p^a(x_a, q^2)$ ($f_{\bar{p}}^a(x_a, q^2)$) represents the probability for having parton a with momentum fraction x_a inside the proton (anti-proton). The distribution functions, $f(x, q^2)$, depend on the parton type (quark flavor or gluon). They are determined experimentally at low momentum transfer q^2 from several processes and are evolved to higher q^2 using the Altarelli-Parisi equations [83]. The total cross sections depend on the momenta of the hard scattering partons, $x_a P_{bm}$ and $x_b P_{bm}$, where P_{bm} is the beam momentum. At the Fermilab Tevatron, $P_{bm} = 900$ GeV/c.

The partonic cross section depends on the reaction in question. In processes involving the strong interaction, $\hat{\sigma}_{ab}$ will contain the running QCD coupling, $\alpha_s(Q^2)$. In the leading-log approximation, this is given by

$$\alpha_s(Q^2) = \frac{12\pi}{(33 - 2N_f) \ln\left(\frac{Q^2}{\Lambda_{QCD}^2}\right)} \tag{1.7}$$

where N_f is the number of flavors of fermions with mass $m < \frac{1}{2}Q$ and Λ_{QCD} is the fundamental scale parameter of QCD. For $Q^2 \gg \Lambda_{QCD}^2$, α_s is small. These are the conditions under which a perturbation expansion in α_s converges. For $Q^2 \sim \Lambda_{QCD}^2$, the QCD coupling becomes large, and perturbation theory cannot be applied. The parameter Λ_{QCD} is determined from experiment.

Figure 1.9 shows the total leptoquark pair production cross section as a function of LQ mass. The cross section calculation for the scalar leptoquark pairs is performed to leading order with the diagrams in Figures 1.7 and 1.8 as implemented by the

the ISAJET Monte Carlo[66]. (See Chapter 6 for details). The vector leptoquark cross sections are calculated using the PYTHIA Monte Carlo [82] with leading order subprocess cross sections [41] provided by the authors of Ref. [38]. The CTEQ2L [90] parton distribution functions were used in all cases. The pair production cross section for scalar leptoquarks with $M_{LQ} = 50$ GeV/c^2 is 315 pb^{-1}. The production cross section for non-gauge ($\kappa = 0$) vector leptoquark pairs with $M_{LQ} = 50$ GeV/c^2 is ~ 3800 pb^{-1}, while for gauge ($\kappa = 1$) vector leptoquark pairs, it is ~ 19500 pb^{-1}.

Resonant Pair Production: Technicolor

For completeness, an additional production mechanism for leptoquark pairs is mentioned here briefly.

The theories of extended technicolor (ETC) [12, 13, 14] contain a rich spectrum of technihadrons. In these models the color-triplet technipions (π_T^3) are scalar leptoquarks. The technipions decay to ordinary fermions with a coupling strength proportional to fermion mass, although the specific form of the coupling is model dependent. The technihadrons have QCD-like interactions with each other. The color-octet technirhos (ρ_T^8) couple directly to π_T^3 pairs, analogous to $\rho^o \rightarrow \pi^+\pi^-$ in QCD for example. The ρ_T^8 have the same quantum numbers as that of the gluon, and thus couple directly to the gluon. (This is analogous to the direct coupling between the photon and J/ψ resonance.). Therefore the ρ_T^8 provide a resonant production mechanism for π_T^3 pairs (scalar leptoquarks) in hadron collisions. The lowest-order diagrams responsible for this are shown in Figure 1.10.

This resonant production mechanism will in general enhance the cross section and efficiency for detecting the leptoquark pairs. However, the degree of enhancement is affected by the parameters and dynamics of the theory. Further treatment of these models is beyond the scope of this thesis.

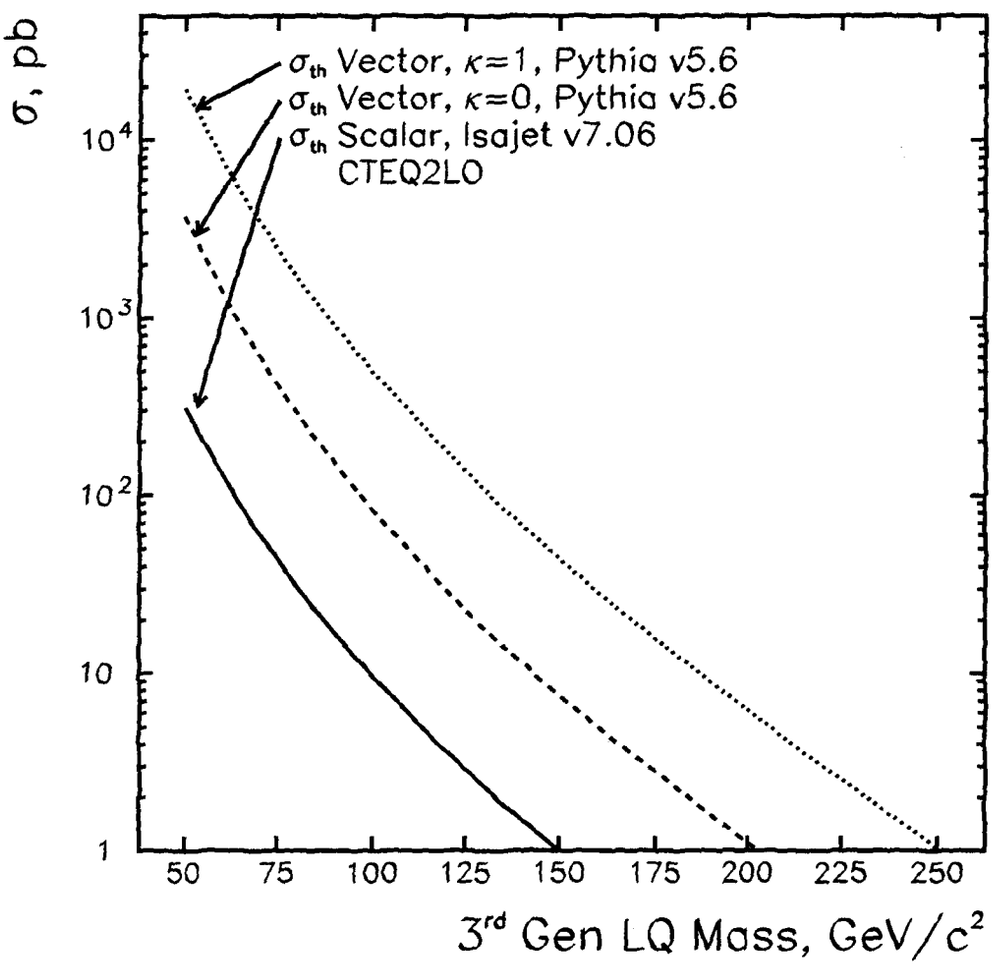

Figure 1.9: The theoretical cross sections for scalar and vector leptoquark pair production. The scalar cross section is calculated using the Isajet Monte Carlo program configured for scalar leptoquark pairs, as described in the text. The $q\bar{q}$ and gg subprocess cross section for vector leptoquark pairs have been provided by Rizzo, et. al. The point cross sections vector leptoquark pairs are integrated using the Pythia Monte Carlo program. The CTEQ2L parton distribution functions were used in all cases.

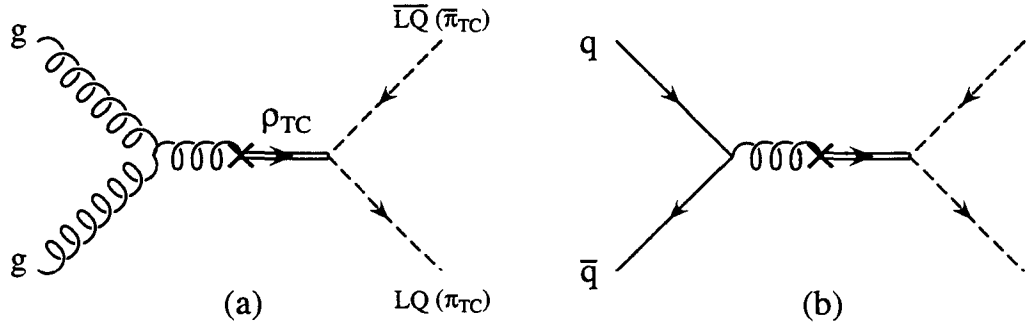

Figure 1.10: Feynman diagrams for resonant leptoquark pair production in extended technicolor (ETC) theories. The color-triplet technipions in these models are leptoquarks. In ETC models, the technirho couples directly to the gluon enhancing the production of leptoquark pairs.

Chapter 2

The CDF Experiment

The Collider Detector at Fermilab (CDF) is located at the the Fermi National Accelerator Laboratory in Batavia, Illinois. The CDF experiment has two major components: the system of accelerators which provides colliding proton-antiproton ($p\bar{p}$) beams, and the CDF detector which records the results of the $p\bar{p}$ collisions. This chapter begins with brief description of the accelerator complex, after which the components of the CDF detector used in this analysis are described.

2.1 The Accelerators

Figure 2.1 shows a diagram of the accelerator complex at Fermilab. In order to reach the center-of-mass energy of $\sqrt{s} = 1.8$ TeV, the protons and antiprotons are accelerated in several stages. A Cockroft-Walton generator (not shown in Figure 2.1) produces a beam of 750 KeV H^- ions which is then injected into the linear accelerator (Linac). The Linac accelerates the H^- ions to an energy of 200 MeV. Then both electrons are stripped off the H^- ions by a carbon foil, and the resulting protons are injected into the circular Booster accelerator. The Booster accelerates the protons to 8 GeV, forms them into discrete bunches, and feeds the bunches of protons into the Main Ring. The protons are then accelerated to 150 GeV and coalesced into a single

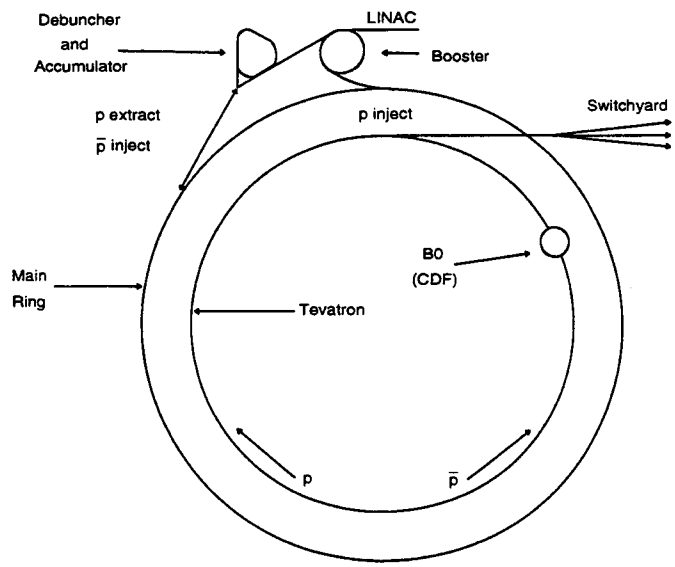

Figure 2.1: A schematic of the Tevatron and associated accelerators

bunch. The bunch is then injected into the Tevatron accelerator. For standard Collider operation, 6 bunches of protons and antiprotons are injected into the Tevatron. The Main Ring and Tevatron both lie in the same 1 *km*-radius tunnel.

The Main Ring also serves to produce a 120 GeV proton beam for antiproton production. A proton beam in the Main Ring is extracted onto a tungsten target. This produces secondary particles among which are antiprotons. The antiprotons are focused by a current-pulsed lithium lens and directed into storage ring called the Debuncher. The antiprotons are stochastically cooled in the Debuncher and then transferred to the Accumulator ring. The result of the cooling is a mono-energetic beam of 8 GeV antiprotons. When a sufficient number of antiprotons have been collected, six bunches of antiprotons are extracted from the Accumulator and injected into the Main Ring. Then they are accelerated to 150 GeV and injected into the Tevatron with the protons. The protons and antiprotons occupy the same beam pipe, but circulate in opposite directions with the proton bunches clockwise and the antipro-

ton bunches counter clockwise. In the Tevatron ring, the bunches of protons and antiprotons are accelerated to 900 GeV. The six bunches of protons and six bunches of antiprotons cross at 12 points around the Tevatron ring. The CDF experiment is located at one of these points, the B0 interaction region. The DØ experiment is located at the DØ interaction region, at 6 o'clock in Figure 2.1 (not shown).

In high energy physics, particle collisions are characterized by a quantity called luminosity, $\mathcal{L}$. The luminosity is the product of the incident beam flux (particles per second) and the mean target density (particles per unit area). For proton–anti-proton collisions, the luminosity is given by

$$\mathcal{L} = \frac{N_p N_{\bar{p}} C}{4\pi\sigma^2}, \tag{2.1}$$

where N_p ($N_{\bar{p}}$) is the number of protons (antiprotons) in each bunch, C is the bunch crossing rate, and σ is the rms width of the Gaussian beam profile. The crossing rate is $\sim 50\ kHz$ which gives 3.5 μs between collisions. This analysis uses data collected during two distinct periods: Run 1A lasting from August 1992 to May 1993; and the portion of Run 1B lasting from January 1944 to February 1995. Typical and peak luminosities for Run 1A were 0.54×10^{31} cm$^2/s$ and 0.92×10^{31} cm$^2/s$ respectively. For Run 1B these were 1.6×10^{31} cm$^2/s$ and 2.8×10^{31} cm$^2/s$ respectively.

2.2 Overview of the CDF Detector

The CDF detector is a general purpose detector designed to analyze the products of 1.8 TeV $p\bar{p}$ collisions. A detailed description is given in the literature [42]. The detector is cylindrically symmetric and surrounds the beam pipe as shown in the isometric view in Figure 2.2. Figure 2.3 shows the side view cross section of a quarter of the CDF detector. The detector is forward-backward symmetric about the plane transverse to the nominal collision point which is the bottom right corner of Figure 2.3.

The CDF coordinate system is indicated in Figure 2.3. The origin $x = y = z = 0$

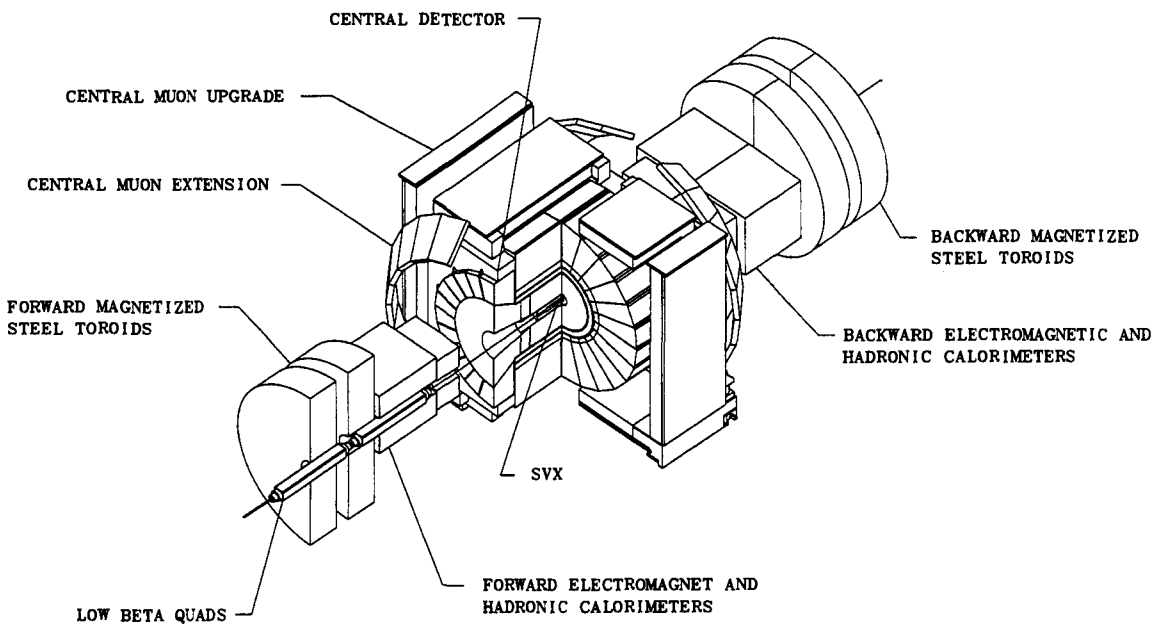

Figure 2.2: Isometric view of the CDF Detector

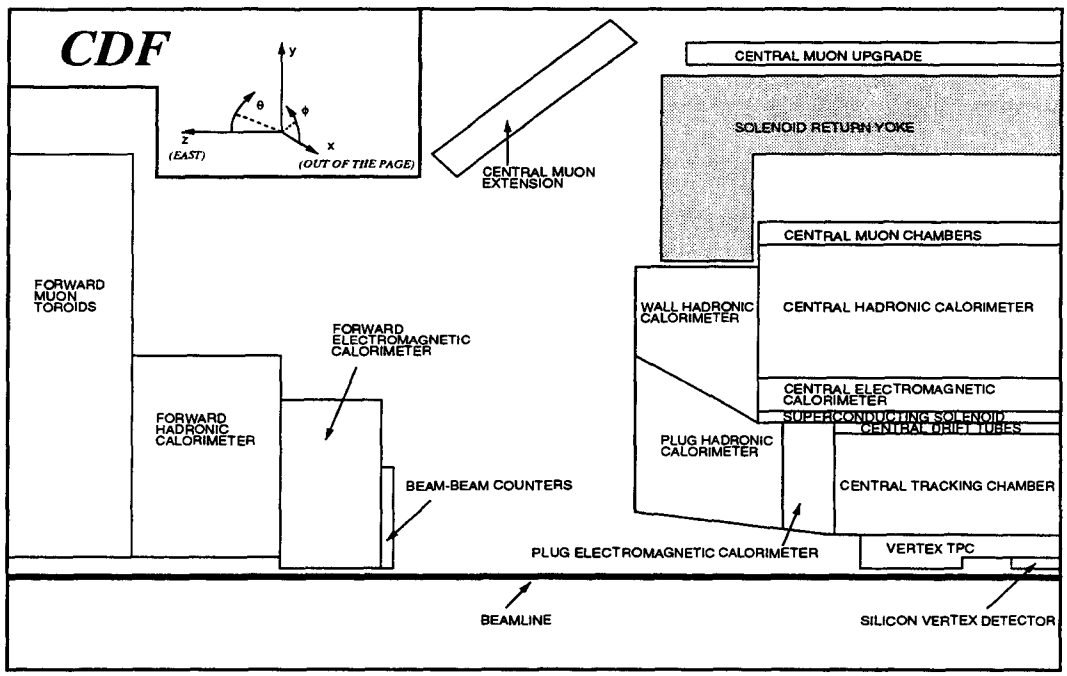

Figure 2.3: Quarter view schematic of the CDF Detector.

is at the nominal collision point located at the geometric center of the detector. The z axis is in the direction of the proton beam, y is vertical, and x is horizontal as shown. The azimuthal angle ϕ is the angle around the beam line, and the polar angle θ is the angle relative to the proton beam direction. The variable pseudorapidity, η, is often used instead of θ. It is defined as

$$\eta = \ln \tan \frac{\theta}{2} \tag{2.2}$$

Also, the *transverse* energy, E_t, is used rather than using the scalar energy, E, to characterize the energy deposits in the calorimeter. The transverse energy is defined as

$$E_t = E \times \sin \theta \tag{2.3}$$

(The *transverse momentum*, p_t, is defined similarly by replacing E by p in Equa-

tion 2.3) The variables E_t and η are more convenient than E and θ to describe $p\bar{p}$ collisions. This is because the pseudorapidity of a relativistic particle is nearly equal to its rapidity, y, given by

$$y = \frac{1}{2} \ln \frac{E + p_z}{E - p_z} \tag{2.4}$$

The variables E_t, ϕ, and η are appropriate for characterizing the kinematics of the collisions because E_t and ϕ remain unchanged while $\eta \sim y$ transforms additively under the unavoidable longitudinal boosts in $p\bar{p}$ collisions. Moreover the η and ϕ coordinates are a more appropriate for jets since the distribution of energy within a jet is on average circular in η-ϕ space. This motivates the projective η-ϕ geometry of the calorimeter segmentation discussed below. Finally, the variables E_t and p_t are used because many of the interesting physics processes produce particles with large transverse energy. Most inelastic $p\bar{p}$ collisions produce particles with very small transverse momentum, around 0.5 GeV/c total, whereas a W boson can produce a charged lepton with typical $p_t \sim 35$ GeV/c.

The CDF detector consists of three major systems shown in Figure 2.3: the tracking detectors, the calorimeters, and the muon chambers. The tracking detectors occupy the innermost region of the CDF detector. They are fully contained within a 1.4 Tesla magnetic field produced by a solenoidal superconducting magnet. The tracking systems are used to measure the charge and momentum of charged particles. The calorimeter systems surround the tracking system. The calorimeters are segmented with a projective tower geometry in η and ϕ which covers $|\eta| \lesssim 4.2$ and 2π in azimuth. The calorimeters are used to measure particle energies, and act as a hadron absorber for the muon detection systems. The muon detectors, situated behind the calorimeters, consist of drift chambers which record the passage of penetrating particles.

2.3 Tracking Systems

The tracking system consists of three tracking detectors situated inside the solenoidal field. The innermost detector is the four-layer Silicon Vertex Detector (SVX) [44, 45]. The SVX is 51 cm long and consists of twin cylindrical modules which meet at $z = 0$. The SVX detector of Run 1A was replaced by the SVX′ detector for Run 1B due to radiation damage suffered by the SVX readout chip during data taking. The design of the two are similar with the exception that the SVX′ is more resistant to radiation damage. The four layers of the SVX are at distances of 3.0, 4.2, 5.7, and 7.9 cm from the beamline. (The SVX′ inner radius is 2.86 cm). The SVX is designed to track particles in the r-ϕ view[1] and distinguish sequential decay vertices with a resolution on the tens-of-microns level. For instance, the SVX can be used to tag a B hadron by identifying a decay vertex displaced from the primary interaction point. In this analysis, the SVX is used to improve the tracking resolution through the precise determination of the beam position.

Outside the SVX is the vertex time projection chamber (VTX) [43]. The VTX is designed to provide tracking information in the r-z view up to a radius of 22 cm for $|\eta| < 3.5$. The VTX consists of 28 modules which surround the SVX, with each module approximately 10 cm in the z extent. Tracks reconstructed in the r-z view are used to determine the z position of the primary event vertex with a typical resolution, $\sigma_z = 1$ mm.

The SVX and VTX are surrounded by the Central Tracking Chamber (CTC) [46]. The CTC provides a measurement of the momentum and direction of charged particles in the range $|\eta| \leq 1.5$. The CTC is a large cylindrical drift chamber with a total of 6152 sense wires arranged into cells of 6 or 9 wires each. The cells are organized in 84 layers, and the layers are grouped into 9 *superlayers*. The cell arrangement is shown in Figure 2.4. Five of the *superlayers* contain 12-wire cells strung parallel

[1] r = radial distance from the interaction point

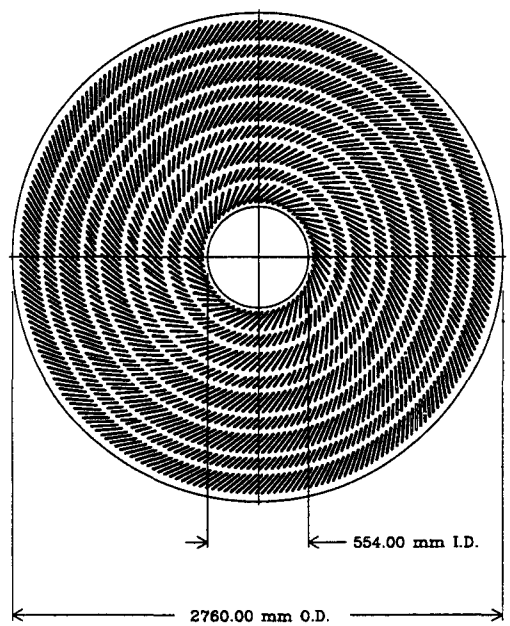

Figure 2.4: A schematic of the Central Tracking Chamber (CTC) endplate. The beam direction is perpindicular to the page. The sense wires are organized into cells, and the cells are grouped into nine superlayers which are shown here.

to the magnetic field and beam direction. These *superlayers* are called *axial layers.* The *axial layers* provide a precise measurement of the track position in the r-ϕ view. Between each pair of *axial layers* is a *stereo superlayer.* The *stereo* layers contain 6-wire cells which are tilted at an angle of $\pm 3°$ with respect to the beam direction. These provide information about the z position of the track.

An energetic charged particle which exits through the outer superlayer will leave 84 *hits* in the sense wires. The CTC track reconstruction is a pattern recognition algorithm which fits the hits to the arc of a helix. The curvature of the helix is inversely proportional to the track p_t. The p_t resolution using the CTC hit information alone is $\delta p_t = 0.0016 \times p_t^2$ GeV/c. The beam position as measured by the VTX or SVX can be used to provide an additional measurement of the track position. Incorporating this information in a *beam-constrained* fit improves the momentum resolution to $\delta p_t = 0.0011 \times p_t^2$ GeV/c. Particles with $p_t \lesssim 400$ MeV/c curl up in the magnetic field and do not exit the CTC.

The high track reconstruction efficiency and two-track resolution are important for the leptoquark search. The track finding efficiency for isolated tracks was measured using a special $W \rightarrow e\nu$ sample formed with no tracking requirements. The resulting track reconstruction efficiency was very high: $\varepsilon = 99.67^{+0.06}_{-0.07}\%$ [47]. The two-track resolution was estimated by adding single simulated tracks to real CDF events. For tracks with an average r-ϕ separation greater than 2 cm, the track reconstruction efficiency was estimated to be $\sim 97\%$ [93].

2.4 Calorimeters

The CDF calorimeter is used to measure the energies and positions of electromagnetic and hadronic showers. The calorimeter consists of three distinct subsystems: the central, plug, and forward calorimeters. Together they provide nearly complete coverage in solid angle to within 2° of the beam line. The calorimeters are segmented

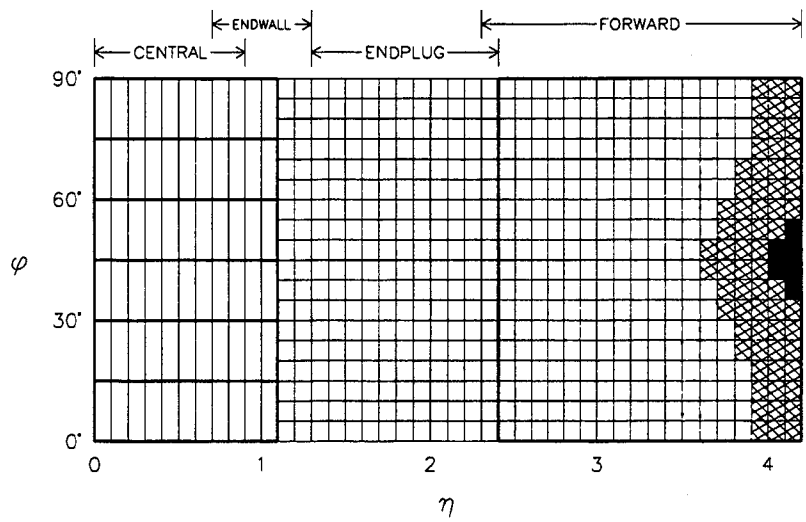

Figure 2.5: One-eighth of the calorimeter towers, showing the η-ϕ projective tower segmentation. The heavy lines indicate module or chamber boundaries. The cross-hatched area has only partial hadron depth coverage due to space required for the low-beta quadrupole magnets. The shaded area has no coverage. The electromagnetic calorimeters have complete ϕ coverage out to a pseudorapidity of 4.2.

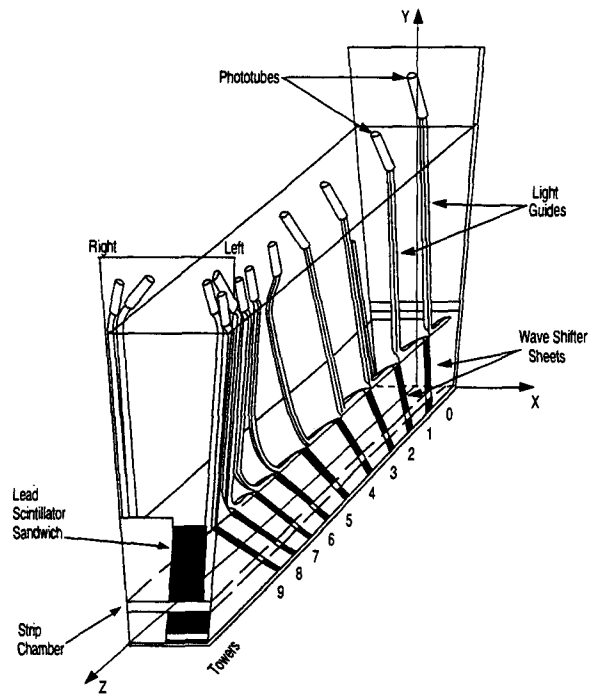

Figure 2.6: A cutaway view of a single cental calorimeter wedge, showing the central electromagnetic (CEM) calorimeter and light transmission system. Each wedge spans 15° in ϕ and contains ten towers in η each covering $\sim$ 0.1 units in pseudorapidity. Proportional chambers are embedded in the CEM at a depth roughly corresponding to shower maximum.

into towers in η-ϕ space which project back to the nominal interaction point. In the central region, ($|\eta| \lesssim 1.1$), the tower size is roughly $0.1 \times 15°$ in $\eta \times \phi$. In the plug ($1.1 \lesssim |\eta| \lesssim 2.2$) and forward ($2.2 \lesssim |\eta| \lesssim 4.2$) regions, the tower size is $0.1 \times 5°$ in $\eta \times \phi$. The calorimeter segmentation is shown in Figure 2.5.

Each calorimeter consists of alternating layers of an absorber material in which the particles shower, and an active material which samples the energy flow in the shower. In the central region, plastic scintillators are used as the active medium in the hadronic and electromagnetic calorimeters. The plug and forward calorimeters use proportional tube chambers with segmented cathode pad readout.

The calorimeters in the central region are the central electromagnetic calorimeter (CEM), the central hadronic calorimeter (CHA), and the wall hadron calorimeter (WHA). The calorimeters are divided into wedges which cover 15° in azimuth. The CEM and CHA wedges are combined to form four arches which comprise the central barrel. There are gaps in the calorimeter coverage every 15° in ϕ between each wedge and between the east and west arches at $\eta = 0$. Figure 2.6 is a cutaway view of a central calorimeter wedge with only the electromagnetic compartment shown.

The CEM calorimeter [48] consists of 30 layers of $\frac{1}{8}$ inch thick lead radiator interleaved with 31 layers of 5 mm thick polystyrene scintillator. To ensure a constant number of radiation lengths as a function of polar angle, some lead is replaced with acrylic and the scintillator behind the acrylic is painted black. This way, the CEM is 18 radiation lengths deep on average. The CEM calorimeter represents approximately 1 pion absorption length. Each tower is read out by two phototubes on both sides of the wedge. The scintillation light is transmitted to the phototube through wavelength shifters and light guides located in the gaps in ϕ between each wedge.

A test beam of 50 GeV electrons was use to calibrate each wedge at the tower center. Position scans were performed to determine a response map that is used to correct for variations due to the position of the shower within the tower. There were 6% peak-to-peak variations due to shower leakage from the wedge boundaries and variations in light collection from the scintillator and wavelength shifter (see Figure 3.3). The energy resolution of the CEM is

$$\left(\frac{\sigma_E}{E}\right)^2 = \left(\frac{13.5\%}{\sqrt{E_t}}\right)^2 + (1\%)^2 \tag{2.5}$$

which was determined from testbeam electrons and $Z \rightarrow ee$ data [50]. The second term accounts for residual response variations not corrected by the calibration procedure.

Embedded near the shower maximum in the CEM are proportional strip and wire chambers (CES) to measure the position and transverse profile of electromagnetic

showers. The wires are strung parallel to the beam direction and provide a view of the shower in the ϕ direction. The strips are perpendicular to the wires and measure the z profile of the shower. The position resolution of the CES is ± 2 mm in both views, determined from 50 GeV test beam electrons.

The CHA and WHA calorimeters [49] together with the CEM provide a measurement of the total energy deposited by a hadron. The CHA calorimeters are located behind CEM compartments in each wedge covering the pseudorapidity range $0 < |\eta| < 0.9$. The WHA ($0.7 < |\eta| < 1.3$) is housed separately in the wall of the magnet yoke. The CHA consists of 32 layers of 1 inch scintillator interleaved with $2\frac{1}{2}$ inch iron absorber. The WHA consists of 15 layers of 1 inch scintillator and 5 inch iron absorber. The WHA and CHA towers are read out through a system of wavelength shifters and lightguides. There are two phototubes per tower on each side of the wedge in ϕ. The CHA and WHA represent a depth of ~ 4.5 interaction lengths. Using test beams of 10–150 GeV pions, the WHA and CHA resolutions were determined to be

$$\left(\frac{\sigma_E}{E}\right)^2 = \left(\frac{50\%}{\sqrt{E_t}}\right)^2 + (3.0\%)^2 \qquad \text{CHA} \tag{2.6}$$

$$\left(\frac{\sigma_E}{E}\right)^2 = \left(\frac{75\%}{\sqrt{E_t}}\right)^2 + (4.0\%)^2 \qquad \text{WHA} \tag{2.7}$$

The leptoquark analysis uses the calorimeter to measure the energy and position of the decay products of tau leptons. Only the decays contained in the central region are considered. This is the region in which the CTC provides a measurement of the charged particle momenta necessary for reconstructing the tau lepton decay products. The energies and directions of hadronic jets from b quark decays are also used in the leptoquark analysis. The calorimeter coverage for these jets is extended to $|\eta| \leq 4.2$ with the plug and forward calorimeters. The central, plug, and forward calorimeters are also used to measure the magnitude and direction in ϕ of the total missing transverse energy in the event (see Section 3.6). This is necessary for selecting $\tau^+\tau^-$ events.

The plug and forward calorimeters are gas calorimeters covering the pseudorapidity regions $1.1 \lesssim |\eta| \lesssim 2.4$ and $2.2 \lesssim |\eta| \lesssim 4.2$, respectively. The calorimeters use proportional chambers with cathode pad readout as the active sampling medium. The response of the gas calorimeters depends on the density of the 50% Argon and 50% Ethane gas mixture and on the anode high voltages. The design of the proportional chambers is such that the atmospheric pressure and ambient temperature determine the calorimeter gas density. Thus for a fixed anode high voltage the gain of the calorimeters will vary with changing atmospheric conditions. The response of the calorimeters is maintained constant with time through an operational procedure called *high voltage feedback*. In high voltage feedback, the anode high voltage is changed to counteract response variations due to drifts in gas density. These high-voltage and density dependences were measured in test beams of electrons and pions. During atmospheric conditions giving a nominal gas density, the calorimeters were calibrated in the test beams using fixed anode high voltages. During Collider data taking, the atmospheric pressure and temperature of the collision hall are monitored to infer the calorimeter gas density. Then calorimeter response was held constant by changing the anode high voltages to compensate for variations from changing gas density. This procedure allowed for continuous running of the detector during changing atmospheric conditions.

The plug electromagnetic calorimeter (PEM) [51] is an annular shaped detector covering each end of the CTC. The PEM consists of 34 layers of conductive plastic proportional tubes interleaved with 2.7 mm sheets of lead absorber representing a depth of 18–21 radiation lengths. The cathodes are copper pads etched on a G-10 board. In the PEM, the pads of 34 layers are ganged into projective towers, each subtending $5^\circ \times 0.1$ in $\phi \times \eta$. Each response of the PEM was calibrated at the center of each tower using 100 GeV test beam electrons. The energy resolution was determined to be

$$\left(\frac{\sigma_E}{E}\right)^2 = \left(\frac{22\%}{\sqrt{E}}\right)^2 + (2\%)^2 \qquad (2.8)$$

The plug hadronic calorimeter (PHA) [52] is located directly behind the PEM. The PHA uses 20 layers of conductive proportional tubes interleaved with 5 cm steel sheets. The PHA is 5.7 interaction lengths deep. The PHA cathode pads are ganged into projective towers as in the PEM. The PHA resolution measured in $\sim 10 - 227$ GeV pion test beams is

$$\left(\frac{\sigma_E}{E}\right)^2 = \left(\frac{106\%}{\sqrt{E}}\right)^2 + (6\%)^2 \tag{2.9}$$

The forward calorimeters cover the pseudorapidity region $2.2 \lesssim |\eta| \lesssim 4.2$ which corresponds roughly to 10° to 2° from the beamline. The forward electromagnetic calorimeter (FEM) [53] consists of 30 layers of aluminum proportional tubes interleaved with 4.5 mm sheets of lead comprising a total of 25 radiation lengths of material. The tower segmentation is similar to that of the plug calorimeters. The FEM resolution to electromagnetic showers is

$$\left(\frac{\sigma_E}{E}\right)^2 = \left(\frac{26\%}{\sqrt{E}}\right)^2 + (2\%)^2 \tag{2.10}$$

measured with test beam electrons. The forward hadronic calorimeter (FHA) [54] completes the calorimetry coverage in the forward region. The FHA is located behind the FEM, and consists of 27 layers of proportional tubes alternated with 5 cm steel sheets. This represents 7.7 absorption lengths. The FHA tower geometry is essentially identical to that of the FEM. The energy resolution for single pions is

$$\left(\frac{\sigma_E}{E}\right)^2 = \left(\frac{137\%}{\sqrt{E}}\right)^2 + (3\%)^2 \tag{2.11}$$

determined in test beam studies.

2.5 Muon Systems

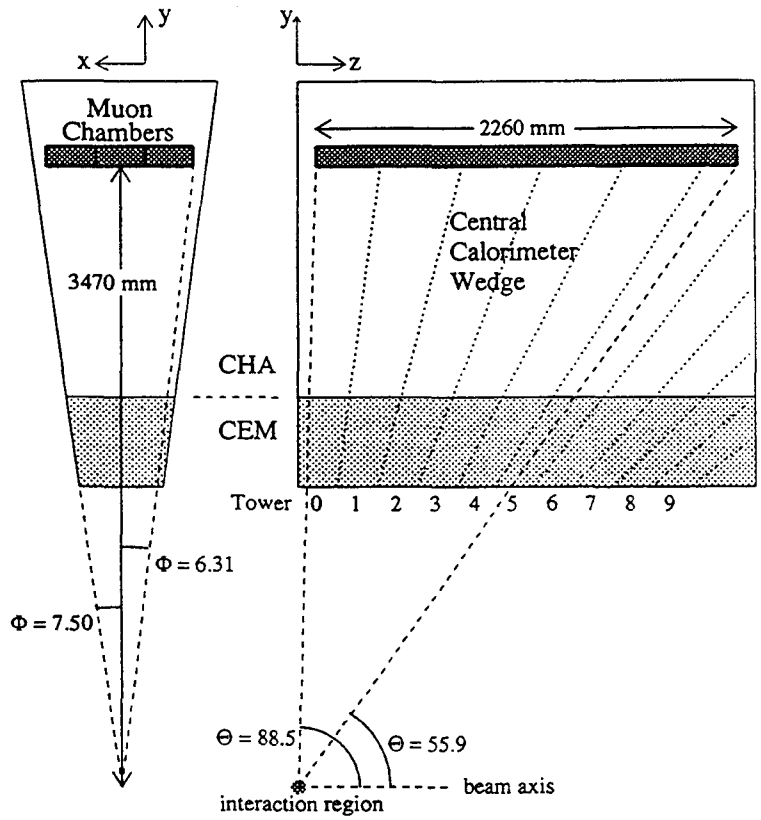

Figure 2.7: A schematic view of a central wedge, showing the location of the Central Muon Chambers (CMU)

There are two distinct muon detection systems in CDF: the forward muon detectors and the central muon detectors. The forward muon system (FMU) [55] is located behind the forward calorimeters, and are not used in this analysis. Leptons from leptoquark decays are produced preferentially in the central. Therefore muons detected in the FMU system do not significantly contribute to the leptoquark detection efficiency.

The central muon system provides muon coverage for the pseudorapidity region $|\eta| < 1$. The central muon detection system consists of three types of muon chambers: the central muon chambers (CMU) [56], the central muon upgrade chambers (CMP), and the central muon extension chambers (CMX). The CMU chambers are embedded in the wedges of the central calorimeter at an average depth of 5.4 pion interaction lengths. The CMU system covers the pseudorapidity region, $|\eta| \lesssim 0.6$. Each central calorimeter wedge contains four layers of single wire drift tubes operated in the limited streamer mode. The CMU layout in a single wedge is shown in Figure 2.7. The layers of drift tubes in each are arranged into three *towers* spanning 5° in ϕ. There are 2.4° gaps in the muon coverage between adjacent calorimeter wedges in ϕ, and a 3° gap at $\eta = 0$ where the east and west wedges meet. Figure 2.8 is a schematic of a 5° muon tower with the trajectory of a muon indicated. Each CMU drift chamber contains a single sense wire which runs the length of the wedge. A muon track *stub* is formed by measuring the time of arrival of the ionization avalanche at each of the four sense wires. The left-right ambiguity is resolved by staggering wires in two of the four layers by 2 mm in the ϕ direction with respect to the radial centerline. The angle of the muon track with respect to the radial centerline is derived from the drift time in two of the four chambers. This angle is used in the muon trigger, discussed in the next section. Cosmic ray data taken by CDF show the chamber resolution in the drift (ϕ) direction to be 250 μm. Information about the z position of the stub may be obtained by charge division. The z position resolution determined from cosmic ray data is 1.2 mm.

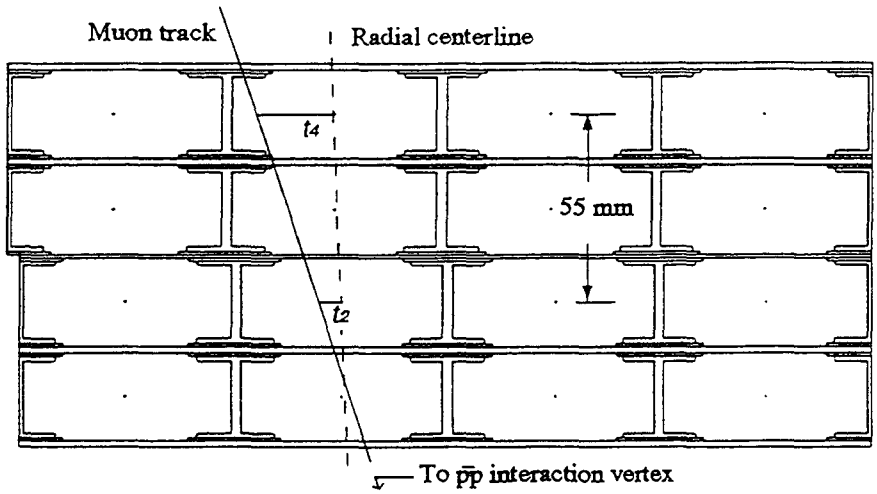

Figure 2.8: A cross section of a single CMU tower. A tower consists of four radial layers of four drift tubes. The sense wires from alternate layers in the muon tower lie on a radial line with the nominal $p\bar{p}$ interaction point. The other two are offset from this line by 2 mm from the chamber midpoint to resolve the left-right ambiguity in the muon position.

Outside the central wedges there is an additional absorber of 60 cm of steel followed by the CMP system. The CMU and CMP cover approximately the same range in η indicated in Figure 2.9. The CMP chambers are mounted on four flat planes around the central calorimeter, about three extra absorption lengths of steel behind the CMU. On the top and bottom of the detector, the CMP chambers planes are mounted to the steel of the solenoid return yoke. On the north and south sides of the detector, the CMP planes are attached to walls of steel built expressly for the CMP system. The CMP sense wires are arranged in four layers parallel to the beamline. The CMP drift chambers have the same cross sectional size as the CMU chambers, but span the full length of the detector in z, 3.2 m, with no gap at $\eta = 0$. The CMP coverage has gaps in ϕ which correspond to gaps in the magnet return yoke (see Figure 2.9). The CMP drift chambers are staggered in the ϕ direction by half the chamber width. Muon stubs are reconstructed in the transverse plane by measuring the drift times

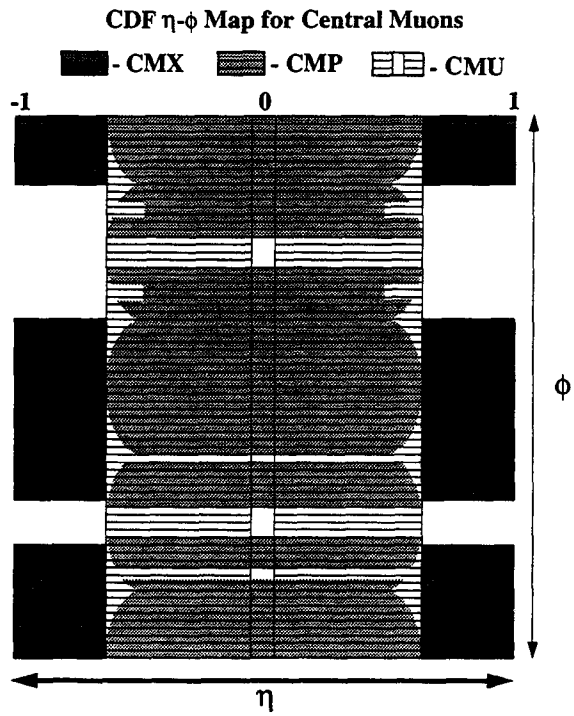

Figure 2.9: A schematic map of the CDF cental muon coverage. Not shown here are are the gaps in the CMU coverage every 15° in ϕ between wedges and at $\eta = 0$ where the east and west central calorimeter barrels meet (see Figure 2.7). The two largest gaps in CMP ϕ coverage are due to the solenoid return yoke.

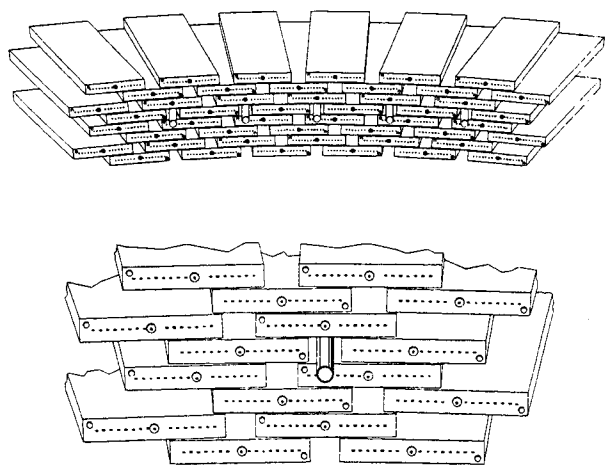

Figure 2.10: The layout of the drift tubes in a 15° wedge of the Central Muon Extension (CMX) muon system. The tubes are mounted on four free standing arches which span 240° in ϕ and cover the pseudorapidity region $0.6 \lesssim |\eta| \lesssim 1.0$.

in the four layers, but no measurement is made of the z position. Track stubs in the CMP are used as confirmation for stubs found in the CMU chambers.

The CMX chambers extend the central muon coverage to the pseudorapidity region $0.6 \lesssim |\eta| \lesssim 1.0$ and cover 240° in azimuth as shown in Figure 2.2. The muon coverage in η-ϕ of the CMX is indicated in Figure 2.9. The CMX chambers are mounted on four free-standing arches adjacent to the central detector. There are eight layers of drift chambers grouped into four radially aligned pairs (see Figure 2.10). Adjacent layers are offset by a half cell. The distance in ϕ between adjacent sense wires is a function of η due to the conical geometry. High-p_t muons typically traverse between four and six drift chambers. Scintillator planes (called CSX) are mounted on both sides of the CMX. During Run 1B data taking, the CSX were used in the trigger to reject spurious triggers from low energy particles passing through the CMX chambers.

2.6 Trigger

During normal operations, the Tevatron delivered $p\bar{p}$ collisions at a rate of 287 MHz. The typical luminosities achieved during Run 1A and Run 1B were 0.54×10^{31} cm$^2/s$ to 1.6×10^{31} cm$^2/s$. The effective $p\bar{p}$ inelastic cross section is roughly 50 mb. So there is at least one inelastic interaction per crossing. The task of the trigger is to reduce the event rate from 287 MHz down to a tape-writing limited speed of $\sim$ 10 Hz while keeping the interesting events and minimizing the deadtime. To this end, CDF employs a three level triggering system. Each level reduces the event rate such that succeeding level may make increasingly more sophisticated and time consuming decisions.

The Level 1 trigger system consists of three main components: coincidence hits between east and west beam-beam counters (BBC); single calorimeter towers over E_t threshold; and muon chamber track stubs over p_t threshold.

The beam-beam counters (BBC) consist of a plane of 16 scintillation counters

mounted on the front face of the east and west forward calorimeters. They form a rectangular frame about the beam pipe arranged very close to the beam pipe: polar angles $0.32° < \theta < 4.47°$ and $175.53° < \theta < 79.68°$. The BBC's record low angle particles from inelastic $p\bar{p}$ collisions. A coincidence in at least one of the BBC counters on each side of the collision in time with the beam crossing serve as the so-called minimum bias trigger. The BBC coincidences are not required in other triggers, discussed below, except during the beginning of Run 1A.

The BBC counters also serve as the primary luminosity monitor. The rate (number) of BBC coincidences divided by the effective cross section of the counters is used to determine the instantaneous (integrated) luminosity. The CDF Collaboration recently published direct measurements of the inelastic and total $p\bar{p}$ cross sections [57, 58, 59]. This allows for a direct measurement of the effective BBC cross section, $\sigma_{BBC} = 51.2 \pm 1.7$ mb. After accounting for backgrounds in the BBC's, the total uncertainty on the integrated luminosity is 3.6% [96] for Run 1A. The best estimate for the uncertainty for Run 1B data is 8% [97], based on the observed rate of $p\bar{p} \rightarrow J/\psi\, X$ events.

The Level 1 calorimeter trigger uses the analog signals from the calorimeter to form transverse energy sums, and the sums are compared to programmable thresholds. This trigger was used for inclusive electron and jet events. The calorimeter detector segmentation described above is made more coarse by performing fast analog sums on the signals. The hadronic and electromagnetic towers are summed separately. The calorimeter trigger segmentation is $0.2 \times 15°$ in $\eta \times \phi$ which results in a more manageable 2048 trigger towers. Each trigger tower is weighted by $\sin\theta$ where θ is the detector polar angle. This allows the trigger to set a threshold based on $E_t = E \sin\theta$. The event z vertex is always assumed to be at $z = 0$ cm. The E_t thresholds are applied separately to six regions, (central, plug, forward) $\times$ (electromagnetic, hadronic). The Level 1 trigger is satisfied when a single trigger tower E_t exceeds the threshold. During Run 1A, Level 1 trigger E_t thresholds for electron and jet triggers were 6 GeV for the

CEM, 8 GeV for the CHA, PEM, and FEM. The PHA and FHA thresholds ranged from 12 GeV to 51 GeV. During Run 1B, the Level 1 thresholds were 8 GeV for the CEM, 11 GeV for the PEM, 12 GeV for the CHA, and 51 GeV for the FEM, PHA and FHA.

The Level 1 muon triggers [98] require hits in the sense wires of the muon chambers. Muons are deflected while inside the axial magnetic field. After exiting the solenoid, they resume a straight path to the muon chambers. The trajectory through the muon chambers forms an angle with respect to the radial path, as indicated in Figure 2.8. The size of this angle is a function of the amount of deflection experienced in the magnetic field which, in turn, is a function of the muon p_t. This angle is measured by the Level 1 trigger by making fast analog measurements of the times t_2 and t_4. The muon p_t is determined from the difference $\Delta t = t_4 - t_2$. This is done for the CMX and CMU chambers. The CMP stubs are formed by a simple coincidence in hits between chambers in alternate layers. The CMU triggers require a track stub with $p_t > 6$ GeV/c and a stub in the CMP except in the regions where there is no CMP coverage. If there is no CMP coverage behind the CMU chamber, then the CMU hits are required to be coincident in time with TDC's in the associated hadron calorimeter wedge. The CMX trigger requires a muon track stub with $p_t > 10$ GeV/c which is in-time with signals from the CSX scintillators and associated hadron TDC's. This particular CMX trigger was implemented only for Run 1B data taking. Therefore CMX muon triggers in Run 1A data are not used.

The Level 1 trigger decisions are made entirely between successive beam crossings, and hence cause no dead time. The Level 1 trigger reduces the event rate to a few thousand per second. Upon receipt of a Level 1 trigger, the detector signals are held until the Level 2 trigger makes a decision in about 20 μs. During this time, subsequent beam crossings are ignored, which incurs a dead time of a few percent. With the additional processing time, the Level 2 trigger [99] is able to make more sophisticated decisions based on five main items: hadronic and electromagnetic

calorimeter clustering; fast CTC track pattern recognition (CFT tracks); matching Level 1 muon stubs to CFT tracks; matching calorimeter clusters to CFT tracks; and global energy sums (total, transverse, and missing transverse energy).

Hardware processors perform the Level 2 calorimeter clustering. A fast nearest-neighbor algorithm is used to locate clusters. Two sets of thresholds are applied to all calorimeter trigger towers to identify seed and shoulder towers. The seed towers are ordered sequentially in η-ϕ space. Next, the four towers adjacent in η-ϕ to the seed are tested to see whether they pass the seed or shoulder thresholds. If a tower E_t is below both thresholds, the tower is not added to the cluster. All towers adjacent to the newly included towers are also checked and included in the cluster if they pass the threshold. The process is repeated for each subsequent tower over threshold until no additional towers are found. The E_t and average η and ϕ are calculated. More than one clustering pass can be made at Level 2, allowing for separate clustering for jets (electromagnetic and hadronic E_t combined), and photons or electrons (electromagnetic E_t only). The seed and shoulder tower E_t thresholds for electromagnetic clusters used in this analysis are 9 GeV and 7 GeV, respectively. For jet clusters, the seed and shoulder tower thresholds are $E_t > 3$ GeV and $E_t > 1$ GeV, respectively.

The Central Fast Tracker (CFT) [100] is a hardware processor which makes use of fast hit information from the five axial *superlayers*. Charged particles which pass through the CTC will deposit charge on nearby sense wires. The particle's distance from the wires determines the time of arrival at the sense wires. The arrival times are arranged into a pattern of hits. These are compared to pattern recognition lookup tables to identify tracks in the r-ϕ view falling in one of eight p_t bins. The p_t of the tracks can be measured with a resolution of $\frac{\delta p_t}{p_t^2} \sim 3.5\%/$ GeV.

The Level 2 muon trigger matches a Level 1 muon stub to a corresponding CFT track. The Run 1A Level 2 muon triggers used in this analysis require a CFT track with $p_t > 9.2$ GeV/c^2 matching in ϕ to a Level 1 muon stub in the CMU or CMP

[2]The p_t threshold represents the 90% efficiency point of the 10 GeV/c p_t bin

chambers. For Run 1B data taking, the CFT track threshold was increased to $p_t >$ 12 GeV/c. Also for Run 1B data, the Level 2 muon triggers used in this analysis have the added requirement of a Level 2 jet cluster with $E_t > 15$ GeV. These are referred to as "muon + jet" triggers.

The Level 2 electron triggers used in the leptoquark analysis require an electromagnetic cluster with an associated CFT track. Only clusters in the CEM are used. For the Run 1A electron data sample used here, the Level 2 electron trigger required an electron cluster with $E_t > 9$ GeV matching to a CFT track with $p_t > 9.2$ GeV/c. A similar trigger was used for the Run 1B sample, but the E_t threshold was increased to $E_t > 16$ GeV and the CFT threshold was increased to $p_t > 12$ GeV/c. The Run 1A and Run 1B triggers both require E_t in the hadronic compartments behind the cluster to be less than 12.5% of the electron cluster E_t.

The Level 2 trigger reduces the event rate down to 20-35 Hz. When a Level 2 trigger is satisfied, all detector channels are digitized and sent to the Level 3 trigger system [101]. Digitization takes typically two to three milliseconds. The Level 3 trigger runs independently from the Level 1 and Level 2 triggers. Thus after Level 3 receives the event the detector is available to test subsequent beam crossings for Level 1 and Level 2 triggers.

The Level 3 trigger is software-based. It consists of a farm of Silicon Graphics computers which run a variant of the offline reconstruction algorithms (Chapter 3). Most of the Level 3 processing is written in FORTRAN. The Level 3 filters applicable in this analysis apply electron and muon identification requirements less stringent than those described in the next chapter. Events passing the Level 3 selection algorithms are written to tape.

Chapter 3

Data Reconstruction and Lepton Identification

In the topic of this thesis, $p\bar{p}$ interactions produce leptoquark pairs which result in final states with two taus plus two jets. The taus are not directly observed in the detector; rather the decay products are. The decay modes and branching fractions for taus are listed in Table 1.2.2. These decays produce characteristic signatures in the detector. The leptonic tau decays are observed by the presence an electron or muon. The hadronic tau decays form a signature in the detector similar to that of a jet. All tau decay channels involve neutrinos, which are not observed in the detector. In this chapter, the reconstruction of these objects is described. First, the calorimeter energy measurement is presented. These calorimeter energy depositions also serve as the starting point for jet clustering. Jets from QCD sources, quarks and gluons, form backgrounds to identifying the leptons. The methods for reconstructing and identifying the electrons, muons, and taus and the quantities which distinguish them from jets are discussed next. Finally, the neutrino reconstruction is described.

3.1 Calorimeter Energy

The calorimeter energy reconstruction forms the magnitude and position of the energy depositions in the calorimeters. The signal from each calorimeter channel is converted to energy with detector-dependent scale factors. Several corrections and cleanup algorithms are applied to remove spurious sources of energy in the calorimeter. The energies from individual detector systems are then merged into a global map of depositions in the η-ϕ plane.

The transverse energy (E_t) of each tower is calculated using the tower's polar angle, θ, relative to the event z-vertex: $E_t = E \sin\theta$. The vertex time-projection chamber (VTX) provides a measurement of the z vertex from tracks reconstructed in the r-z view. Clusters of tracks emanating from a common point along the beam line define an event vertex, and the vertex with the most VTX tracks is used as the primary vertex for electron and jet clustering.

3.2 Jet Reconstruction

Energetic quarks and gluons fragment into a collimated spray of hadrons roughly parallel to the parton direction. During fragmentation, the hadrons acquire momentum perpendicular to the parton direction causing the jet typically to spread over many calorimeter towers. To estimate the momentum and direction of the parent quark or gluon, the tower energies are clustered to form *jets*.

3.2.1 Jet Clustering Algorithm

There are three stages to the CDF jet clustering algorithm: preclustering, clustering, and handling of overlapping clusters. First, seed towers are defined to be towers with total $E_t > 1$ GeV (EM+HAD) and are ordered by decreasing E_t. Candidate towers are those with total $E_t > 0.1$ GeV. A precluster is formed by merging adjacent seed

towers with continuously decreasing E_t until no more towers can be incorporated. The process is repeated for all seed towers which are not already contained in a precluster.

A precluster is the starting point for the iterative clustering procedure. The E_t-weighted centroid of the precluster is calculated. Then a cone of fixed radius $R = \sqrt{(\Delta\eta)^2 + (\Delta\phi)^2} = 0.4$ in η-ϕ space is placed on the precluster centroid, and all candidate towers within the cone are merged into the cluster. The cluster centroid is calculated, a new cone is made, and candidate towers are merged again. The process is repeated until the list of towers in the cluster is unchanged. The procedure is repeated for the the remaining preclusters.

Finally, cases of overlapping clusters are resolved. If two clusters share common towers, the sum E_t of the overlap towers is calculated. If the sum is greater than 75% of either cluster E_t, then the two clusters are merged and a new centroid calculated. If the shared fraction is less than 75% of the smaller cluster E_t, then the two clusters are split. Each shared tower is assigned to the closer cluster, and new centroids are found. The overlap fraction is recalculated and checked again. The cluster merging and splitting continues until the list of towers in the each cluster is unchanged. This is repeated for each pair of overlapping clusters.

The jet cluster E_t is formed by the scalar sum E_t of all towers associated with the cluster. The jet direction is given by the η-ϕ centroid of the towers. The electromagnetic fraction (EMF) is the ratio of the energy in the electromagnetic towers to the total energy.

3.3 Central Electrons

Electrons form a distinct signature in the CDF detector. Most importantly, nearly all of the energy is deposited in the EM calorimeter compartment. The transverse shower size, typically 3 cm radius, is small compared to the tower size, and so will be contained in one or two CEM towers. Also, when an electron passes through the

CTC, it leaves a trail of ionization in the gas which is reconstructed as a track. This track will have a momentum roughly equal to the shower energy measured in the CEM, and the trajectory will point to the shower position in as determined in the proportional tubes embedded in the CEM.

Hadronic jets are the largest background to identifying a pure sample of electrons. The jet fragmentation can fluctuate such that only a few hadrons emerge, giving the jet many of the characteristics of the electron shower described above. For instance, a single charged pion can shower in the EM calorimeter via the reaction $\pi^- p \rightarrow n\pi^\circ$. However, if the pion interacts late in the CEM, there may be significant leakage into the hadron compartment. Also a charged pion overlapping with a neutral pion can also produce an EM shower with an associated track. In this case, the track momentum will not match the shower energy or point to the shower position in general.

These features of electron showers and the processes that can mimic them are the motivation for the electron clustering algorithm and identification variables discussed in the next sections.

3.3.1 Electron Clustering Algorithm

The electron clustering begins by finding towers which will form the "seed" for the cluster. Seed candidates are those towers with electromagnetic (EM) $E_t > 3$ GeV. Once a seed tower is found, nearest-neighbor towers in η with EM $E_t > 0.1$ GeV are incorporated into the cluster. If the adjacent tower has an E_t larger than the seed tower, it becomes the new seed tower, and only towers adjacent to it are considered. This merging continues until either no more towers can be added, or the maximum number of towers for the cluster is reached. In the CEM, the maximum cluster dimension is 3×1 in $\eta \times \phi$. The cluster is kept if it has EM $E_t > 5$ GeV and if the ratio of energy in the hadronic calorimeter to that in the electromagnetic calorimeter is less than 0.125. The electron 4-momentum is calculated using the electron cluster

energy and the direction of the associated track.

3.3.2 Electron Variable Definitions

The variables used to identify central electrons are listed below. The distributions of each variable are shown in Figures 3.1 and 3.2. These distributions are from isolated electrons in the $Z \rightarrow ee$ samples discussed in Section 3.3.5.

- E/p The ratio of the corrected electron energy (E) from the CEM to the associated track momentum (p) measured in the CTC. The track is constrained to come from the beam position. The mean of this ratio peaks at 1 and the width is affected by the electron energy and momentum resolutions. The ratio acquires a tail at values > 1 due to photon radiation: the energy carried off by the photons is measured in the CEM, but not by the electron track.

- LSHR The lateral energy sharing with towers adjacent in η to the electron seed tower. The expected sharing measured from testbeam electrons is compared to the observed sharing, given the position of the cluster in the CES. The quantity LSHR is defined as

$$\text{LSHR} = 0.14 \times \sum_i \frac{E_i^{meas} - E_i^{pred}}{\sqrt{\left(0.14\sqrt{E}\right)^2 + \left(\delta E_i^{pred}\right)^2}} \tag{3.1}$$

  where the sum is over the towers adjacent to the seed tower, E_i^{meas} is the measured tower energy, E_i^{pred} is the expected energy in that tower based on the electron position in the strip chambers, δE_i^{pred} is the uncertainty on E_i^{pred} associated with a 1 cm uncertainty in the strip chamber position measurement, and E is the electron cluster energy.

- χ^2_{strip} The transverse spread of the shower in the z direction measured by the CES strip chambers is compared to the shape from testbeam electrons, and a chi-squared test is performed.

- Δx The difference in the ϕ direction between the electron CES wire chamber position and the extrapolated track position at the CES.

- Δz The difference in the z direction between the electron CES strip chamber position and the extrapolated track position at the CES.

- HAD/EM The ratio of energy in the hadronic compartment (HAD) to the energy in the electromagnetic compartment (EM).

Leptons from decays of b or c quarks typically have nearby jet activity, whereas leptons from W, Z, or leptoquark decays are well-isolated from other activity in the event. The electron isolation in the calorimeter can separate leptons from quark or heavy boson decays. The isolation is defined as

$$I_{cal} = \frac{E_t(0.4) - E_t^{ele}}{E_t^{ele}} \tag{3.2}$$

where $E_t(0.4)$ is the amount of transverse energy inside a cone of radius $R = \sqrt{(\Delta\eta)^2 + (\Delta\phi)^2}$ centered on the electron. Requiring a small value of I_{cal} suppresses leptons from b or c decays.

3.3.3 Electron Fiducial Region

The electrons are restricted to a fiducial region of the central calorimeter in which the calorimeter response is well understood. This region is defined so that electron detection efficiency is uniform and the energy calibration is reliable. This is accomplished in the CEM by excluding uninstrumented regions of the central calorimeter or regions near the calorimeter module boundaries. Two requirements are made on the electron seed tower. The seed tower must not be in the outermost CEM towers in η. Also. the seed tower must not be the tower containing access to the cryostat. Additional requirements are made on the electron cluster based on the position information from the CES strip and wire chambers. The electron position in ϕ must be within 21 cm

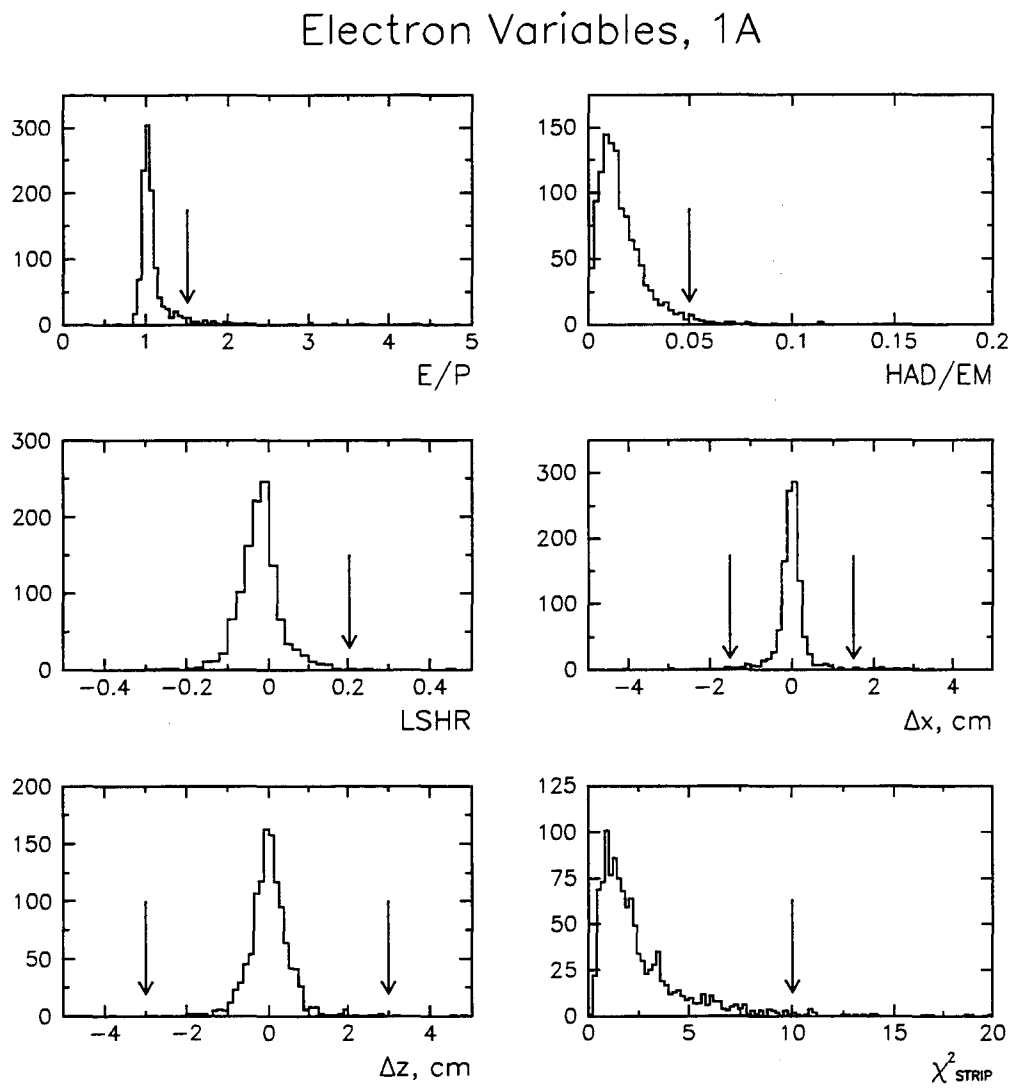

Figure 3.1: Central electron identification variables from $Z \rightarrow ee$ events in Run 1A data. The arrows indicate the strict electron identification criteria.

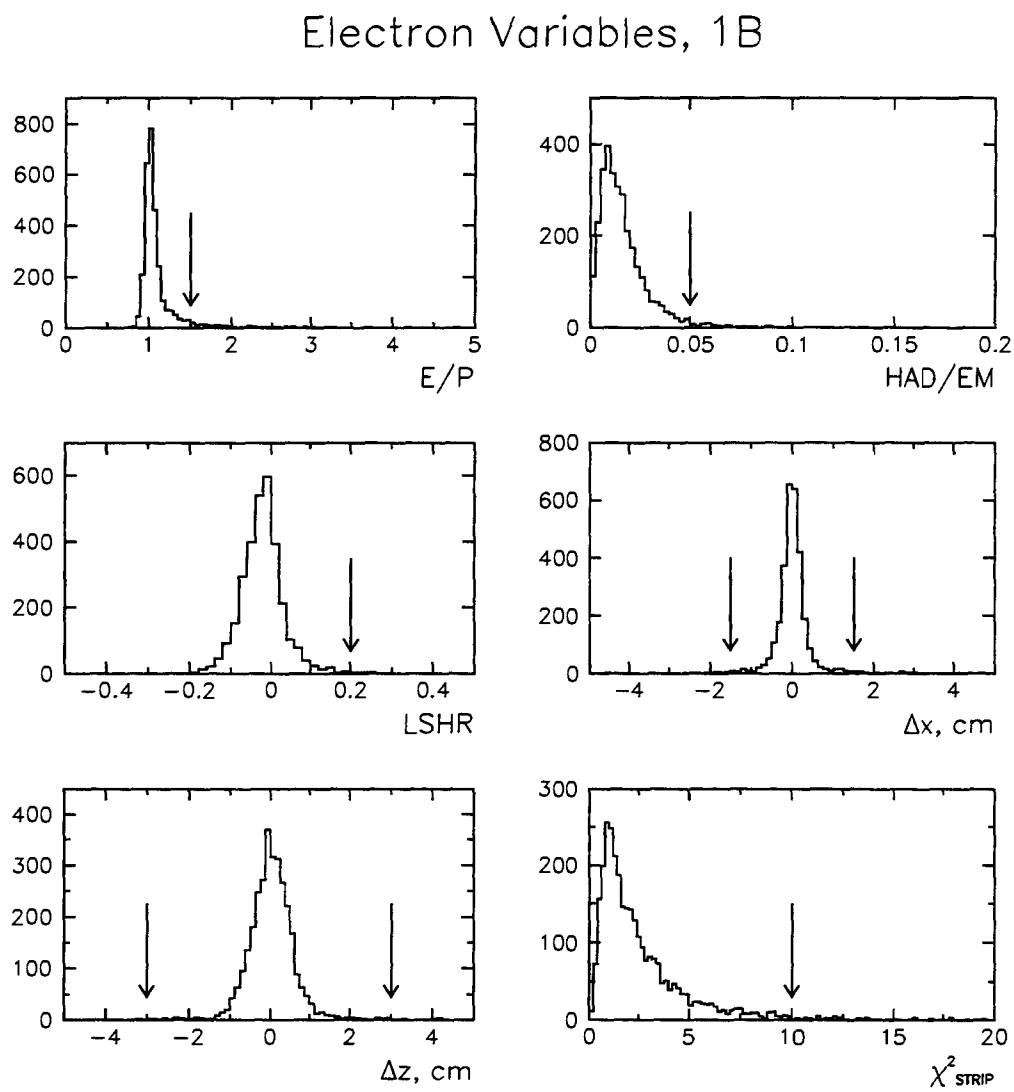

Figure 3.2: Central electron identification variables from $Z \rightarrow ee$ events in Run 1B data. The arrows indicate the strict electron identification criteria.

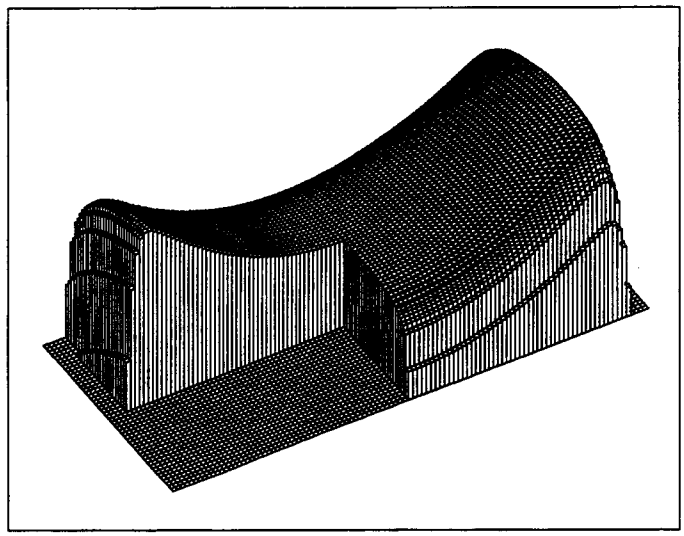

Figure 3.3: The Central Electromagnetic (CEM) calorimeter response map shows the dependence of the response on the electron position within a typical tower. Each tower has a slightly different response. The local x and z directions (ϕ and η) are roughly left-right and up-down on the page, respectively.

of the tower center. This requires electrons to be more than 3 cm away from the 15° CEM wedge boundaries. The electron position in the z direction must be more than 9 cm away from the $z = 0$. This excludes the region where the east and west halves of the central central meet. The electron fiducial volume covers 84% of the solid angle in the region $|\eta| < 1.0$.

3.3.4 Energy Corrections

The following corrections are made to the electron energy to account for known sources of variations.

Response map corrections: The measured electron energy depends on the position of the electron within the CEM tower. The relative response within each tower was mapped using testbeam electrons. A correction function derived from

$E/p < 1.5$
$LSHR < 0.2$
$\chi^2_{strip} < 10.0$
$\lvert\Delta x\rvert < 1.5$ cm
$\lvert\Delta z\rvert < 3.0$ cm
$HAD/EM < 0.05$

Table 3.1: Electron identification requirements

test beam data is used to remove the position dependence. The corrections within a typical CEM tower are shown in Figure 3.3

Tower-to-tower corrections: Each CEM tower has a slightly different response to electrons. The average E/p distribution is made for each tower from large samples of inclusive electrons. For each tower a correction factor is found which removes tower-to-tower variations. Also, there are residual response variations as a function of η-ϕ position in the CEM wedge. This dependence is measured and removed.

Time variations: The gain of the CEM was seen to decrease linearly with time. This was observed as a decrease in $< E/P >$ with time. This was due in part to aging of the scintillator which reduces the light yield collected at the phototubes. This dependence is parametrized and removed [50].

Absolute scale: The CTC momentum scale has been calibrated using dimuons from J/ψ and Υ decays. The absolute CEM energy scale is tied to the CTC scale by comparing the E/p distribution from $W \rightarrow e\nu$ events to the predictions from a W Monte Carlo which includes radiative effects [50].

3.3.5 Electron Identification Criteria and Efficiencies

High-E_t central electrons are identified using the requirements listed in Table 3.1. The efficiencies of the requirements are estimated from samples of $Z \rightarrow ee$ events. The sample is selected from the inclusive high-E_t electron samples (Chapter 4) using the following criteria:

$Z \rightarrow ee$ Sample Selection

1. Two central electrons with corrected $E_t > 20$ GeV in the fiducial region defined in Section 3.3.3. At least one of the electrons must satisfy all identification criteria in Table 3.1.

2. Both electrons must be isolated in the calorimeter: $I_{cal} < 0.1$.

3. The event vertex must satisfy $|z_v| < 60$ cm

4. The dielectron mass must fall in the range 75 GeV/c^2 $< M_{ee} <$ 105 GeV/c^2.

There 586 events in the Run 1A $Z \rightarrow ee$ sample and 1552 events in the Run 1B $Z \rightarrow ee$ sample.

The efficiencies are determined using the following argument. Suppose there are N_Z $Z \rightarrow ee$ events passing the Z sample selection with no identification requirements. Then if $Z \rightarrow e_1 e_2$, either electron can satisfy the identification requirements. For a given requirement with efficiency ε, four possibilities can occur:

	Number of Events
a) Both electrons pass requirement	$\varepsilon^2 N_Z$
b) e_1 passes, e_2 fails	$\varepsilon(1-\varepsilon)N_Z$
c) e_1 fails, e_2 passes	$(1-\varepsilon)\varepsilon N_Z$
d) Both electrons fail requirement	$(1-\varepsilon)^2 N_Z$

The events in categories (a), (b), and (c) enter into the Z sample described above. In events in category (d), neither electron satisfies the strict identification criteria, so

Requirement	ε, 1A	ε, 1B
$E/p < 1.5$	90.7 ± 0.9	88.7 ± 0.6
$LSHR < 0.2$	99.1 ± 0.3	98.6 ± 0.2
$\chi^2_{strip} < 10.0$	96.5 ± 0.6	96.9 ± 0.3
$\lvert\Delta x\rvert < 1.5$ cm	94.2 ± 0.7	94.6 ± 0.4
$\lvert\Delta z\rvert < 3.0$ cm	98.9 ± 0.3	99.0 ± 0.2
$HAD/EM < 0.05$	97.5 ± 0.5	96.8 ± 0.3
Total	83 ± 1	80.0 ± 0.9

Table 3.2: Electron identification efficiencies from the $Z \rightarrow ee$ samples

the events do not enter the $Z \rightarrow ee$ sample above. The identification efficiency can be extracted using the number of events in which both electrons satisfy the requirement, N_2, and those in which only one electron satisfies the requirement, N_1, as follows:

$$\begin{aligned} \frac{N_2}{N_2 + \frac{1}{2}N_1} &= \frac{N_Z\varepsilon^2}{\varepsilon^2 N_Z + \frac{1}{2}\left[\varepsilon(1-\varepsilon)N_Z + (1-\varepsilon)\varepsilon N_Z\right]} \\ &= \varepsilon \end{aligned} \tag{3.3}$$

The identification efficiencies are listed in Table 3.2. The total identification efficiency for central electrons is $(83 \pm 1)\%$ from the Run 1A sample and $(80.0 \pm 0.9)\%$ from the Run 1B sample.

3.4 Central Muons

Muon reconstruction exploits the characteristics of the muons' passage through matter. Muons are charged particles and thus will leave a trail of ionization in the Central Tracking Chamber (CTC). However muons are minimum ionizing particles, depositing only a small amount of their energy in the EM calorimeter. Since muons do not

interact strongly, they will penetrate the hadron calorimeter also. From testbeam data and cosmic ray studies, muons typically leave 2 GeV and 0.4 GeV in the hadron and EM compartments respectively. After exiting the calorimeters the muons with $|\eta| < 1$ pass through the central muon (CMU) or central muon extension (CMX) drift chambers. In the central region with $|\eta| \lesssim 0.6$, muons pass through additional steel and traverse the central muon upgrade (CMP) drift chambers. Thus the signature of a muon is a track in the CTC which points to calorimeter towers with minimum ionizing energy deposition and which matches to track stub(s) in the muon drift chambers.

Backgrounds to muons fall into three categories: a) fake muons, b) muons from pion or kaon decays or cosmic rays, and c) muons from other primary sources. The chief source of fake muons is charged pions which penetrate to the muon chambers. The calorimeter requirement reduces most of this background, but some pions will pass through the calorimeter without depositing all their full energy and "punch through" to form stubs in the CMU or CMX chambers. The punch-through background is reduced in some regions of the CMU chambers by requiring a stub in the muon upgrade chambers where CMP coverage available (see Figure 2.9). In the next class of backgrounds, a muon from a secondary source produces a track stub in the muon chambers. These can be cosmic ray muons or muons from the decays-in-flight of charged mesons, e.g. $\pi/K \rightarrow \mu\nu$. If the neutrinos from the meson decay carry enough momentum, there may be a kink in the charged particle trajectory where the decay occurs. Then the reconstructed track may appear to originate from a point separated from the beam position.

The muon 4-momentum is given by the track momentum. The muon track is constrained to originate from the event vertex – a "beam constraint." By including the beam position in the muon trajectory, the effective path length measured in the magnetic field increases from 1.0 m to 1.3 m. This improves the momentum resolution of the muon.

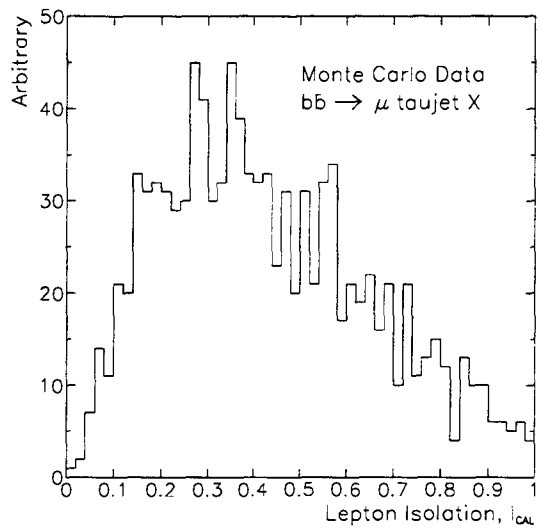

Figure 3.4: The isolation, I_{cal}, for central muons $p_t > 20$ GeV in simulated $b\bar{b}$ events. The events are generated with the Pythia Monte Carlo and passed through a simulation of the CDF detector. Leptons from the decays of B hadrons are expected to be less isolated than those from the decays of heavy bosons (eg. $W^{\pm}$, Z°, leptoquarks).

3.4.1 Muon Variable Definitions

The variables listed below are used to define candidate muons. The distributions for each variable are shown in Figures 3.5–3.7 for isolated muons in the $Z \rightarrow \mu\mu$ samples discussed in Section 3.4.2.

- d_0 The impact parameter of the muon track. This is the distance of closest approach of the muon track to the beam x-y position. This point in the trajectory also defines the z vertex of the muon track.

- E_{EM} The energy of the electromagnetic calorimeter towers traversed by the muon.

- E_{HAD} The energy of the hadronic calorimeter towers traversed by the muon.

- Δx The difference in the ϕ direction between the position of the muon stub and the position of the track extrapolated to the muon chambers. Muons which hit the CMX or CMP pass through more pion absorption lengths in the calorimeter, and thus experience more multiple scattering than muons at the CMU. Therefore the resolution of the CMU stub matching is better than for the CMX or CMP

- ΔZ_{vert} The difference between the muon track z vertex and the nearest event z vertex found in the VTX chamber.

A filter algorithm is used to reject muons from cosmic rays. Cosmic rays can enter one side of the detector forming two tracks in the CTC that are back-to-back in η-ϕ and then exit the detector. These events are generally not associated with a $p\bar{p}$ collision or in time with the beam crossing. Furthermore, one leg of the muon trajectory is separated in time from the other leg. A filter is used to remove cosmic ray muon candidates based on these features. Cosmic ray muon candidates are flagged if the z vertex of the muon track is not close to an event z-vertex, if the muon has a poor-quality track opposite in η-ϕ, or if the opposing track is significantly shifted in time from the primary muon track.

$E_{EM} < 2.0$ GeV
$E_{Had} < 6.0$ GeV
CMU $\lvert\Delta x\rvert < 2.0$ cm
CMP $\lvert\Delta x\rvert < 5.0$ cm
CMX $\lvert\Delta x\rvert < 5.0$ cm
$\lvert d_0\rvert < 0.3$ cm
$\lvert\Delta Z_{vert}\rvert < 5$ cm
Cosmic Ray Filter

Table 3.3: Muon identification criteria. CMUP muons must satisfy both the CMU and CMP chamber Δx requirements.

The muon isolation in the calorimeter is defined similarly to that of the electron.

$$I_{cal} = \frac{E_t(0.4) - E_t^{\mu}}{p_t^{\mu}} \tag{3.4}$$

where $E_t(0.4)$ is the amount of transverse energy inside a cone of radius $R = \sqrt{(\Delta\eta)^2 + (\Delta\phi)^2}$ centered on the muon, E_t^{μ} is the E_t of the towers traversed by the muon, and p_t^{μ} is the muon track transverse momentum measured in the CTC. As with electrons, I_{cal} is used to reduce muons from b or c hadron decays. The muon isolation distribution for simulated $b\bar{b} \rightarrow \mu X$ events (see Section 5.2.5) is shown in Figure 3.4.

3.4.2 Muon Identification Criteria and Efficiencies

High-p_t central muons are identified using the requirements listed in Table 3.3. The muon identification efficiencies are estimated from samples of $Z \rightarrow \mu\mu$ events. These are selected from high-p_t inclusive muon samples (Chapter 4) using the following criteria:

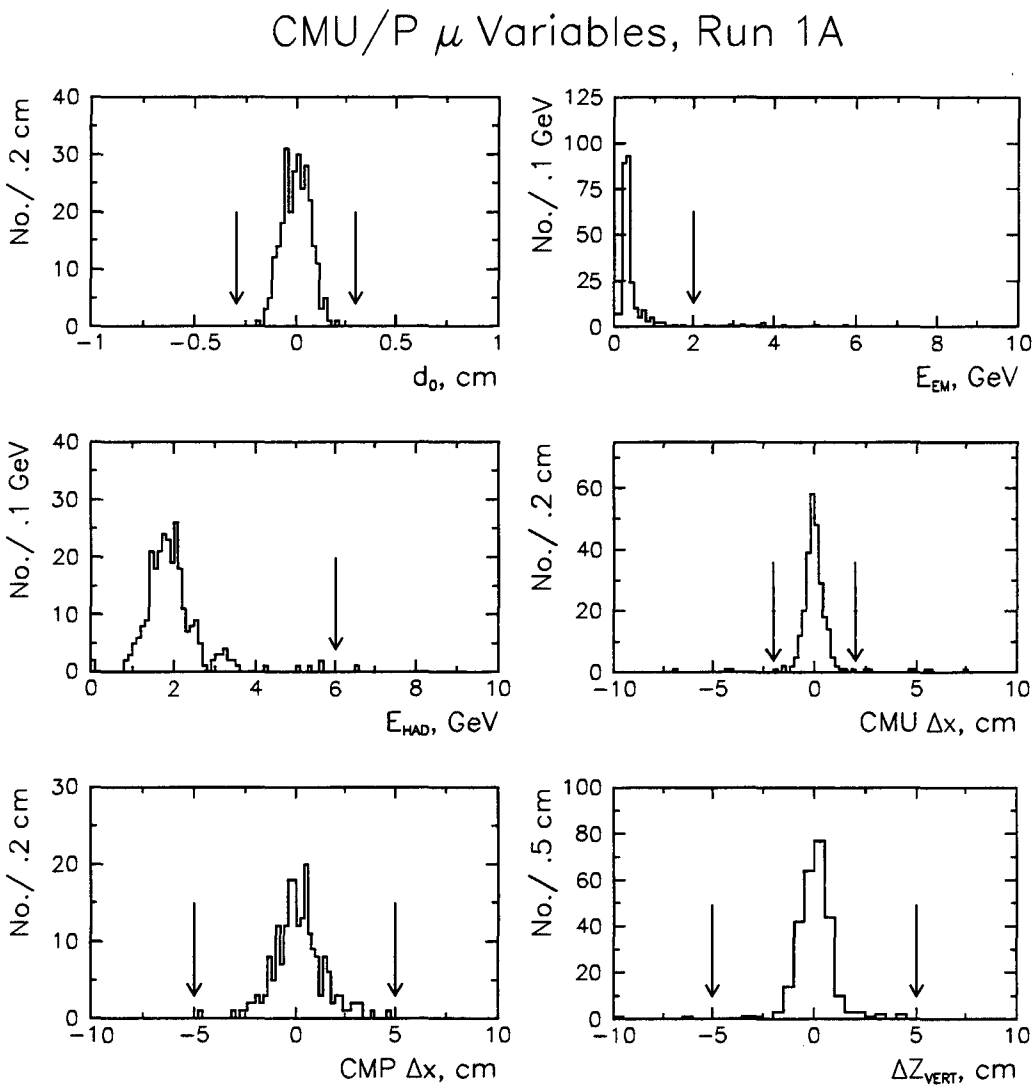

Figure 3.5: Central muon (CMU/P) identification variables from $Z \rightarrow \mu\mu$ events in Run 1A data. The arrows indicate the strict identification criteria.

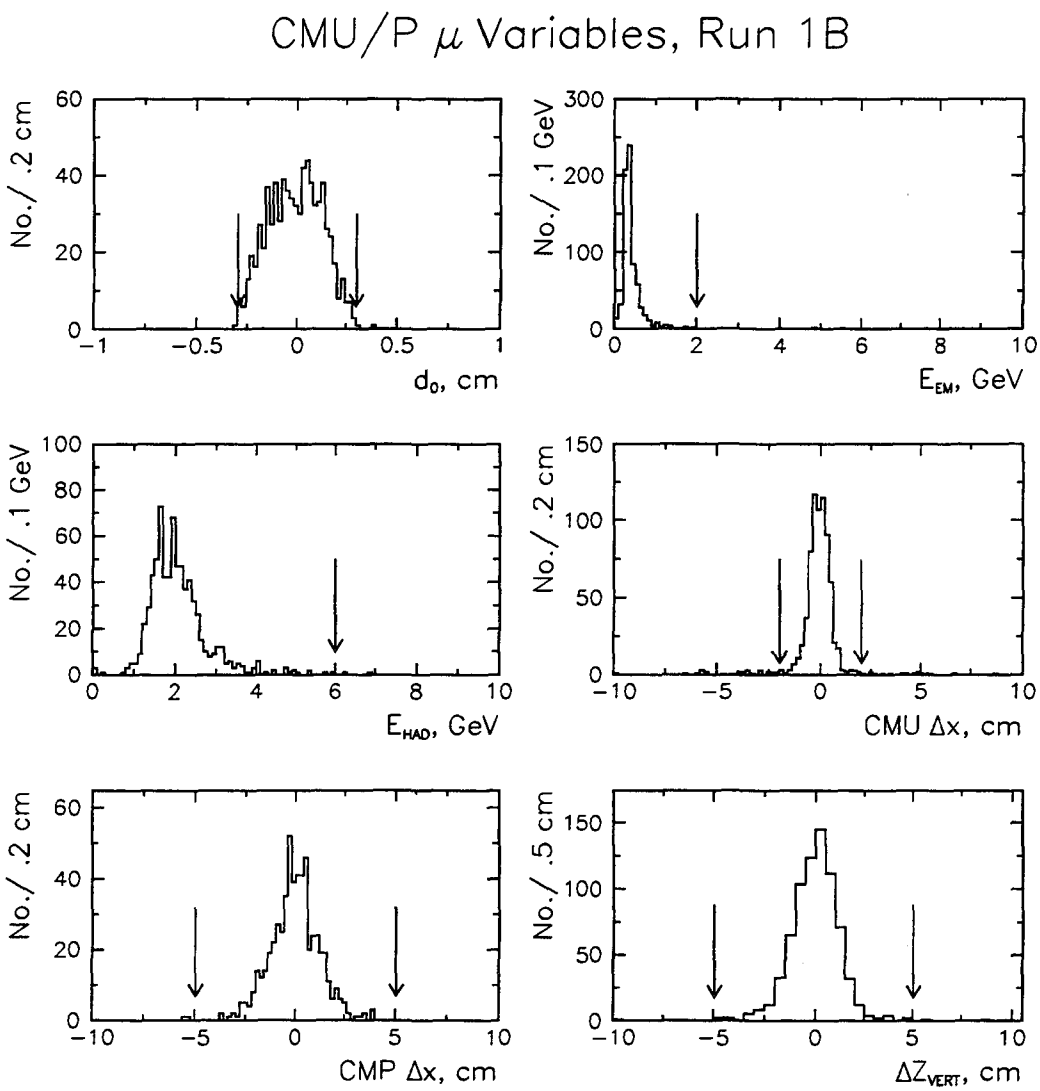

Figure 3.6: Central muon (CMU/P) identification variables from $Z \rightarrow \mu\mu$ events in Run 1B data. The arrows indicate the strict identification criteria.

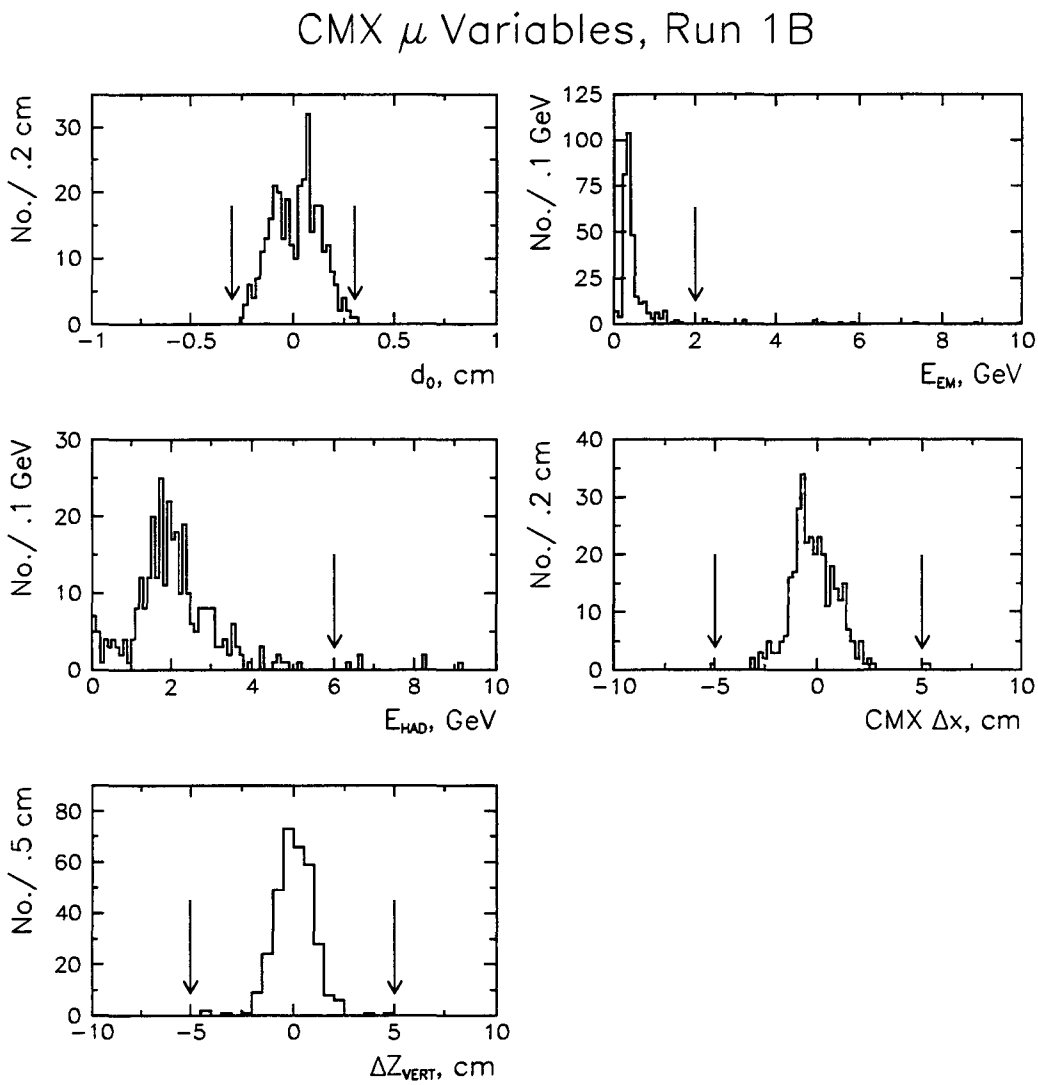

Figure 3.7: Central muon (CMX) identification variables from $Z \rightarrow \mu\mu$ events in Run 1B data. The arrows indicate the strict identification criteria.

Requirement	CMU and CMUP Muon ε, 1A	CMU and CMUP Muon ε, 1B	CMX Muon ε, 1B
$E_{EM} < 2.0$ GeV	96 ± 1	97.5 ± 0.6	95 ± 1
$E_{Had} < 6.0$ GeV	99.3 ± 0.5	99.2 ± 0.3	97.0 ± 0.9
CMU, CMP $\|\Delta x\|$	95 ± 1	93 ± 1	—
CMX $\|\Delta x\| < 5.0$ cm	—	—	99.1 ± 0.55
$\|d_0\| < 0.3$ cm	100 ± 0.5	99.6 ± 0.2	99.7 ± 0.3
$\|\Delta Z_{vert}\| < 5$ cm	98.9 ± 0.6	99.1 ± 0.4	100 ± 0.3
Cosmic Ray Filter	98.9 ± 0.6	98.8 ± 0.4	100 ± 0.3
Total	90 ± 2	89 ± 1	91 ± 2

Table 3.4: Central muon identification efficiencies from the $Z \rightarrow \mu\mu$ samples.

$Z \rightarrow \mu\mu$ Sample Selection

1. Three types of muons are considered:

   (a) CMX: The muon has a track which extrapolates to a stub in the CMX detector.

   (b) CMUP: The muon has a track which extrapolates to the CMU *and* CMP chambers, and has stubs in *both* chambers.

   (c) CMU-only: The muon has a stub in the CMU chambers and a track which extrapolates to the CMU chambers but *not* to the CMP chambers.

   Then two opposite-charge muons with beam-constrained $p_t > 20$ GeV are required. At least one must pass the identification requirements in Table 3.3. For CMUP muons, both $|\Delta x|$ matching requirements must be satisfied.

2. Both muons must be isolated in the calorimeter: $I_{cal} < 0.1$

3. The event vertex must satisfy $|z_v| < 60$ cm

4. The $Z \rightarrow \mu\mu$ events are classified according the $\mu\mu$ topology:

   (a) CMX-CMX: Two CMX muons

   (b) CMX-CMU/P: One CMX muon and one CMU-only or CMUP muon

   (c) CMU/P-CMU/P: Two CMU-only or CMUP muons, any combination.

   The event must be of CMX-CMU/P or CMU/P-CMU/P topology. For the CMX-CMU/P case, the CMU/P muon must pass the identification requirements.

5. The dimuon mass must fall in the range 75 GeV/c^2 < $M_{\mu\mu}$ < 105 GeV/c^2

There 135 events in the Run 1A $Z \rightarrow \mu\mu$ sample and 701 events in the Run 1B $Z \rightarrow \mu\mu$ sample.

The CMP $|\Delta x|$ matching requirement is ~100% efficient, so the CMUP matching efficiencies are dominated by the CMU $|\Delta x|$ matching requirement (the matching requirements are AND'ed for CMUP muons). Therefore the efficiencies for CMU and CMUP muons are calculated together. In this case the identification efficiencies can be calculated with the same arguments for the electrons, using the CMU/P-CMU/P topology. The efficiencies are listed in Table 3.4. The CMU/P muon identification efficiencies determined from the Run 1A and Run 1B $Z \rightarrow \mu\mu$ samples are (90 ± 2)% and (89 ± 1)% respectively.

The number of Z decays with CMX-CMX topology is small, so identification efficiencies determined from such a sample would have large statistical uncertainties. Therefore an alternate method is used to determine the CMX muon identification efficiencies. A sample of CMX-CMU/P Z's is made, accepting only those events where the CMU/P muon satisfies the identification criteria in Table 3.3. The CMX muons then form an unbiased sample of muons since no identification requirements have been made on them. The CMX identification efficiency is then determined by the

ratio of CMX muons which pass the identification requirements to the total number of CMX muons in the sample. The efficiencies for the CMX muon identification requirements are listed in Table 3.4. The total identification efficiency determined from the Run 1B $Z \rightarrow \mu\mu$ sample is $(91 \pm 2)\%$.

3.5 Hadronic Tau Reconstruction: Taujets

The decays of hadronic taus are have been used in several other CDF analyses [93, 94, 95]. This decay channel has substantial backgrounds from quark and gluon jets. These jets contain the same constituents as hadronic tau decays, and are produced more copiously in $p\bar{p}$ interactions than jets from hadronic taus.

However, the characteristics of tau decays can be used to design additional requirements which preferentially select hadronic tau decays or *taujets*. The decay products include only a few hadrons, typically three or fewer, which carry the visible momentum of the tau, i.e. excluding the neutrino. The number of charged hadrons is one or three, hence only one or three high p_t tracks will point to the jet. Also some decay modes contain neutral pions, from $\rho^{\pm} \rightarrow \pi^{\pm}\pi^{\circ}$ for example, which contribute EM energy to the jet. Taus from the decays of heavy leptoquarks ($M \gtrsim 50$ GeV/c^2) are energetic since the tau mass is small. Therefore the tau decay products will be highly collimated, and close to the parent tau direction. Finally taus from leptoquark decays are often well-separated from other activity in the event, so they will be isolated.

Using these features as a guide, the following hadronic tau reconstruction algorithm is defined:

1. A candidate calorimeter jet is found: This is defined as a jet with $E_t > 15$ GeV and $|\eta_d| < 1$ using the jet clustering algorithm described in Section 3.2.1. Here the detector pseudorapidity η_d is calculated assuming the jet originates from $z = 0$, the geometric center of the detector, rather than from the event z vertex.

This ensures that the jet falls in a region with full CTC tracking coverage. The jet cluster E_t, η (using the event z vertex), and ϕ define the tau candidate 4-momentum.

2. A list of candidate tracks is tabulated: These are defined as CTC tracks with $p_t > 1$ GeV/c. Each track must satisfy a minimum hit usage in the axial and stereo superlayers to ensure a good 3-D track, and have a z-vertex within 5 cm of the primary z vertex (the lepton z-vertex in the leptoquark search).

3. Candidate tracks are associated to the jet: Using the axis defined by the event z vertex and jet centroid, a cone of radius 30° is formed about the jet. All candidate tracks within this cone are associated to the jet.

4. Tracks in the inner core of the jet are associated with the tau decay: A cone of radius 10° is formed about the jet axis. All candidate tracks within this cone are assigned to the tau. These tracks are subject to additional requirements to select tau-like jets. These requirements are described in the next section. They are also used to calculate the tau charge, and reject jets consistent with being an electron.

3.5.1 Taujet Variable Definitions

The variables listed below are used to select jets from the hadronic decays of taus. The distributions of the variables used to identify hadronic tau decays are shown in Figures 3.8-3.11 for taus from simulated leptoquark events and for jets from a control sample in lepton + jets data. Both samples are discussed in Section 3.5.3. Jets from quarks or gluons are expected to dominate the control sample. So the distributions from that sample provide a useful comparison to the corresponding distributions from hadronic tau decays.

- p_t^{lead}: The p_t of the most energetic track in the 10° cone

- $\sum p_t$: The summed p_t of all tracks in the 10° cone

- EMF: The electromagnetic fraction of the jet cluster. This is used in conjunction with p_t^{lead} and E_t to reject jets formed by an electron shower.

- $M(trks)$: The mass formed by the tracks in the 10° cone, assigning each track the $\pi^{\pm}$ mass

- $N_{10°}$: The number of charged tracks in the 10° cone.

In order to select $\tau^+\tau^-$ pairs, the charges of the both tau decay products must be determined. For leptonic tau decays, this is simply given by the charge of the lepton. For hadronic tau decays, the tau charge is given by the sum of the decay products' charges. If all the charged decay products are contained within the 10° cone the tau charge is given by $\sum_{10°} Q$, the sum of the track charges in the 10° cone. This is seen in the $\sum_{10°} Q$ and $N_{10°}$ distributions in Figure 3.9. The corresponding distributions in the control sample jets are shown in Figure 3.11. Here, $\sum_{10°} Q$ takes on values other than ± 1 in a larger fraction of quark and gluon jets jets than in hadronic taus. This is a direct consequence of the $N_{10°}$ distribution. The jets with even values of $N_{10°}$ have $\sum_{10°} Q = 0, 2, 4 \ldots$. In order to demonstrate a $\tau^+\tau^-$ signal in the data, the $N_{10°}$ is compared between events with same-charge lepton + jet pairs and opposite-charge pairs. The jets having $\sum_{10°} Q = 0$ cannot be classified this way, so an alternate definition is adopted: the charge of the highest p_t track. This method to assign the jet charge is summarized in $Q_{\tau jet}$:

$$Q_{\tau jet} \equiv \begin{cases} \sum_{10°} Q & \text{if } \sum_{10°} Q = \pm 1 \\ Q \text{ of leading } 10° \text{ track} & \text{otherwise} \end{cases} \tag{3.5}$$

The final taujet variable, N_{isol}, is a measure of the taujet's isolation. N_{isol} is the number of candidate tracks between the 10° and 30° cones. The area between these cones defines the isolation region.

Requirement		$M_{LQ} = 125$ GeV/c^2 Efficiency, %
$p_t^{lead} > 10$ GeV/c	Leading track	
$\Sigma p_t > 20$ GeV/c	for $N_{10^\circ} \geq 3$	81.2 ± 0.8
EMF $< 1 - \frac{p_t}{7E_t}$	Electron Removal	93.9 ± 0.5
$M(trks) < 2$ GeV/c^2		92.7 ± 0.5
1 or 3 Tracks	In 10° cone	84.5 ± 0.7
Total		64 ± 1

Table 3.5: The taujet identification requirements and efficiencies from simulated leptoquark events ($M_{LQ} = 125$ GeV/c^2). These requirements are made on central jets with $E_t > 15$ GeV and $|\eta_d| < 1$. The variable η_d is the pseudorapidity calculated assuming $z = 0$. The leptoquark events were generated with the ISAJET Monte Carlo and passed through a simulation of the CDF detector. The events used in calculating the efficiencies were required to have a central lepton (e or μ) with $E_t > 20$ GeV. The central jet was required to have a generated tau pointing to it.

3.5.2 Taujet Fiducial Region

The taujets are restricted to a fiducial region of the central detector detector which is away from uninstrumented regions of the calorimeter. This is accomplished by extrapolating the leading track to the central strip chambers in the CEM. The extrapolated position in the ϕ view must be within 21 cm of the tower center. The track position in the z direction must also be more than 9 cm away from the $z = 0$. These requirements remove taujets in which the most energetic track passes through a boundary between calorimeter modules. Roughly (83±1)% of the taujets in simulated leptoquark events enter the fiducial region.

3.5.3 Taujet Identification Requirements

Hadronic taus are identified by placing requirements on the p_t of tracks in the 10° cone: $p_t^{lead} > 10$ GeV/c for all taujets, and $\sum p_t > 20$ GeV for jets with $N_{10°} \geq 3$. Also, electron candidates are removed using the expected relation between the ratio E_t/p_t^{lead} and the jet electromagnetic fraction. The taujet identification criteria are listed in Table 3.5.

To estimate the efficiencies of these requirements for selecting hadronic taus, a sample of jets from simulated leptoquark events was chosen. The sample was generated using the ISAJET event generator (see Chapter 6) and was put through a simulation of the detector. Events with a central lepton $p_t > 20$ GeV were required to have a generated tau associated with a central jet with $E_t > 15$ GeV and $|\eta_d| < 1.0$. These jets are used in the simulation distributions in Figures 3.8-3.9. The efficiency of each identification criteria is listed in Table 3.5. The efficiencies are $\varepsilon = N(pass\ single)/N_{tot}$, where N_{tot} is the total number of jets with $E_t > 15$ GeV and $|\eta_d| < 1.0$, and $N(pass\ single)$ is the number of jets satisfying the given criteria.

To estimate the fraction of quark and gluon jets which satisfy the identification criteria, a control sample of jets is assembled from the data. The inclusive lepton samples from which the $Z \rightarrow ee$ and $Z \rightarrow \mu\mu$ samples were selected are appropriate samples to start with. The control sample events are required to contain at least one lepton satisfying either of the following requirements:

Lepton Selection For Control Sample	
Electron Selection	Muon Selection
$E_t > 20$ GeV	$p_t > 20$ GeV/c
Pass e ID (Table 3.1)	Pass μ ID (Table 3.3)
$\lvert z_v^{ele}\rvert < 60$ cm	$\lvert z_v^{\mu}\rvert < 60$ cm
Fiducial	
Conversions Removed (Section 4.2)	

The events are further required to contain a jet $E_t > 15$ GeV with $|\eta_d| < 1.0$. Finally, only events having $Q_\ell \times Q_{\tau jet} \geq 0$ are considered, where Q_ℓ is the lepton charge, and $Q_{\tau jet}$ is the jet charge defined above. The condition $Q_{\tau jet} = 0$ implies that there is no candidate track in the 10° associated with the jet. The jets in these lepton + jets events are used in the distributions in Figures 3.10-3.11.

Most of the taujet identification criteria are correlated with jet E_t. A fair comparison between the efficiencies for hadronic taus and the efficiencies for quark or gluon jets is the dependence on jet E_t in each case. These are shown in Figures 3.12-3.14. The distributions which separate hadronic taus from jets are the track p_t, track mass $M(trks)$, and the number of tracks requirements. These quantities are clearly correlated. The total efficiency at $E_t = 20$ GeV is 45% for taus and 3% for control sample jets. The efficiency for taus plateaus at a value of 70% at $E_t = 40$ GeV. For control sample jets the plateau efficiency is around 8% also at $E_t = 40$ GeV.

3.6 Neutrino Reconstruction

Neutrinos do not interact in the detector, so their presence must be inferred by an imbalance of transverse energy, or "missing E_t" ($\not\!\!E_t$) in the event. The missing E_t magnitude and direction are given by the negative vector sum of the transverse energy in the calorimeter.

$$\vec{\not\!\!E}_t = -\sum E_t^i \cdot \hat{n}_i, \quad \text{i = calorimeter tower } |\eta_d| < 3.5 \tag{3.6}$$

where $\hat{n}_i$ is a unit vector pointing to the i^{th} tower. There are detector-dependent thresholds on the tower energy in order to enter the sum: 100 MeV for the CEM, CHA and WHA, 300 MeV for the PEM, 500 MeV for the PHA and FEM, and 800 MeV for the FHA. The longitudinal momentum of the colliding partons is not known. So only the transverse component of the neutrino momentum can be calculated in general.

Two corrections may be applied to the calorimeter sum in Equation 3.6. The

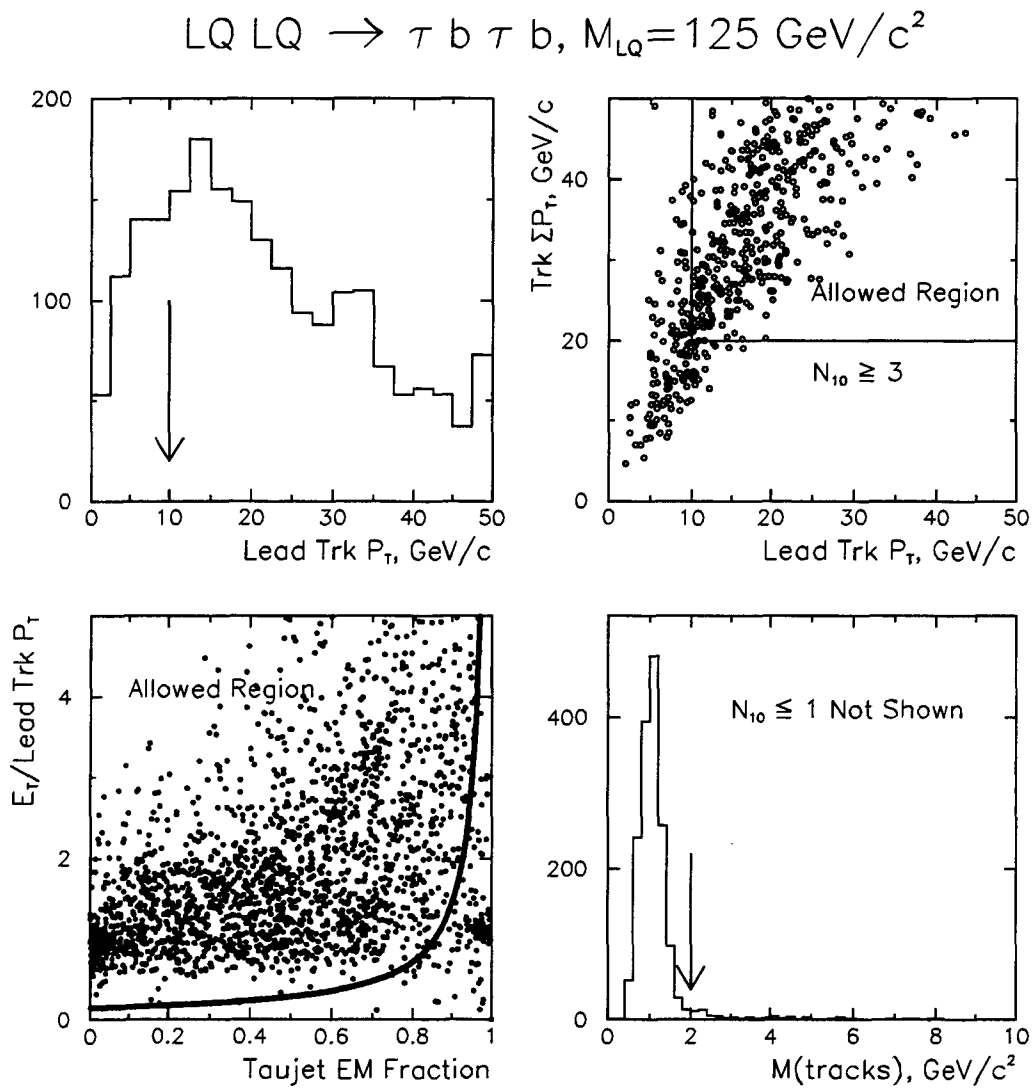

Figure 3.8: The distributions of the taujet identification variables for taus in simulated leptoquark events (ISAJET $M_{LQ} = 125$ GeV/c^2). Each jet is central, $|\eta_d| < 1$, with $E_t > 15$ GeV, and has a generated tau pointing to it. In addition the events must have a central lepton $p_t > 20$ GeV/c. The top two plots show the p_t requirements for taujets. The top left plot shows the distribution of p_t^{lead}, the p_t of the leading track in the 10° cone centered on jet axis. The arrow indicates the requirement for taujet identification. The top right plot shows the scatter plot of Σp_t, the sum p_t of 10° tracks, and p_t^{lead} for jets with three or more track in the 10° cone. The bottom left shows the scatter plot of the jet electromagnetic fraction and the ratio E_t/p_t^{lead}. The jets which enter below the curved line are tagged as electrons and removed. The cluster of jets at $E_t/p_t^{lead} = 1$ and EM fraction > 0.9 are electrons from $\tau \to e\nu\nu$ decays. The bottom right plot shows the mass formed by the tracks in the 10° cone for jets with $N_{10°} > 1$. The arrow indicates the requirement for taujet identification.

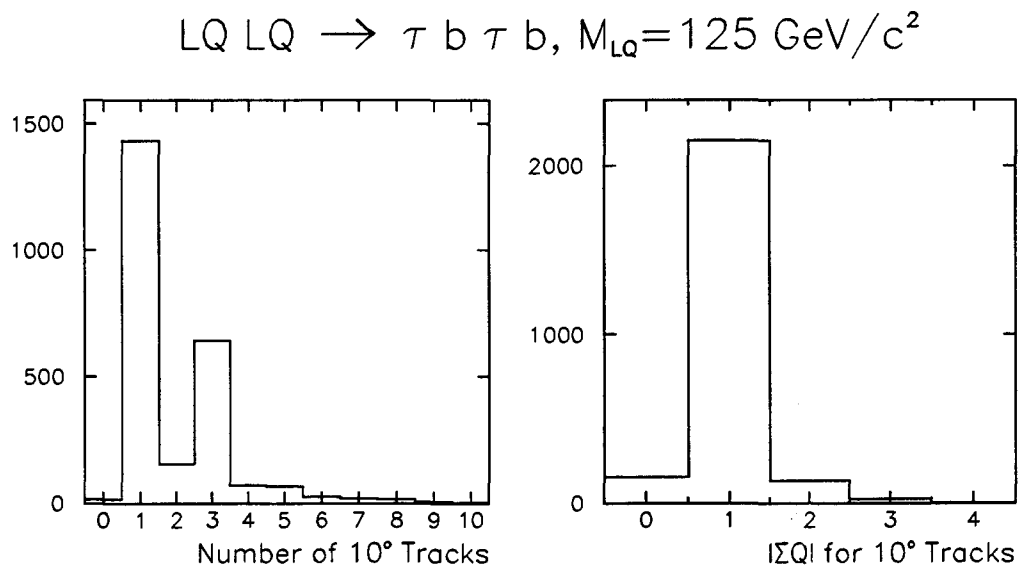

Figure 3.9: The distributions of the taujet variables for taus in simulated leptoquark events (ISAJET $M_{LQ} = 125$ GeV/c^2). Each jet is central, $|\eta_d| < 1$, with $E_t > 15$ GeV, and has a generated tau pointing to it. In addition the events must have a central lepton $p_t > 20$ GeV/c. The left plot shows the distribution of $N_{10°}$, the number of tracks in the 10° cone centered on the jet axis. Hadronic taus are required to have $N_{10°} = 1$ or 3. The hadronic tau jets with $N_{10°} = 2$ or $N_{10°} \geq 4$ in the plot above overlap with other activity in the event (eg. jets or random tracks from underlying event). The right plot shows the distribution of $\sum_{10°} Q$, the sum of the charges of the tracks in the 10° cone. This is not a taujet identification variable, but is used in defining the taujet charge (Equation 3.5).

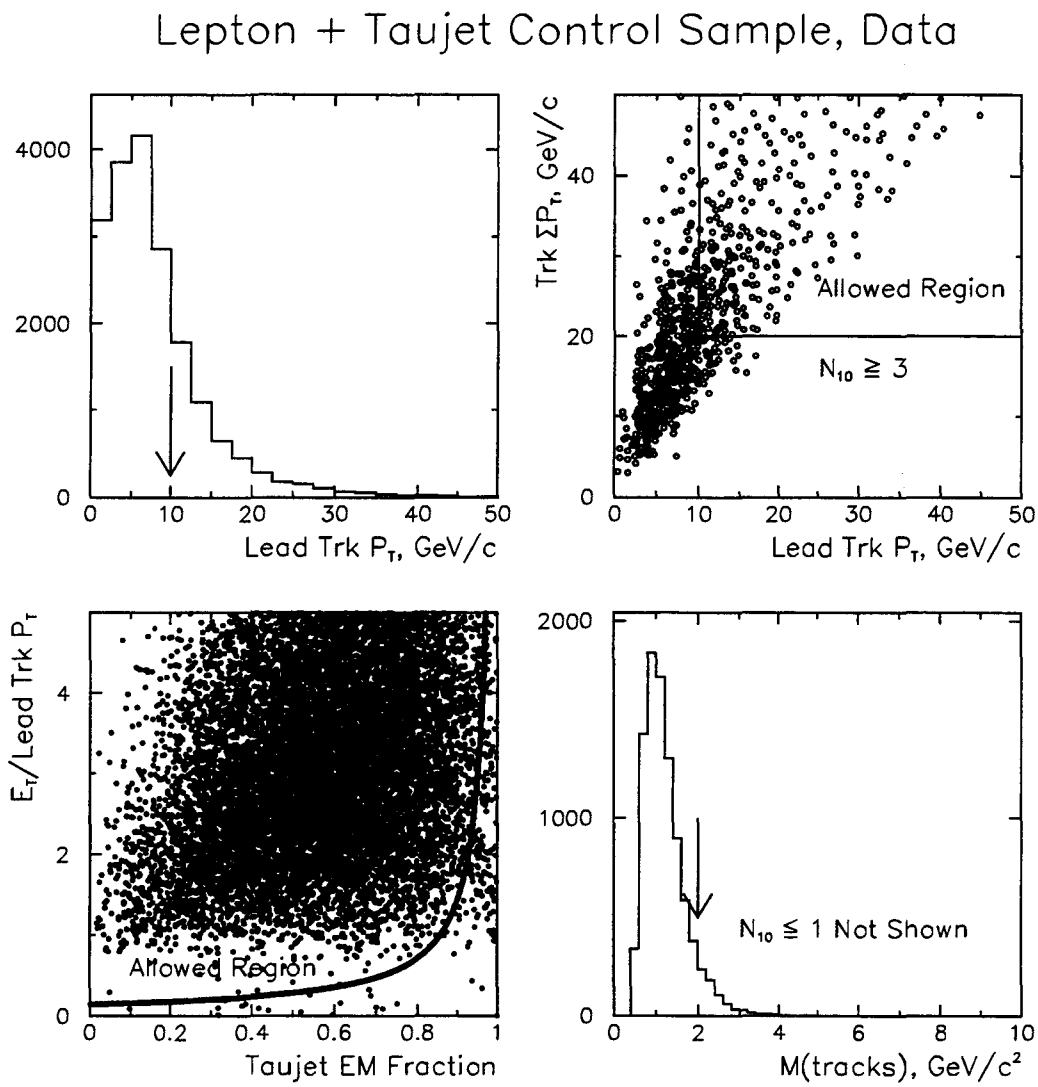

Figure 3.10: The distributions of the taujet identification variables for jets in a lepton + jet control sample (data), defined in the text. The jets are central, $|\eta_d| < 1$, with $E_t > 15$ GeV. The control sample is defined by $Q_\ell \times Q_{jet} \geq 0$, where is given by $Q_{jet} = Q_{\tau jet}$. The jets in this sample are expected to be from quarks and gluons. The top two plots show the p_t requirements for taujets. The top left plot shows the distribution of p_t^{lead}, the p_t of the leading track in the 10° cone centered on jet axis. The arrow indicates the requirement for taujet identification. The top right plot shows the scatter plot of Σp_t, the sum p_t of 10° tracks, and p_t^{lead} for jets with three or more track in the 10° cone. The bottom left shows the scatter plot of the jet electromagnetic fraction and the ratio E_t/p_t^{lead}. The jets which enter below the curved line are tagged as electrons and removed. The bottom right plot shows the mass formed by the tracks in the 10° cone for jets with $N_{10°} > 1$. The arrow indicates the requirement for taujet identification.

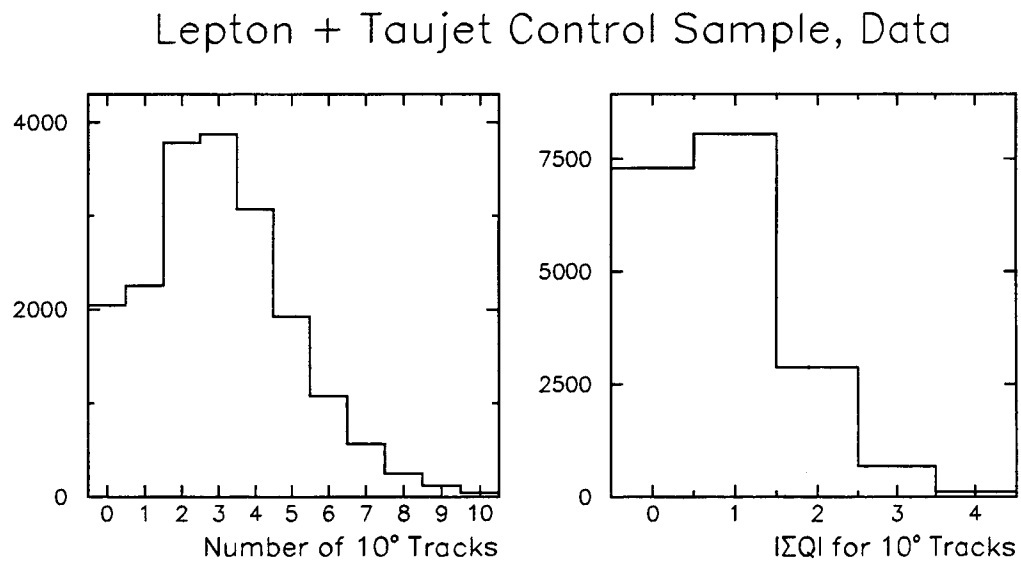

Figure 3.11: The distributions of the taujet identification variables for jets in a lepton + jets control sample (data), defined in the text. The jets are central, $|\eta_d| < 1$, with $E_t > 15$ GeV. The control sample is defined by $Q_\ell \times Q_{jet} \geq 0$, where is given by $Q_{jet} = Q_{\tau jet}$. The jets in this sample are expected to be from quarks and gluons. The left plot shows the distribution of N_{10°, the number of tracks in the 10° cone centered on the jet axis. The taujet identification requirement is $N_{10^\circ} = 1$ or 3. Clearly this rejects a significant fraction of jets from quarks and gluons. The right plot shows the distribution of $\sum_{10^\circ} Q$, the sum of the charges of the tracks in the 10° cone. This is not a taujet identification variable, but is used in defining the jet charge (Equation 3.5). The jet charge is defined to be $\sum_{10^\circ} Q$ unless $\sum_{10^\circ} Q \neq \pm 1$. If $\sum_{10^\circ} Q \neq \pm 1$ then the jet charge is defined to be the charge of the leading track in the 10° cone.

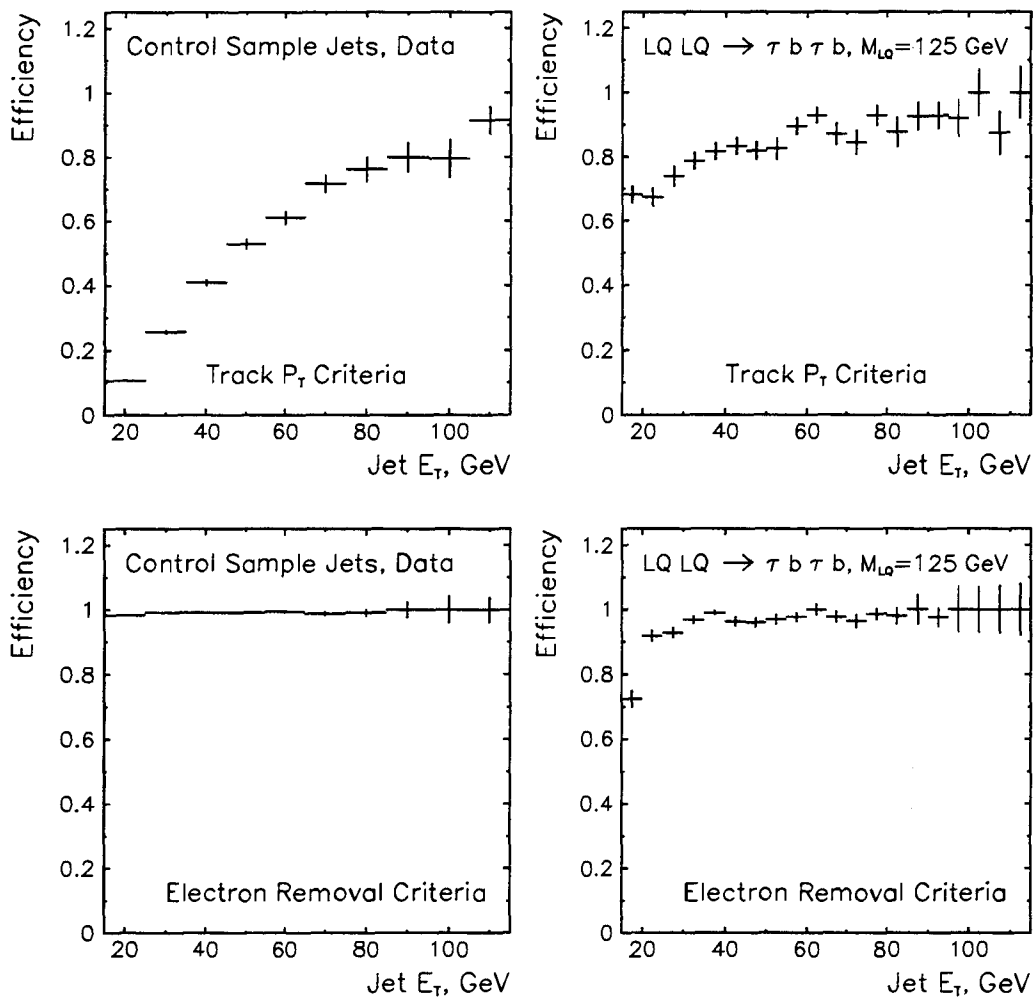

Figure 3.12: The efficiencies of the tau identification criteria versus jet E_t for control sample jets (data, defined in text) and for jets from hadronic tau decays in simulated leptoquark events (ISAJET, $M_{LQ} = 125$ GeV/c^2). Each jet is central, $|\eta_d| < 1$, with $E_t > 15$ GeV. The taujet identification requirements are applied to these jets. The left plots show the fraction of jets from the control sample which satisfy the requirement indicated. The right plots show the fraction of taus in simulated leptoquark events which satisfy the requirement indicated. The track p_t criteria for taujet identification are $p_t^{lead} > 10$ GeV/c for all jets and $\Sigma p_t > 20$ GeV/c for jets with $N_{10^\circ} \geq 3$. The electron removal requirement is EMF $< 1 - \frac{p_t}{7E_t}$. Otherwise the jet is rejected.

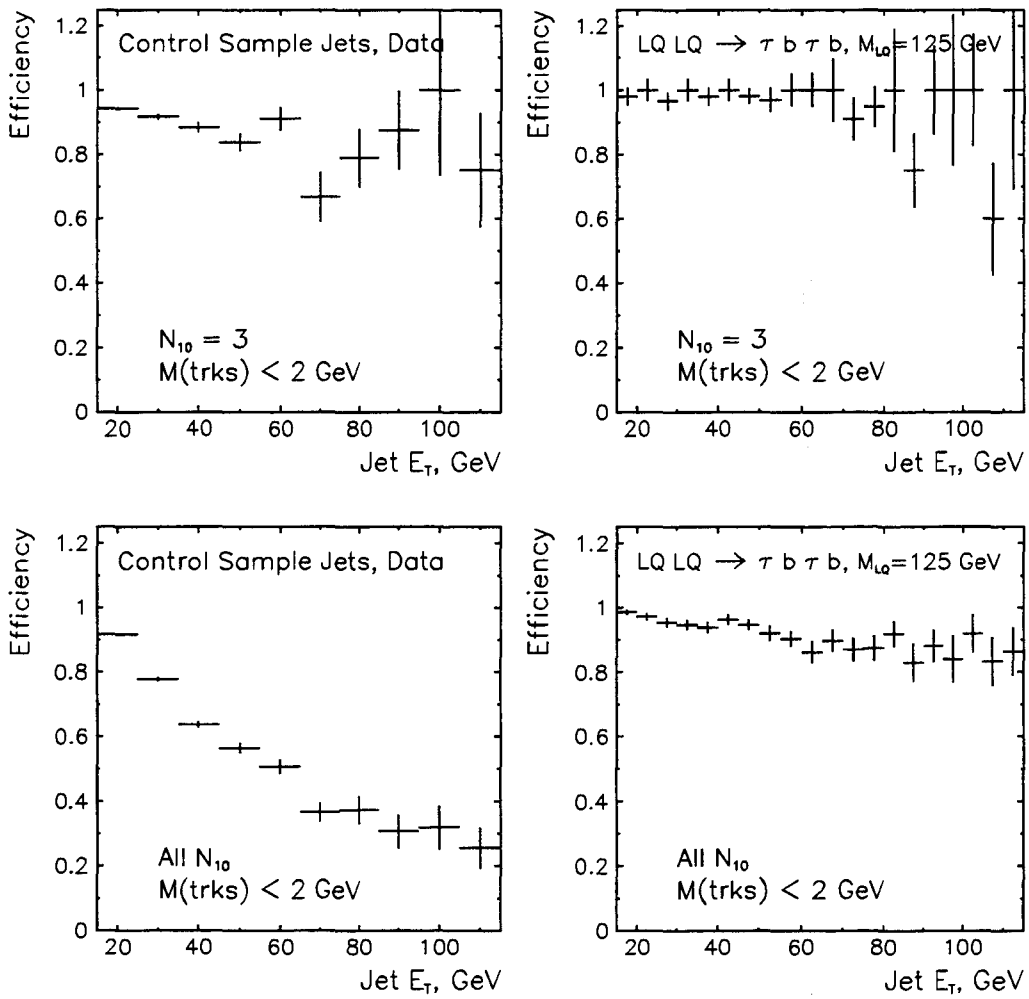

Figure 3.13: The efficiencies of the tau identification criteria versus jet E_t for control sample jets (data, defined in text) and for jets from hadronic tau decays in simulated leptoquark events (ISAJET, $M_{LQ} = 125$ GeV/c^2). Each jet is central, $|\eta_d| < 1$, with $E_t > 15$ GeV. The taujet identification requirements are applied to these jets. The left plots show the fraction of jets from the control sample which satisfy the requirement indicated. The right plots show the fraction of taus in simulated leptoquark events which satisfy the requirement indicated. The top plots show the efficiency of the tracks' mass requirement, $M(trks) < 2$ GeV/c^2, only for jets with $N_{10^\circ} = 3$. The bottom plots show the efficiency of the $M(trks)$ requirement for all jets.

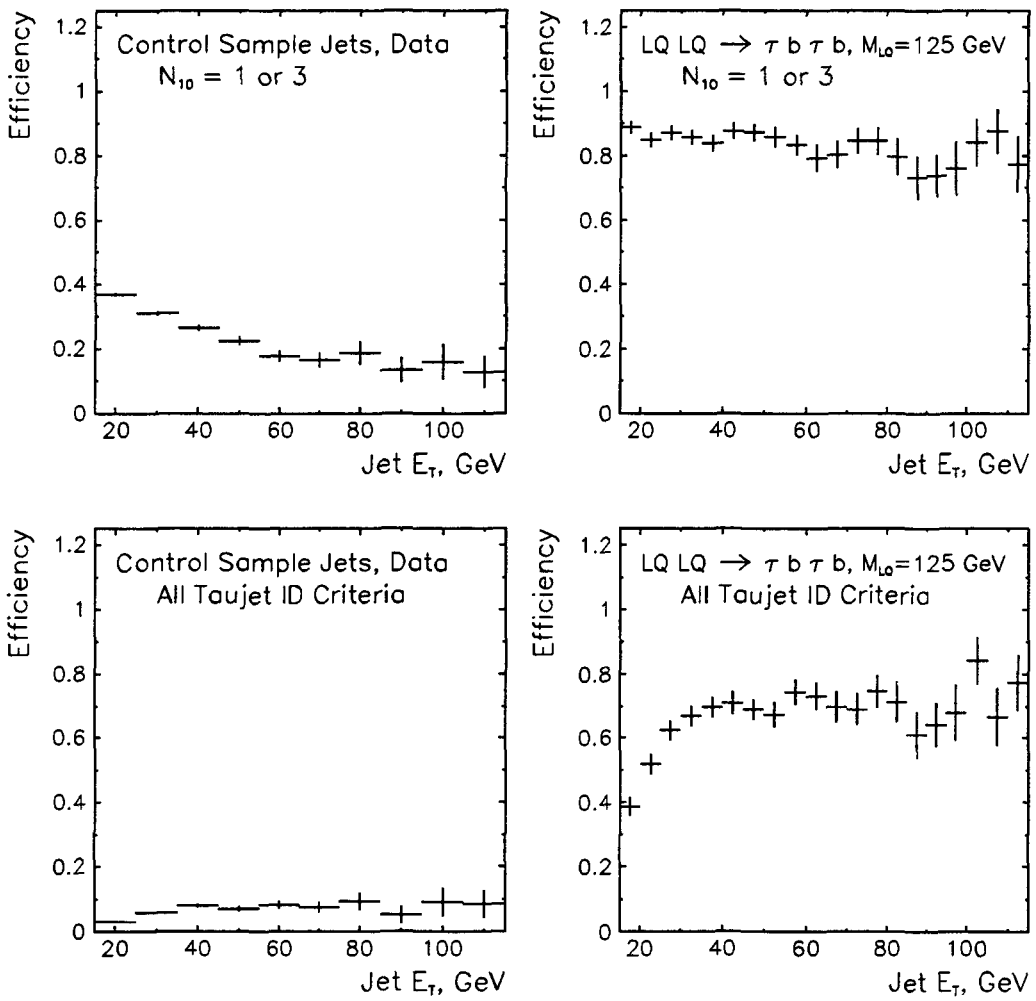

Figure 3.14: The efficiencies of the tau identification criteria versus jet E_t for control sample jets (data, defined in text) and for jets from hadronic tau decays in simulated leptoquark events (ISAJET, $M_{LQ} = 125$ GeV/c^2). Each jet is central, $|\eta_d| < 1$, with $E_t > 15$ GeV. The taujet identification requirements are applied to these jets. The left plots show the fraction of jets from the control sample which satisfy the requirement indicated. The right plots show the fraction of taus in simulated leptoquark events which satisfy the requirement indicated. The top plots show the efficiency of the taujet identification requirement, $N_{10^\circ} = 1$ or 3. The bottom plots show the total efficiency of all taujet identification requirements listed in Table 3.5.

corrected $\vec{\not\!\!E}_t$ is given by

$$\vec{\not\!\!E}_t^{\,cor} = \vec{\not\!\!E}_t + \vec{\not\!\!E}_t^{\,e\,cor} + \vec{\not\!\!E}_t^{\,\mu\,cor} \tag{3.7}$$

where $\vec{\not\!\!E}_t^{\,e\,cor}$ and $\vec{\not\!\!E}_t^{\,\mu\,cor}$ are the corrections for electrons and muons respectively. Energy corrections were made to high-E_t electrons, but the uncorrected electron towers are used in the $\not\!\!E_t$ calculation. Equation 3.8 gives the contribution to take this into account.

$$\vec{\not\!\!E}_t^{\,e\,cor} = \sum_{ele} \left\{ \vec{E}_t^{\,ele}(\text{uncor}) - \vec{E}_t^{\,ele}(\text{cor}) \right\} \tag{3.8}$$

The sum is over central fiducial electrons with $E_t^{cor} > 18$ GeV passing the strict identification criteria in Table 3.1.

The second correction takes into account the presence of high-p_t muons. Since muons deposit minimum ionizing energy in the calorimeter, Equation 3.6 does not include the full muon energy. Equation 3.9 corrects for this by removing the E_t deposited in the EM and hadronic calorimeter towers traversed by the muon, and adding in the beam-constrained muon p_t.

$$\vec{\not\!\!E}_t^{\,\mu\,cor} = \sum_{\mu} \left\{ \vec{E}_t(\mu \text{ towers}) - \vec{p}_t^{\,\mu} \right\} \tag{3.9}$$

For this correction, the sum is over all muons with beam-constrained $p_t > 10$ GeV which are minimum ionizing in the calorimeter: $E_{EM} < 2.0$ GeV and $E_{Had} < 6.0$ GeV in the towers traversed by the muon. No other requirements are made on the muon.

The resolution of the $\not\!\!E_t$ measurement is dependent on the event topology. This is because the $\not\!\!E_t$ depends on the resolutions of the measurements of the electrons, muons, and jets. The uncertainty in $\not\!\!E_t$ is affected most by the errors in the measurements of jet energies since the electrons and muons are typically well-measured. The resolution in $\not\!\!E_t$, $\sigma(\not\!\!E_t)$, is parametrized as a function of the total transverse momentum in the event, ΣE_t. The $\not\!\!E_t$ resolution is measured in minimum events which

require only a coincidence of hits in both the forward and backward BBC's (see Section 2.6). These events are dominated by inelastic $p\bar{p}$ events with no significant $\not\!\!E_t$ expected. A fit to the minimum bias data yields [68]

$$\sigma(\not\!\!E_t) = -0.582 + 0.7418\sqrt{\Sigma E_t}, \quad \text{in GeV} \tag{3.10}$$

For a typical W event, $\sigma(\not\!\!E_t) \sim 3$ GeV while the neutrino momentum is of order 10–40 GeV. The measurement of the $\vec{\not\!\!E}_t$ direction, $\phi(\not\!\!E_t)$, depends on $\sigma(\not\!\!E_t)$ and $\not\!\!E_t$. For small values of $\not\!\!E_t$, the direction of $\vec{\not\!\!E}_t$ is less well-defined because fluctuations from calorimeter energy resolution smear $\phi(\not\!\!E_t)$. In events with large $\not\!\!E_t$, from neutrinos for example, $\phi(\not\!\!E_t)$ is less subject to these fluctuations.

The resolution of $\phi(\not\!\!E_t)$ is estimated from the simulated leptoquark events from Chapter 6. These events contain neutrinos from tau decays for example. The total momentum carried by neutrinos in the event is calculated from the generator-level quantities. This gives the expected $\not\!\!E_t$ before detector simulation. This is compared to the reconstructed $\not\!\!E_t$ after a full detector simulation. For reconstructed $\not\!\!E_t < 25$ GeV, the reconstructed $\phi(\not\!\!E_t)$ is within $\sim \pm 60°$ of the total neutrino momentum direction. For reconstructed $\not\!\!E_t > 25$ GeV, the reconstructed $\phi(\not\!\!E_t)$ matches the total neutrino momentum direction to better than $\pm 20°$.

Chapter 4

Leptoquark Search

4.1 Data Sets

The starting point for the leptoquark analysis are inclusive high-p_t electron and muon samples formed offline. These samples are selected from a subset of Level 3 triggers composed of events with high-p_t leptons

The inclusive lepton samples were made by selecting muons with unconstrained $p_t > 18$ GeV or electrons with uncorrected $E_t > 18$ GeV passing identification criteria looser than those listed in Tables 3.1 and 3.3. No isolation or fiducial cuts were made. These inclusive samples consist of $\sim 450,000$ central electrons and $\sim 480,000$ central muons total. The integrated luminosities of the electron and muon data sets are listed in Table 4.1. These represent an exposure of $\sim 72\ pb^{-1}$.

4.2 Lepton + Taujet Selection

From the inclusive lepton samples above, events with at least one central muon, $p_t > 20$ GeV/c, or at least one central electron, $E_t > 20$ GeV are selected. The leptons must satisfy the identification criteria in Tables 3.1 and 3.3. The beam position is incorporated into the measurement of the muon p_t (a beam-constraint). The central

	Muons	Electrons
Run 1A	$\int \mathcal{L}dt = 18.6\ pb^{-1}$ CMU, CMUP	$\int \mathcal{L}dt = 19.7\ pb^{-1}$
Run 1B	$\int \mathcal{L}dt = 52.7\ pb^{-1}$ CMU, CMUP, CMX	$\int \mathcal{L}dt = 52.8\ pb^{-1}$

Table 4.1: The integrated luminosities of the inclusive lepton samples used in the leptoquark search. This represents the Run 1A and Run 1B data recorded by CDF from August, 1992 through February, 1995. Runs with detector problems are not included in the sums.

muon types accepted are CMU-only, CMUP, and CMX (Section 3.4.2). The electron E_t is corrected for the effects described in section 3.3.4. The electron must be in the fiducial region defined in Section 3.3.3. The z-vertex associated with each lepton must also be within 60 cm of the nominal interaction point, $z = 0$. Muons passing through the CMX drift chambers are required to exit the Central Tracking Chamber (CTC) through the outermost superlayer. This restricts the CMX muon to regions of the CTC with full coverage by the Central Fast Tracker (CFT) trigger.

A final requirement is made on the electron sample. Neutral pions are produced copiously in $p\bar{p}$ collisions. Photons from π° decays may pass through detector material and convert into an e^+e^- pair, producing a high E_t electron with a low energy partner. The Dalitz decays of pions can also produce this final state. Electrons from these sources are identified [102] by searching for an opposite charged partner electron forming a small opening angle and low mass with the primary electron, and both extrapolating from a common point. The efficiency of the algorithm is $(84 \pm 3)\%$ for removing conversion electrons, but it also removes $(1.1 \pm 0.3)\%$ of prompt electrons determined from $Z \rightarrow ee$ and $W \rightarrow e\nu$ events [103].

Runs identified as having trigger problems or problems with the calorimeter or muon systems are removed from the analysis. Runs in high-E_t electron samples which have problems with the muon detector systems are not removed, and vice versa for

the high-p_t muon samples.

The events satisfying the above lepton selection must also have at least one jet with $E_t > 15$ GeV and $|\eta_d| < 1$. The jet must also satisfy the taujet identification criteria and be contained in the fiducial region. The taujet identification and fiducial requirements are described in Sections 3.5.2 and 3.5.3.

The electron (muon) plus taujet events are then required to have triggered a Level 2 electron (muon) trigger. The triggers used in this analysis were described in Section 2.6.

4.3 Isolation Requirements

To select leptons and taujets from tau decays, isolation requirements are made on the electron, muon and taujet. Muon and electrons must satisfy the calorimeter isolation requirement

$$I_{cal} < 0.1 \tag{4.1}$$

I_{cal} is defined in Equations 3.2 and 3.4.

Figure 4.1 shows the lepton isolation distributions for events satisfying the selection requirements in the previous section. The data are split into two sub-samples. A same-sign sample (SS) is composed of events in which the lepton and taujet have like-sign charges, $Q_\ell \times Q_{\tau jet} = +1$. The opposite-sign sample (OS), is defined by $Q_\ell \times Q_{\tau jet} = -1$. The I_{cal} distributions for the OS and SS lepton plus taujet data are shown in Figures 4.1a and b. There are 995 OS events and 621 SS events. After the $I_{cal} < 0.1$ requirement is imposed, 501 OS and 241 SS events remain. For comparison, Figure 4.1c shows the I_{cal} distribution for leptons in simulated leptoquark events, discussed in Chapter 6. This requirement is 81% efficient for leptons in leptoquark events with $M_{LQ} = 50$ GeV/c^2. Figure 4.1d shows the I_{cal} distribution for simulated $Z \rightarrow \tau\tau$ events, described in Chapter 5. These events produce opposite-sign lepton + taujet pairs, so they contribute to the number of OS events in Figure 4.1a. In

72 pb^{-1}, 99 $Z \rightarrow \tau\tau$ events are expected to satisfy the lepton + taujet selection requirements of the previous section. Of these, 98% are expected to pass the lepton isolation requirement.

Taus from $W^{\pm}$, Z° and leptoquarks decays are expected to be well-separated from other activity in the event. This is seen for simulated leptoquark and $Z \rightarrow \tau\tau$ events in the I_{cal} distributions for leptonically decaying taus (Figure 4.1c-d). Hadronically decaying taus are similarly isolated. The taujet isolation variable, N_{isol}, is the track multiplicity in the region surrounding the taujet (Section 3.5.1). Isolated taujets are selected by requiring that there be no tracks in the isolation region:

$$N_{isol} = 0 \tag{4.2}$$

Figures 4.2a-b show the taujet isolation distributions in the data for events satisfying the lepton isolation criteria. The taujet N_{isol} distribution for simulated leptoquark events is shown in Figure 4.2c. Approximately 65% of the taujets in leptoquark events are isolated. The OS and SS data are shown separately in Figure 4.2a-b. The distributions in the OS and SS data are different in shape, with the OS lepton + taujet data containing a larger fraction of isolated taujets than the SS data. This suggests that hadronic taus are already present in the OS sample. Figure 4.2d shows the N_{isol} distribution for simulated $Z \rightarrow \tau\tau$ events. In 72 pb^{-1}, 97 $Z \rightarrow \tau\tau$ events are expected to satisfy the lepton isolation requirement. Of these, 87% are expected to pass the taujet isolation requirement. After the taujet isolation requirement is applied, 212 OS events and 69 SS events remain in the data.

4.4 $Z \rightarrow ee$ and $Z \rightarrow \mu\mu$ Removal

The electron and muon criteria above are efficient for selecting $Z \rightarrow ee$ or $Z \rightarrow \mu\mu$ events. With the additional requirement of a taujet, $Z \rightarrow ee/\mu\mu$ events can enter the analysis in two ways: 1) the event is a $Z+ \geq 1$ jet event where a jet satisfies the taujet

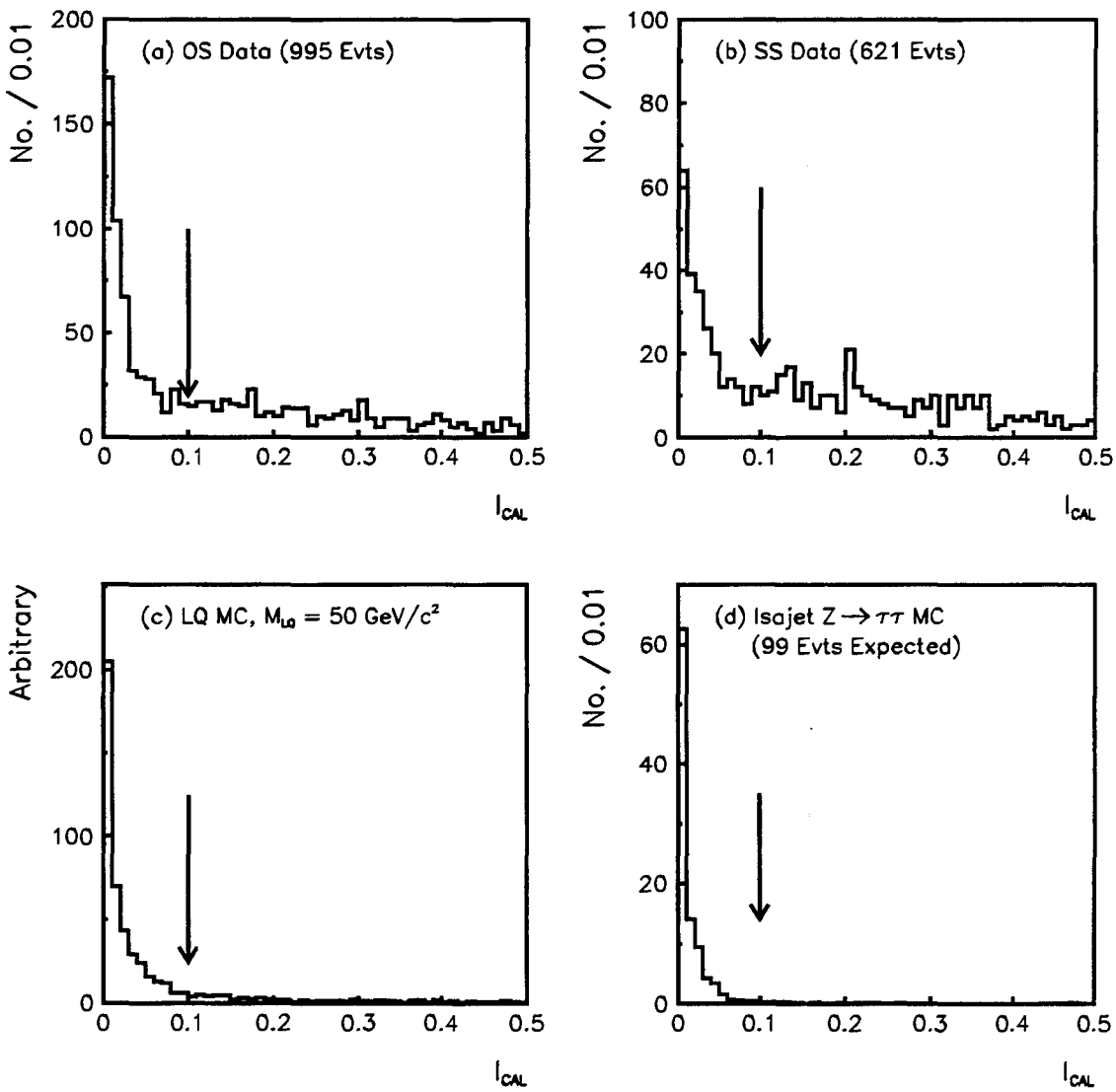

Figure 4.1: The lepton isolation distributions after the lepton + taujet selection, for (a) opposite-sign and (b) same-sign lepton + taujet events in the data; plot (c) shows the I_{cal} distribution for leptons in simulated leptoquark events; and plot (d) shows the I_{cal} distribution for leptons in simulated $Z \rightarrow \tau\tau$ events. The simulated events are generated using the ISAJET Monte Carlo program and passed through a simulation of the CDF detector. The leptoquarks are scalar with $M_{LQ} = 50$ GeV/c^2. The arrows indicate the lepton isolation requirement $I_{cal} < 0.1$.

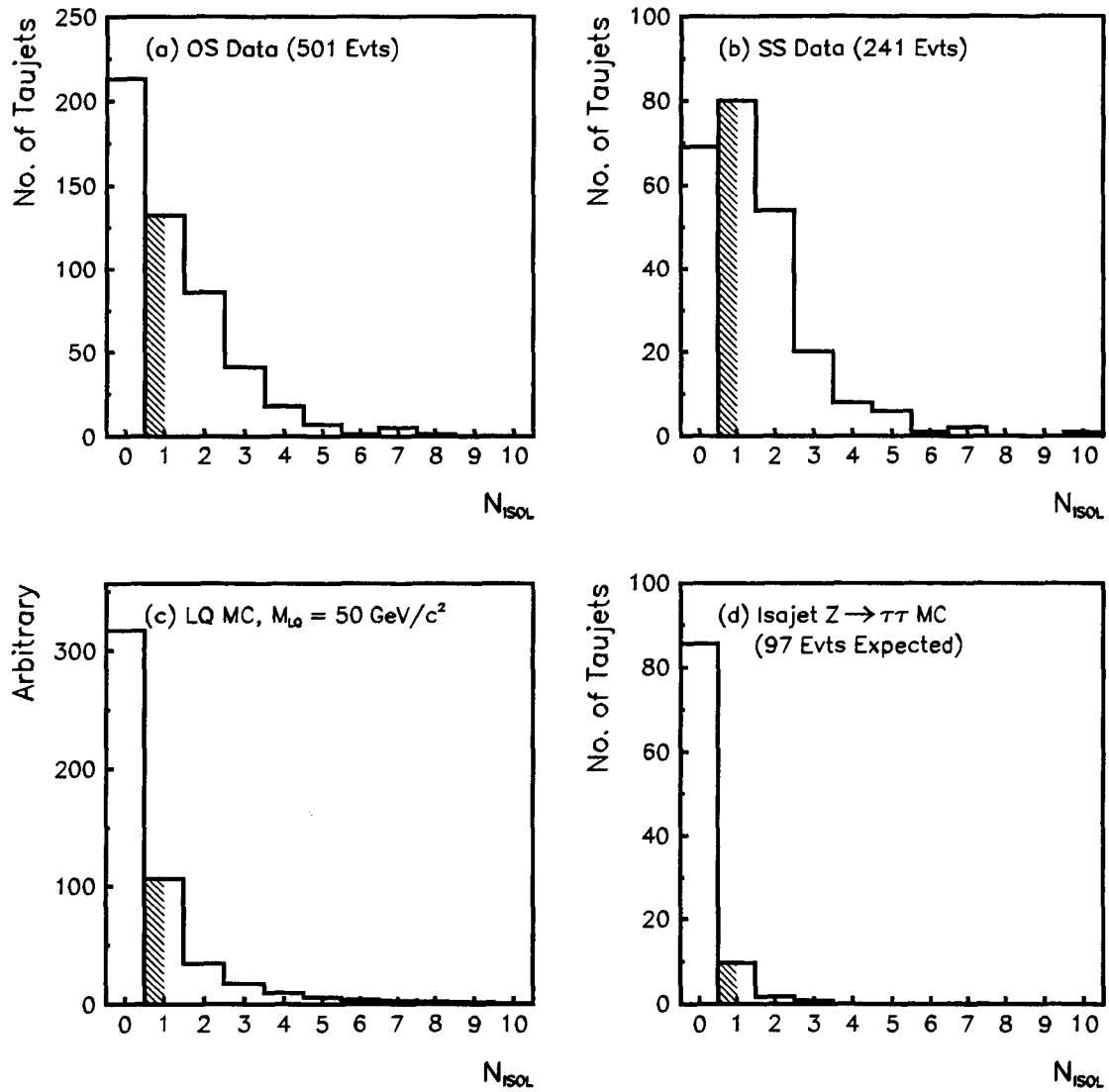

Figure 4.2: N_{isol}, the track multiplicity in the taujet isolation region, defined as the area between the 10° and 30° cones centered on the jet axis, for (a) opposite-sign and (b) same-sign lepton + taujet events in the data; (c) for the for taujets in simulated leptoquark events; and (d) for taujets in simulated $Z \rightarrow \tau\tau$ events . All events pass the lepton isolation requirement. The simulated events are generated using the ISAJET Monte Carlo program and passed through a simulation of the CDF detector. The leptoquarks are scalar with $M_{LQ} = 50$ GeV/c^2. The hatched boundaries shows the isolation requirement $N_{isol} = 0$. Taujets with $N_{isol} \geq 1$ are rejected.

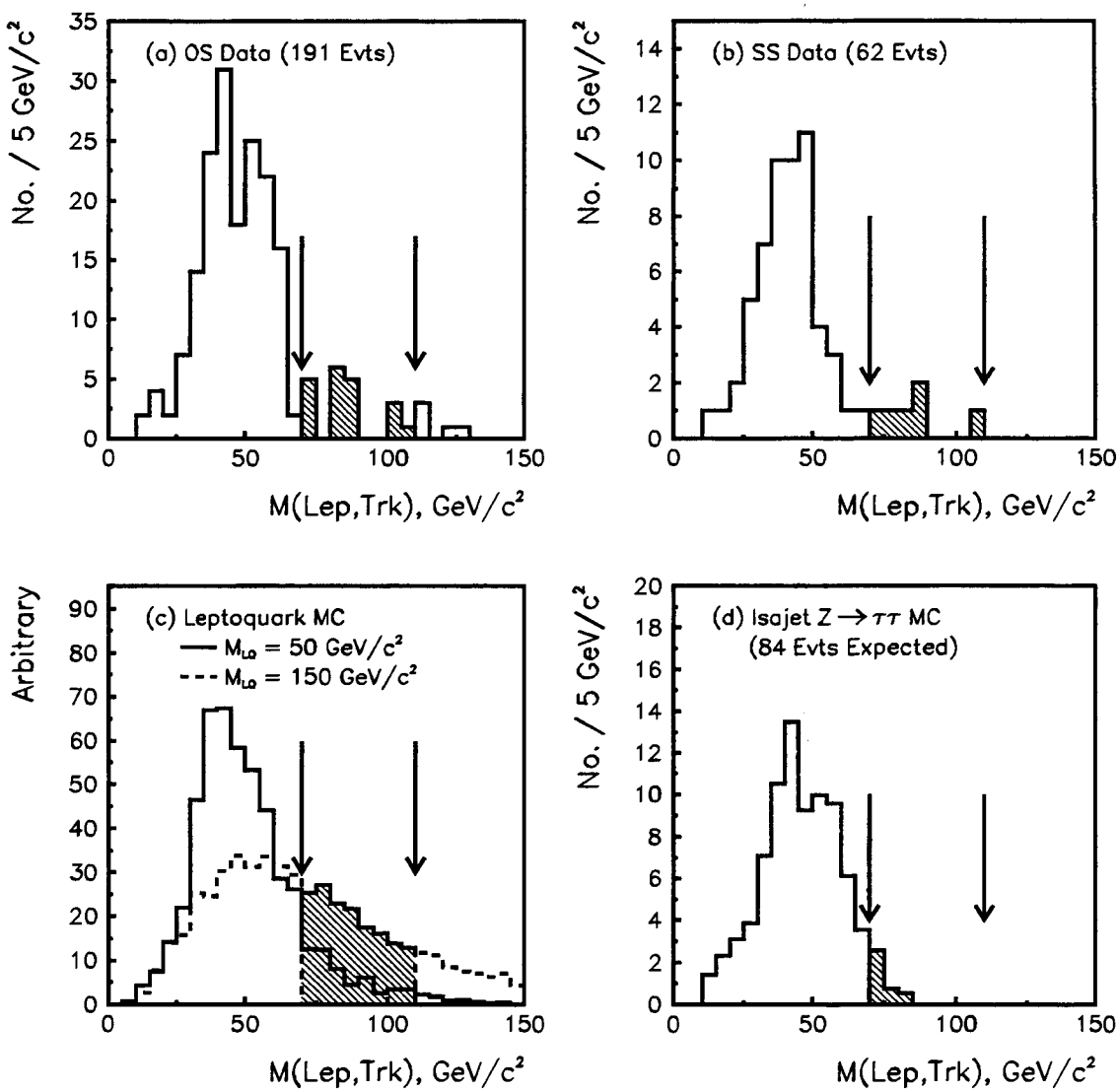

Figure 4.3: $M(\ell, trk)$, the mass of lepton and leading taujet track, for (a) opposite-sign and (b) same-sign lepton + taujet events in the data; for (c) simulated leptoquark events; and for (d) simulated $Z \rightarrow \tau\tau$ events. All events pass the $M_{\mu\mu}$ Z removal. The simulated events are generated using the ISAJET Monte Carlo program and passed through a simulation of the CDF detector. The leptoquarks are scalar with $M_{LQ} =$ 50 GeV/c^2. The events having $M(\ell, trk)$ in the hatched region are rejected by the Z removal veto: 70 GeV/c^2 < $M(\ell, trk)$ < 110 GeV/c^2

selection, or 2) only one of the Z decay leptons passes the strict identification criteria, and the other lepton forms a taujet in the calorimeter. The first case is straightforward to identify. To be efficient, a looser set of electron and muon identification criteria is used to search for a second lepton with $E_t > 10$ GeV. The event is rejected if the dilepton mass, $M_{\ell\ell}$, falls in a window about the Z mass:

$$\text{Reject event if:} \qquad 70 \text{ GeV}/c^2 < M_{\ell\ell} < 110 \text{ GeV}/c^2 \tag{4.3}$$

There are 21 OS events and 7 SS events removed the $M_{\ell\ell}$ requirement. This retains 97% of the events from simulated leptoquark events with $M_{LQ} = 50$ GeV/c^2, and 98% of the events from $Z \rightarrow \tau\tau$ simulation.

The second case is more troublesome: the second electron or muon from the Z decay forms a untypical calorimeter signature. For electrons and muons alike, there is a small but finite probability that the lepton showers in the calorimeter to produce a taujet. Furthermore, such a taujet is likely to be isolated since it is from a Z decay. Electron showers are generally contained in the EM calorimeter, with only a small fraction of the energy deposited in the hadronic compartment (see for example the HAD/EM distribution in Figures 3.1 and 3.2). However, if there is sufficient leakage into the hadron calorimeter, the shower will not be clustered as an electron (recall there is an intrinsic maximum leakage in the electron clustering algorithm). Muons are typically minimum ionizing in the calorimeter. However, the distribution of deposited energy (a Landau distribution) has a tail which extends to large energies. Thus a muon may occasionally deposit a significant amount of energy in the calorimeter which is then clustered as a jet. Rather than estimate the background from these processes, events which are consistent such sources are removed from the data.

This background is removed as follows. The most serious source of these events is expected to be $Z \rightarrow ee$ or $\mu\mu$. The charged track of the unidentified lepton can be used to identify the events in which this lepton forms a taujet. This is accomplished by calculating $M(\ell, trk)$, the mass of the primary lepton and the leading track of the

taujet, which presumably is the second lepton in $Z \rightarrow \ell\ell$. The event is removed as a $Z \rightarrow ee$ or $\mu\mu$ candidate if the lepton-track mass, $M(\ell, trk)$, falls in a window about the Z mass:

$$\text{Reject event if:} \qquad 70 \text{ GeV}/c^2 < M(\ell, trk) < 110 \text{ GeV}/c^2 \tag{4.4}$$

The distribution of $M(\ell, trk)$ for events surviving the $M_{\ell\ell}$ requirement can be found in Figure 4.3. There are 20 OS events and 6 SS events removed the $M(\ell, trk)$ veto. The veto rejects 11% of simulated leptoquark events ($M_{LQ} = 50$ GeV/c^2) and 4% of the simulated Z$\rightarrow\tau\tau$ events. The $M(\ell, trk)$ distribution in leptoquark events is shown in Figure 4.3c. The fraction of leptoquark events rejected by this requirement increases for larger values of leptoquark mass.

There are 171 OS events and 56 SS events which survive the both Z removal requirements. From simulation, $\sim$ 80 Z$\rightarrow\tau\tau$ events are expected to survive both Z removal requirements.

4.5 $\not\!\!E_t$ Direction: Di-tau Selection

So far, the requirements on the data select lepton plus jet events. There are several sources of this event topology, discussed in the next chapter. Lepton plus jets events form the background to di-tau events when a jet in the event passes the taujet selection cuts: neither the lepton nor the jet are produced from a tau decay. A significant source of lepton plus jets events with large $\not\!\!E_t$ is W + jets events in which $W \rightarrow \ell\nu$.

Figure 4.4a show the $\not\!\!E_t$ distributions in the data for events passing both Z removal criteria. This is compared to the number of events expected from a simulation of W+ jets, with $W \rightarrow \ell\nu$ (Figure 4.4b, dashed). There are substantial uncertainties in the W yield from the cross section and modeling of the jet fragmentation. The uncertainties in the W + jets cross sections are on the order of 10% . The fragmentation functions determine whether a jet has associated charged tracks which satisfy

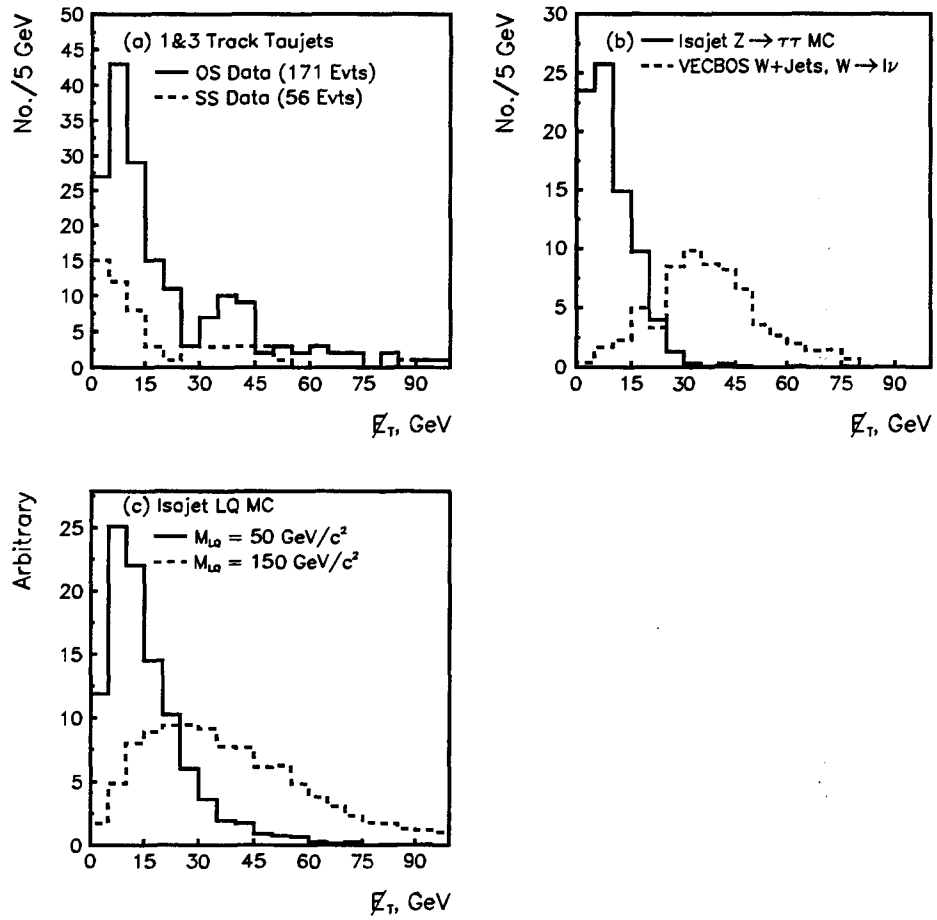

Figure 4.4: The missing transverse energy distributions for events passing both Z removal vetoes. Plot (a) shows the $\not\!\!E_t$ distributions in the opposite-sign lepton + taujet data (solid) and in the same–sign lepton + taujet data (dashed). The component at $\not\!\!E_t \gtrsim 30$ GeV is attributed to W + jets production. Plot (b) shows the $\not\!\!E_t$ distribution in simulated W + jets events (dashed) and simulated $Z \rightarrow \tau\tau$ events (solid). The integrated luminosities of the W and Z Monte Carlos samples are normalized to that of the data. Plot (c) shows the $\not\!\!E_t$ distribution in simulated scalar leptoquark events with $M = 50$ GeV/c^2 (solid) and $M = 150$ GeV/c^2 (dashed). A requirement to reject W + jets events also rejects leptoquark events for large M_{LQ}.

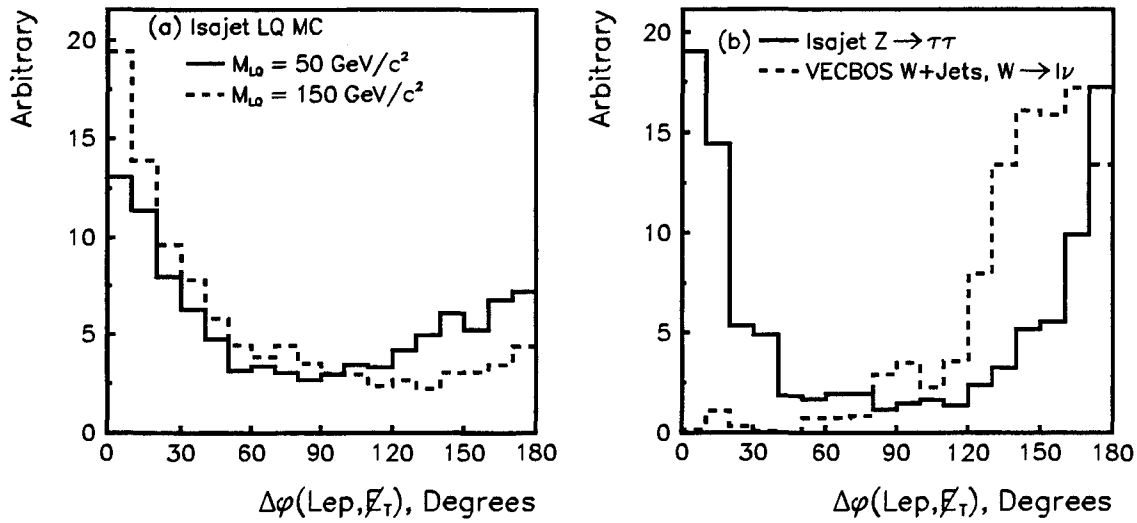

Figure 4.5: $\Delta\phi(\ell, \not\!\!E_t)$ distributions in (a) leptoquark, and (b) $Z \to \tau\tau$, and W + jets simulated events passing both Z removal vetoes. Requiring $\Delta\phi(\ell, \not\!\!E_t)$ to be small rejects W + jets events while accepting $\sim 50\%$ of simulated leptoquark events.

the taujet selection criteria. What is important is the shape of the $\not\!\!E_t$ distribution: there is clearly a component of W + jets in the data. Figures 4.4b-c show the $\not\!\!E_t$ distribution for two sources of di-tau events, $Z \to \tau\tau$ and LQ $\overline{\text{LQ}} \to \tau b\, \tau b$. Requiring $\not\!\!E_t < 25$ GeV can remove the W + jets component and retain a large fraction of a leptoquark signal for low M_{LQ}. However such a requirement is inefficient for high mass leptoquarks. A different variable must be used reduce the W + jets backgrounds.

The $\not\!\!E_t$ in leptoquark events comes primarily from the neutrinos in tau decays. This also holds for $Z \to \tau\tau$ events. In both cases, the direction of $\not\!\!E_t$ is correlated with the direction of the visible tau decay products – the lepton and the taujet. Neutrinos are produced in each tau decay. But since leptonic decays contain two neutrinos, the the total $\not\!\!E_t$ lies along the electron or muon direction more often than that of the taujet. However, in W + jets events, the $\not\!\!E_t$ and lepton come from the W decay. Therefore the lepton and $\not\!\!E_t$ necessarily form a large opening angle. As described

in Section 3.6 , only the *transverse* direction of the missing energy is calculated in the data. Thus, the variable of interest is $\Delta\phi(\ell, \not\!\!E_t)$, the separation in ϕ between the electron or muon and $\vec{\not\!\!E}_t$. Figure 4.5 shows the $\Delta\phi(\ell, \not\!\!E_t)$ distribution for simulated leptoquark, $Z \rightarrow \tau\tau$, and $W+$ jets events. Clearly this variable discriminates between W events and di-tau events. Requiring $\Delta\phi(\ell, \not\!\!E_t)$ to be small can reject the W events while retaining a substantial portion of the di-tau events.

The $\Delta\phi(\ell, \not\!\!E_t)$ requirement is chosen to maximize the significance of a leptoquark signal compared to that of the W + jets background from Monte Carlo simulation. Simulated W + jets events and leptoquark ($M_{LQ} = 50$ GeV/c^2) events are used to model the $\Delta\phi(\ell, \not\!\!E_t)$ distributions for background and signal respectively. The leptoquark significance, $\frac{S}{\sqrt{B}}$, is given by the relative numbers of signal events, S, and the relative number of background events, B, satisfying $\Delta\phi(\ell, \not\!\!E_t) < \Phi$. The events used in both samples satisfy all leptoquark criteria discussed in the previous sections. Also the events must have at least two jets in addition to the lepton and taujet. This jet requirement is discussed in the next section. The significance is calculated as a function of Φ and is shown in Figure 4.6. The maximum near 50° determines the di-tau selection requirement $\Delta\phi(\ell, \not\!\!E_t) < 50°$. This result varies only within a few degrees depending on the choice of M_{LQ}.

The $\Delta\phi(\ell, \not\!\!E_t)$ distribution in the data is shown in Figure 4.7. The number of tracks requirement on the taujets is removed, and the sample is split into two categories: one in which the taujet has 1 or 3 tracks (the usual requirement), and the other in which the "taujet" has 2, or ≥ 4 tracks[1]. Relaxing the requirement on the number of tracks gives a sample of events with a negligible contribution from real taus. Each category is split yet again into same-sign and opposite-sign lepton + taujet samples. Real di-tau events contain taujets with 1 or 3 tracks, and the lepton and taujet will have opposite-sign charges. The events where the lepton and taujet have same-sign

[1]Taujets by definition have 1 or 3 associated tracks. This requirement is relaxed occasionally to illustrate a point, in which case quotes are used.

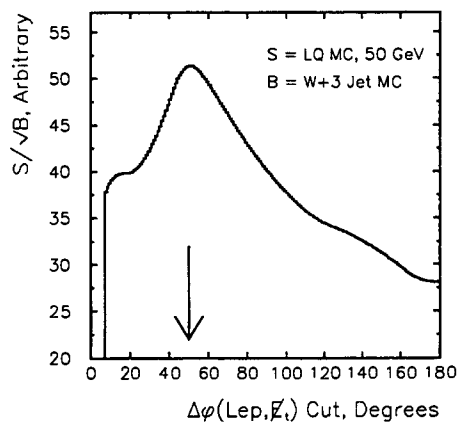

Figure 4.6: The leptoquark significance, $S/\sqrt{B}$ as a function of maximum $\Delta\phi(\ell, \not\!\!E_t)$. Simulated leptoquark events ($M = 50$ GeV/c^2) provide the signal $\Delta\phi(\ell, \not\!\!E_t)$ distribution (S), and simulated W + jets events provide the background $\Delta\phi(\ell, \not\!\!E_t)$ distribution (B). S = the relative fraction of leptoquark events satisfying $\Delta\phi(\ell, \not\!\!E_t) < \Phi(\text{cut})$. B = relative fraction of W + jets events satisfying the same. The maximum in $S/\sqrt{B}$ at 50° motivates the di-tau selection requirement $\Delta\phi(\ell, \not\!\!E_t) < 50°$. The events used satisfy all leptoquark criteria (including $N_{jet} \geq 2$)

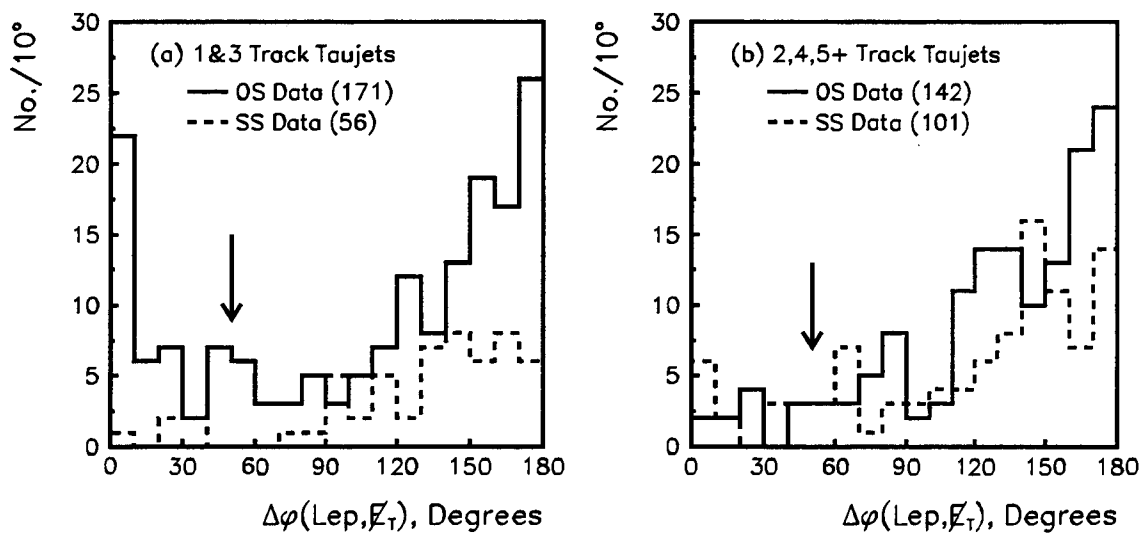

Figure 4.7: The $\Delta\phi(\ell, \not\!\!E_t)$ in the lepton + taujet data passing both Z removal vetoes. The solid histograms are opposite-sign lepton + taujet pairs; the dashed are same-sign pairs. Plot (a) contains the events with 1- and 3-track taujets. Plot (b) contains events with 2- and $\geq$4- track "taujets," The events in (b) do not contain $\tau^+\tau^-$ pairs. The same-sign events in (a) also do not contain $\tau^+\tau^-$. The peaks at 0 and 180 in the opposite-sign data indicate the presence of $\tau^+\tau^-$ pairs. The arrows indicate the requirement to select these events: $\Delta\phi(\ell, \not\!\!E_t) < 50°$.

Taujet Track Mult.	OS	SS
1-Track Taujet	27	1
3-Track Taujet	17	4
2- and ≥ 4 Taujet	11	14

Table 4.2: The breakdown by track multiplicity of lepton + taujet events passing $\Delta\phi(\ell, \not\!\!E_t) < 50°$. $Z \rightarrow \tau\tau$ is expected to contribute 36 ± 5 events to the OS 1- and 3-track lepton + taujet events.

charges are not from $\tau^+\tau^-$ pairs, and thus are from a background process. Events where the "taujet" has 2 or ≥ 4 tracks are backgrounds also. Therefore the $\Delta\phi(\ell, \not\!\!E_t)$ distributions from the same-sign event and from the opposite-sign events with 2- or ≥ 4 track "taujets" provide an estimate from the data for the background $\Delta\phi(\ell, \not\!\!E_t)$ shape. The opposite-sign sample with 1- or 3-track taujets contains the di-taus from $Z \rightarrow \tau\tau$ and its backgrounds. The excess of events near $\Delta\phi(\ell, \not\!\!E_t) = 0°$ and 180° over the same-sign rate in Figure 4.7 is suggestive of $Z \rightarrow \tau\tau$ events (Figure 4.5b). Requiring $\Delta\phi(\ell, \not\!\!E_t) < 50°$ yields 44 opposite-sign and 5 same-sign events with 1- or 3-track taujets. From simulation, 43% of leptoquark events satisfy the $\Delta\phi(\ell, \not\!\!E_t)$ requirement for $M_{LQ} = 50$ GeV/c^2, and 44% of $Z \rightarrow \tau\tau$ events satisfy the $\Delta\phi(\ell, \not\!\!E_t)$ requirement. **The OS events with 1- and 3- track taujets are di-tau candidates.** The breakdown by taujet track multiplicity is given in Table 4.2. The expected yield of OS lepton plus taujet events from all sources is 42 ± 5 events using the method presented in the next chapter. Of these, 36 ± 5 $Z \rightarrow \tau\tau$ events are expected.

The track multiplicity of the taujets in all events satisfying $\Delta\phi(\ell, \not\!\!E_t) < 50°$ is shown in Figure 4.8a. The opposite-sign distribution shows an excess of 1- an 3-track taujets over 2- and ≥ 4 track "taujets." This is a classic signature of hadronic tau decays at hadron colliders [93, 94, 95]. Furthermore, the same-sign distribution contains no such excess. This indicates that the sources of the same-sign lepton plus taujet pairs do not create a 1- and 3-track excess in the opposite-sign distribution.

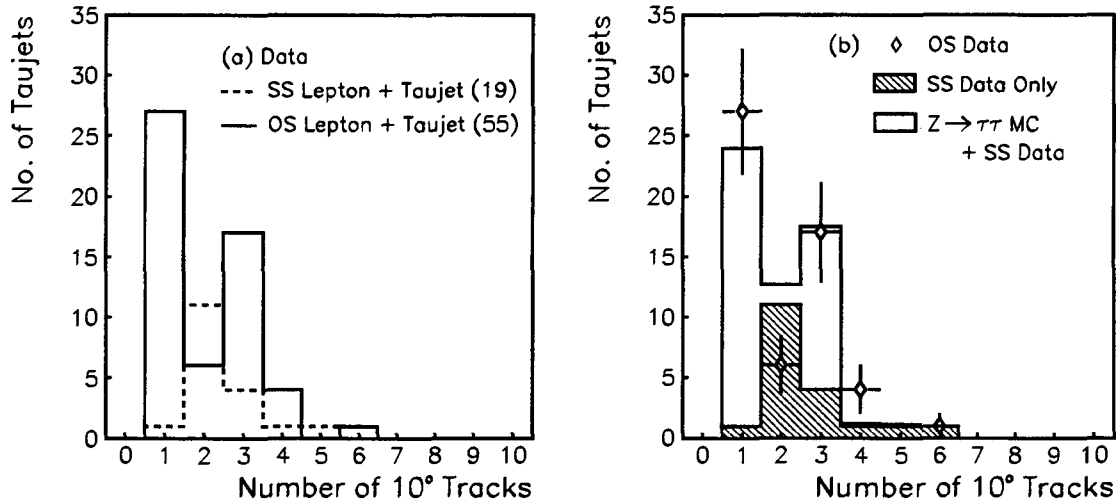

Figure 4.8: Taujet track multiplicity for data satisfying the the di-tau selection. Plot (a) shows the track multiplicity of the taujet in opposite-sign lepton + taujet events (solid) and in same-sign lepton + taujet events (dashed). The excess of 1 and 3 track taujets in the opposite-sign lepton plus taujet sample is a signature of hadronic taus. Plot (b) shows the OS data (points) compared to the expected yield of $Z \rightarrow \tau\tau$ events from simulation and the expected fakes contribution from the SS data.

The opposite-sign taujet multiplicity distribution shown in Figure 4.8b is estimated using the method in the next chapter. The observed opposite-sign multiplicity is described well by simulated $Z \rightarrow \tau\tau$ events plus the multiplicity in the same-sign data as a fakes estimate.

4.6 Number of Jets: Leptoquark Selection

The largest Standard Model source of $\tau^+\tau^-$ pairs is Z production with $Z \rightarrow \tau\tau$. The Z bosons may be produced in association with jets through QCD processes as shown in Figure 4.9. The jets in leptoquark events are produced in the leptoquark decay. Therefore, the properties of the jets in leptoquarks and $Z \rightarrow \tau\tau$ events may be used to

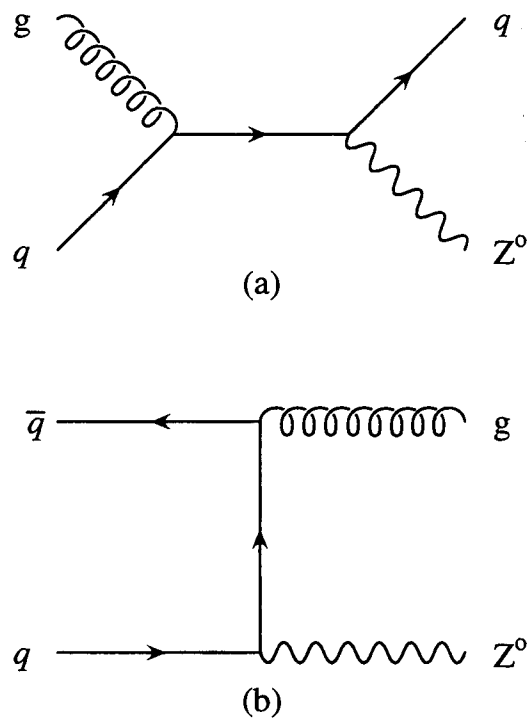

Figure 4.9: Two diagrams for $\mathcal{O}(\alpha_s)$ Z production.

distinguish the two processes. Figure 4.10 shows the E_t spectrum of the leading jet in simulated $Z \rightarrow \tau\tau$ and leptoquark events satisfying the $\Delta\phi(\ell, \not\!\!E_t)$ requirement. The jet E_t distributions in $Z \rightarrow \tau\tau$ and leptoquark events are markedly different for large leptoquark masses, $M_{LQ} = 150$ GeV. But for leptoquark masses near the bounds from direct searches, $M_{LQ} \sim 50$ GeV, the leading jet E_t distribution does not distinguish $Z \rightarrow \tau\tau$ events from leptoquark events.

However, the jet multiplicity in leptoquark events is expected to be higher than that in $Z \rightarrow \tau\tau$ events. The jet multiplicity from simulated leptoquark and $Z \rightarrow \tau\tau$ events is shown in Figure 4.11. The jet multiplicity, N_{jet}, is the number of jets with $E_t > 10$ GeV and $|\eta| < 4.2$. The multiplicity in Z events falls steeply with increasing N_{jet} since these are higher order processes in α_s. The jets in leptoquark events arise from the leptoquark decays, so the average jet multiplicity increases for larger M_{LQ}. The jets in events with $N_{jet} \geq 3$ may also originate from gluons radiated in the initial or final states.

Placing a requirement on the number of jets improves the rejection of di-tau pairs from the $Z \rightarrow \tau\tau$. The jet multiplicity, N_{jet}, is the number of jets with $E_t > 10$ GeV. The E_t threshold is a compromise between maximizing the efficiency for jets in leptoquark events and avoiding fluctuations from the underlying event. The requirement $N_{jet} \geq 2$ is made to select leptoquark events. **There are no leptoquark events observed in the data satisfying $N_{jet} \geq 2$.** About 42% of simulated leptoquark events satisfy $N_{jet} \geq 2$.

A summary of the analysis and event yield is listed in Table 4.3.

4.7 Features of the Di-tau Candidate Sample

Before the number-of-jets requirement, 36 ± 5 $Z \rightarrow \tau\tau$ events are expected in the di-tau candidate sample from Monte Carlo simulation. In this section, the kinematic distributions of the di-tau candidates are compared to the expectations from simulated

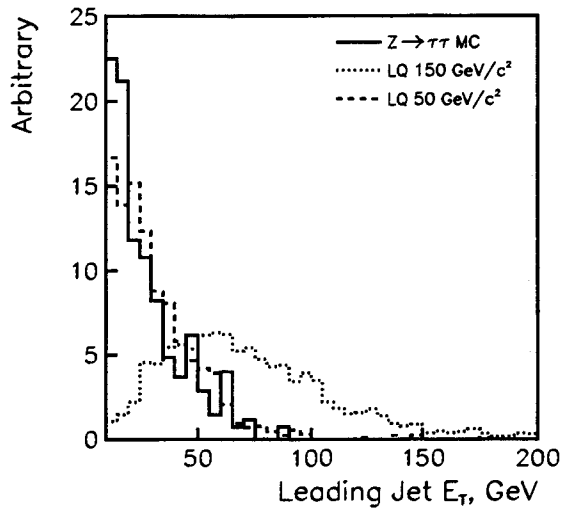

Figure 4.10: The leading jet E_t distributions for simulated $Z \rightarrow \tau\tau$ and leptoquark events satisfying $\Delta\phi(\ell, \not\!\!E_t) < 50°$.

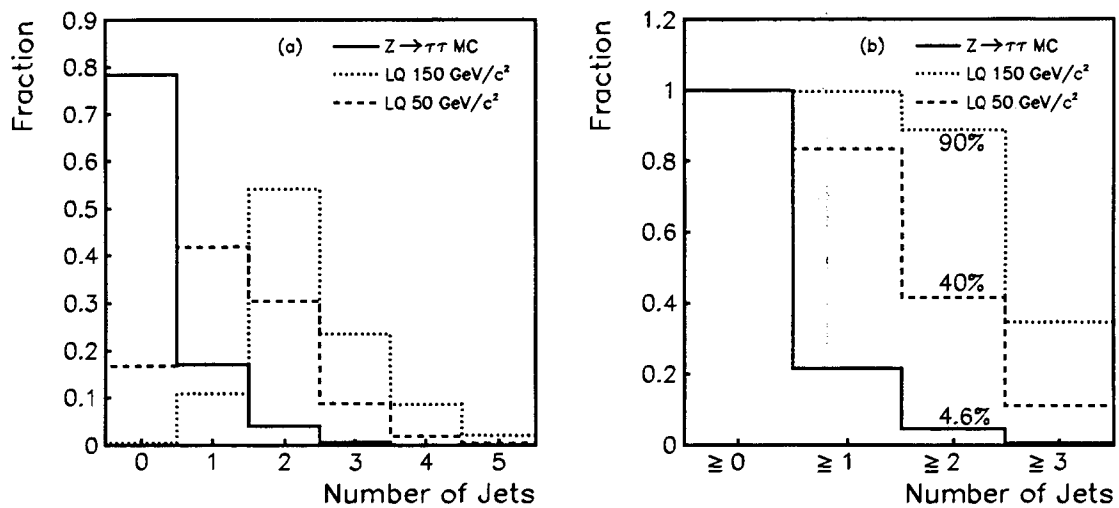

Figure 4.11: The exclusive (a) and inclusive (b) jet multiplicity in simulated $Z \rightarrow \tau\tau$ and leptoquark events. The jets counted here have $E_t > 10$ GeV and $|\eta| < 4.2$. The events entering these plots satisfy the di-tau selection $\Delta\phi(\ell, \not\!\!E_t) < 50°$.

	Lepton + Taujet Events	
Passing Requirement	# OS	# SS
Lepton + Taujet Selection	995	621
Lepton Isolation	501	241
Taujet Isolation	212	69
Z Removal: $M_{\ell\ell}$	191	62
Z Removal: M(ℓ,Lead Trk)	171	56
Di-tau Selection: $\not\!\!E_t$ Direction	44	5
Leptoquark Selection: $N_{jet} \geq 2$	0	0

Table 4.3: Lepton plus taujet yield in data

di-tau events and the taujet fakes estimate from the same–sign lepton plus taujet data.

The inclusive jet multiplicity in the di-tau candidate sample can be found in Figure 4.12a. The real tau component is dominated by Z production, with $Z \rightarrow \tau\tau$. There are 6 OS and 2 SS events with 1 jet, $E_t > 10$ GeV. The E_t distribution of these jets is shown in Figure 4.12b.

Figures 4.13a-c show the E_t of the lepton and taujet, the $\not\!\!E_t$, and the lepton type for the di-tau candidates. The average taujet E_t is larger than that of the lepton for several reasons. First, leptonic tau decays typically have less visible energy to begin with than hadronic tau decays do. Furthermore, the $\not\!\!E_t$ direction cut preferentially selects the lepton plus taujet pairs where $E_t(\ell) < E_t(taujet)$. For these events the $\not\!\!E_t$ magnitude is larger, and $\phi(\not\!\!E_t)$ is less subject to calorimeter fluctuations. The muon+jet trigger requirement in the Run 1B muon sample also biases the taujets to higher E_t. Figure 4.13d shows that the candidates are distributed between electron + taujet and muon + taujet events as expected from the leptonic tau branching fractions and lepton detection geometric coverage.

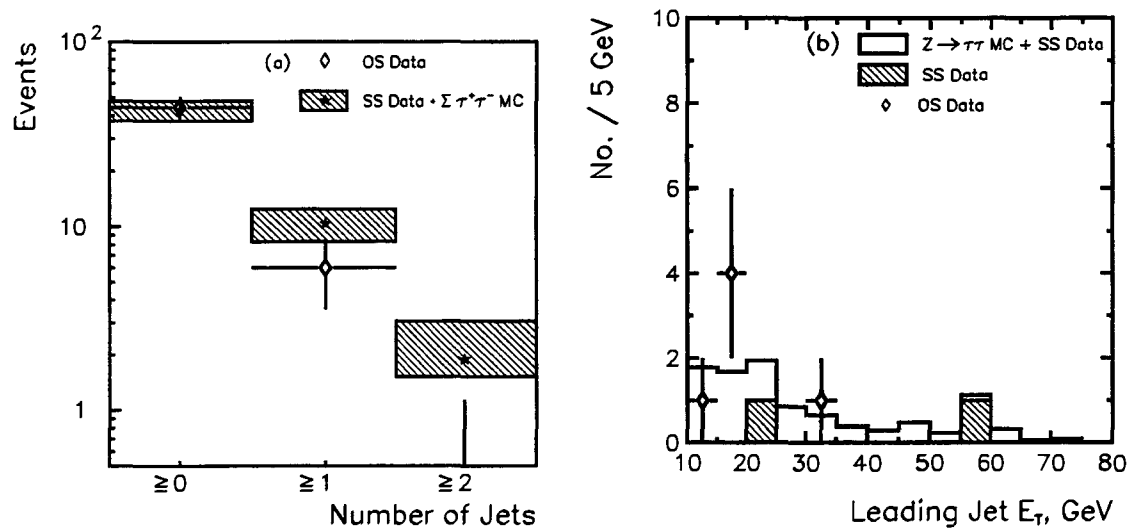

Figure 4.12: The (a) inclusive jet multiplicity for jets with $E_t(jet) > 10$ GeV and $|\eta| < 4.2$ and (b) the leading jet E_t in events passing the di-tau selection $\Delta\phi(\ell, \not\!\!E_t) < 50°$. The open points are the opposite-sign lepton + taujet data. In plot (a) the shaded histogram is the expected jet multiplicity from simulations of the $\tau^+\tau^-$ contributions from $Z \rightarrow \tau\tau$, $\gamma^* \rightarrow \tau\tau$, $t\bar{t}$, and diboson event, and a fakes estimate using the same sign lepton + taujet data. There are 6 OS events and 2 SS events with 1 jet having $E_t(jet) > 10$ GeV and $|\eta| < 4.2$.

Quantities associated with the taujet are plotted in Figures 4.14 and 4.15. The tracking and calorimeter plots in Figures 4.14 show reasonable agreement between the di-tau candidates and expectations from backgrounds and simulated $Z \rightarrow \tau\tau$ events. The p_t distributions of the taujet tracks follow the $Z \rightarrow \tau\tau$ predictions, and the E_t/p_t plots (Figures 4.14c and d) show that the fraction of energy carried by the charged hadrons in candidate taujets is consistent with the expectations for hadronic tau decays. The three-track mass in the data (Figure 4.15a) falls in the range expected for tau decays, and the taujet EM fraction (Figure 4.15b) is also typical of hadronic tau decays.

The $\Delta\phi$ between the lepton and taujet is shown in Figure 4.16a. Since most of the candidate events are expected to be from $Z \rightarrow \tau\tau +$ 0 jets, the lepton and taujet should be back-to-back in ϕ as seen in the di-tau candidate data. Figures 4.16b-c show the mass of the lepton and taujet system for two cases. The mass formed by the lepton and leading taujet track, $M(\ell, trk)$, is shown in Figure 4.16b. This is one of the variables used in the Z removal cuts in Section 4.4. The mass formed by the the lepton and taujet calorimeter cluster can be seen in Figure 4.16c. Again, there is reasonable agreement between the data and prediction.

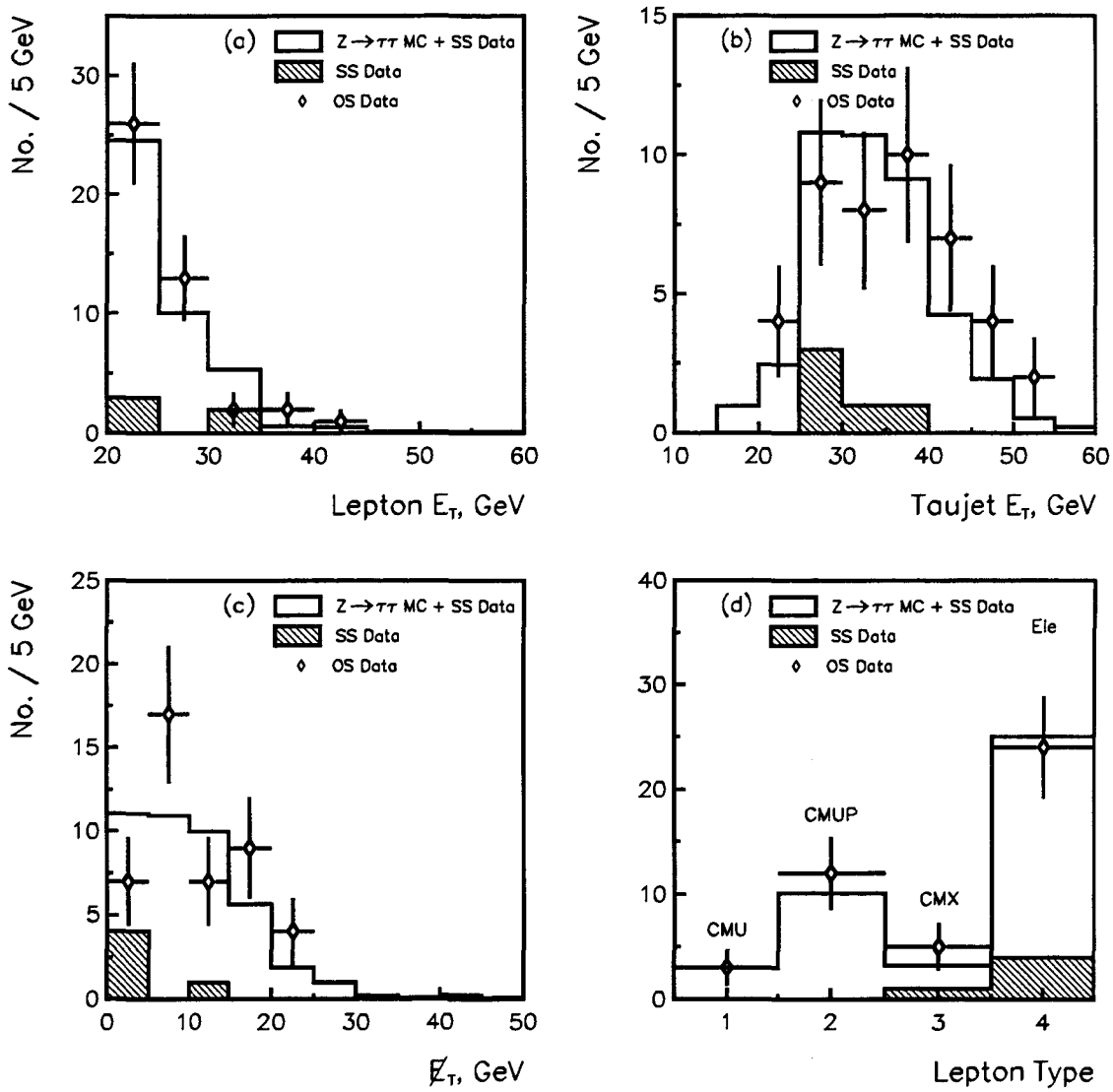

Figure 4.13: Kinematic quantities of the $Z \rightarrow \tau\tau$ candidates compared to the expectations from simulated $Z \rightarrow \tau\tau$ events and a fakes estimate from the same-sign lepton + taujet data.

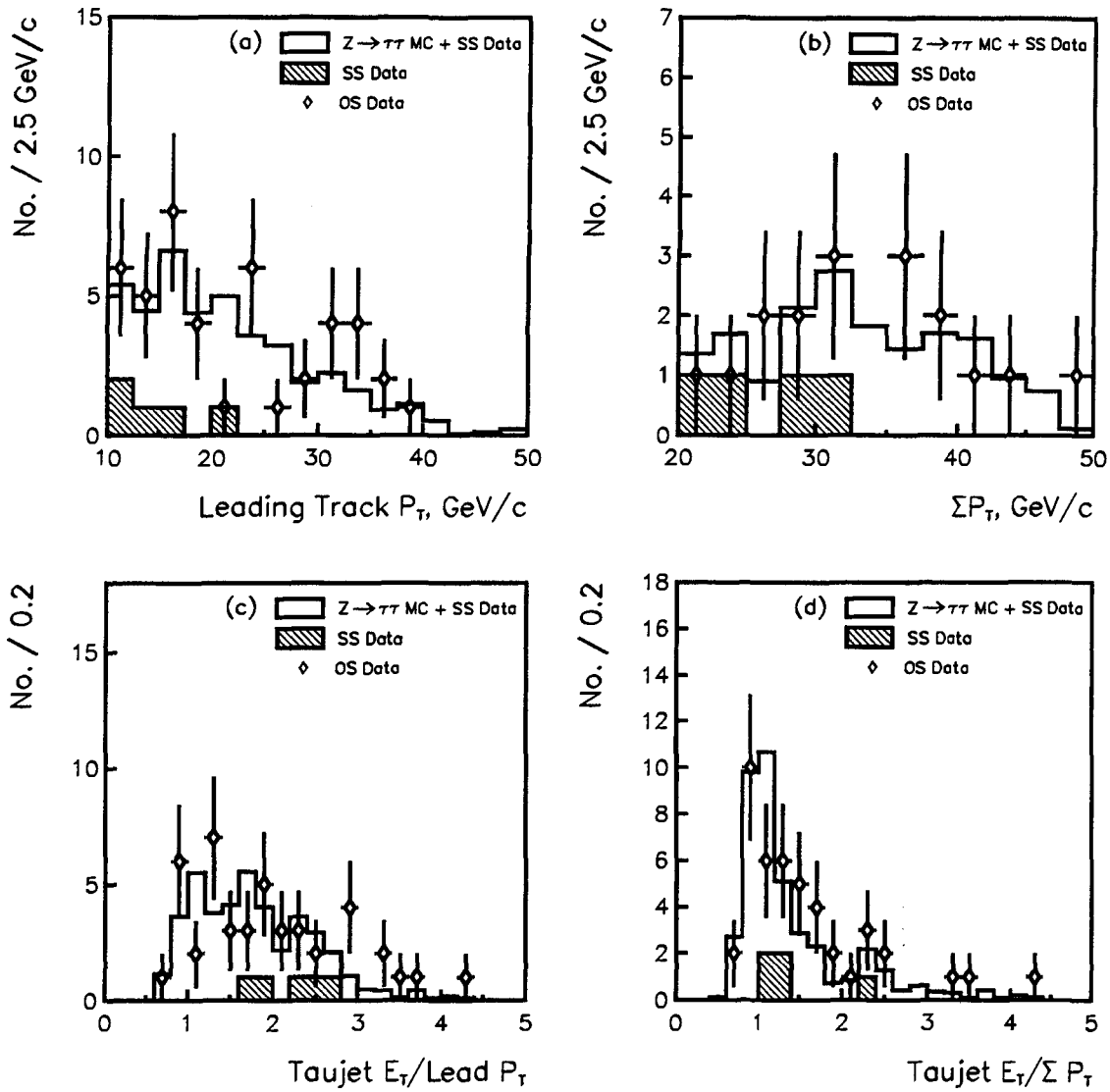

Figure 4.14: Kinematic quantities of the $Z \rightarrow \tau\tau$ candidates compared to the expectations from simulated $Z \rightarrow \tau\tau$ events and a fakes estimate from the same-sign lepton + taujet data. The variable $\sum p_t$ is the scalar sum p_t of the taujet tracks.

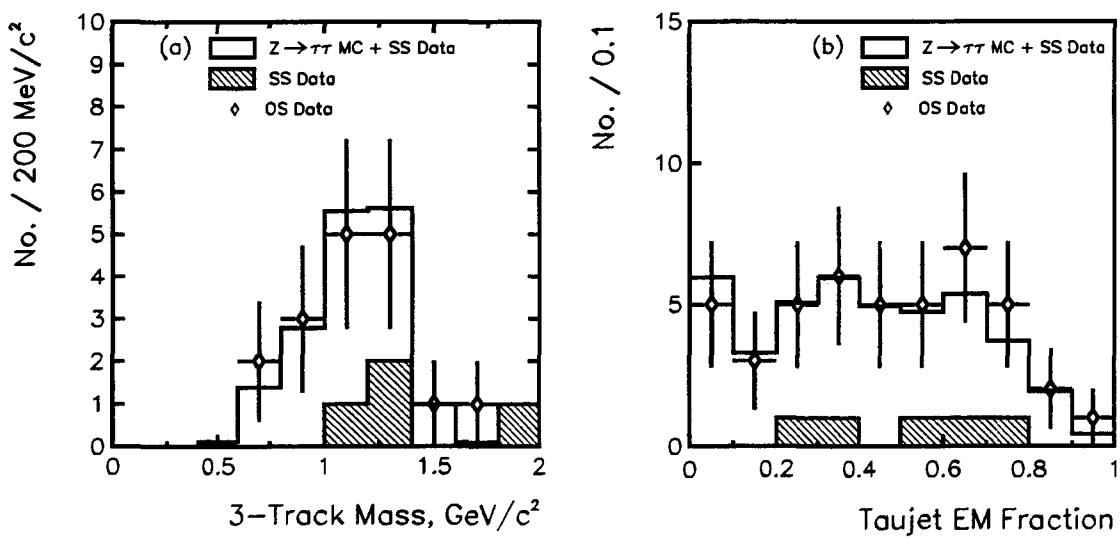

Figure 4.15: Kinematic quantities of the $Z \rightarrow \tau\tau$ candidates compared to the expectations from simulated $Z \rightarrow \tau\tau$ events and a fakes estimate from the same-sign lepton + taujet data.

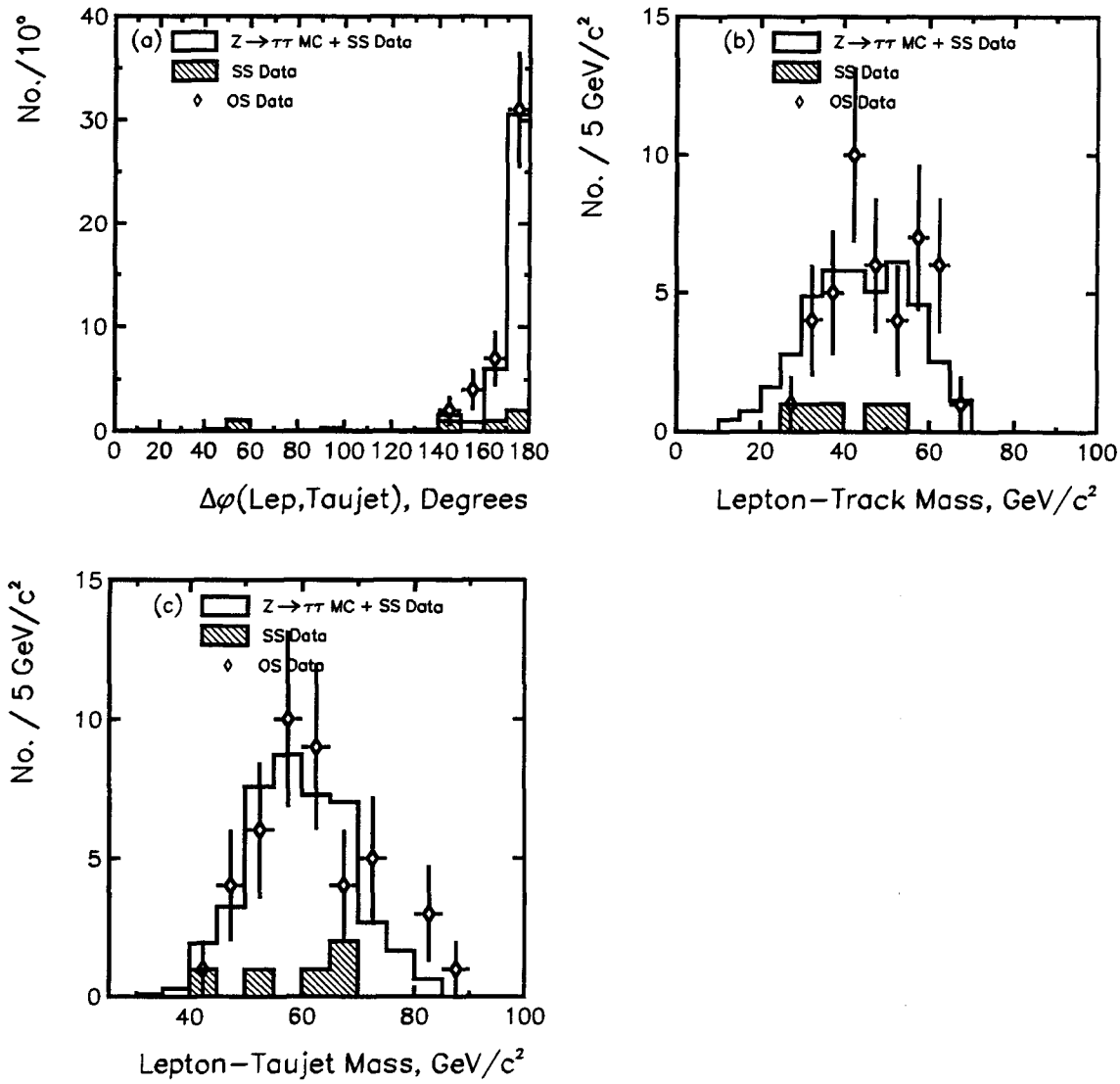

Figure 4.16: Kinematic quantities of the $Z \rightarrow \tau\tau$ candidates compared to the expectations from simulated $Z \rightarrow \tau\tau$ events and a fakes estimate from the same-sign lepton + taujet data. The upper right plot is the distribution of the mass formed by the lepton and the leading track of the taujet. The lower left plot is the distribution of the mass formed by the lepton and the taujet calorimeter cluster,

Chapter 5

Background Estimation

In the previous chapter, the selection criteria for leptoquark events was described. Although no leptoquark candidates were found, a sample of 44 di-tau candidate events was extracted. This chapter describes the method employed to estimate the composition of the di-tau candidate sample and the number of events from Standard Model processes expected to satisfy the leptoquark selection criteria. The technique uses both the predictions from Monte Carlo event generation and simulation (MC) and the fakes estimate taken from the lepton + taujet data. An overview and motivation for the method are given in Section 5.1. In Section 5.2, the backgrounds to di-tau and leptoquark events are discussed and the estimates from each source are made. Finally, assumptions in determining the backgrounds are checked in Section 5.3.

5.1 Overview of Method

Production of Z bosons decaying to $\tau^+\tau^-$ is the largest source of tau pairs expected from Standard Model processes. As described earlier, di-tau events with the final state $\tau\tau \to (\ell\nu\nu)(\tau_h\nu)$ are selected by requiring a lepton and hadronic tau jet. This lepton plus jet signature is not unique to $Z \to \tau\tau$ events. Table 5.1 lists Standard Model processes which also produce the lepton plus jet signature. Several of the

Process	Real	Fake
$Z \rightarrow \tau\tau$	$\surd$	
$\gamma^* \rightarrow \tau\tau$	$\surd$	
W+jets,$W \rightarrow \ell\nu$		$\surd$
WW,WZ,ZZ	$\surd$	$\surd$
$t\bar{t}$	$\surd$	$\surd$
$b\bar{b}$		$\surd$
QCD multijet		$\surd$

Table 5.1: Lepton plus taujet sources. Fakes processes are those with a gluon or quark makes a taujet, with a fake lepton, or with an lepton not from W, Z, or tau decay. The real sources are the defined as .not. fake. The expected event yields from real sources are estimated from Monte Carlo simulation

processes contain $\tau^+\tau^-$ pairs as a possible final state ($W^+W^- \rightarrow \tau^+\tau^-$ for example). However each process may also pose a background to $\tau^+\tau^-$ events if a quark or gluon fragments to form a taujet. The processes in Table 5.1 are classified as real or fake lepton plus taujet sources based on the origin of the lepton and the taujet. The real sources are defined as those in which the taujet is produced from a hadronic tau decay and the electron or muon is produced in the decays of W, Z, γ^*, heavy quarks, or taus. The fake sources are those in which the taujet is from a quark or gluon, or where the electron or muon is from a source other than those listed above. For instance, events with a muon from the decay-in-flight of a pion or kaon, or with an electron from the Dalitz decay of a π° would be classified as a fake lepton plus taujet source. The processes in which the electron or muon are not from the boson, heavy quark, or tau decays are collectively called QCD-multijet sources.

Ideally the expected event yield from each source would be determined from Monte Carlo simulations. The predicted event yields for the fake and real sources would then contain uncertainties associated with the cross sections for each process and detector effects such as the calorimeter response. However, the fake sources have an additional uncertainty not present for the real sources. The electron, muons, and taujets from

the real sources are produced in the decays of W, Z, γ^*, heavy quarks, or taus. In the case of the fake sources, the fragmentation of quarks and gluons yields a taujet. Furthermore, the electrons or muons in the QCD multijet processes as defined above are also produced from the hadronization of quarks or gluons. Thus the effect of fragmentation uncertainties is larger for QCD multijet processes. This is especially problematic since these events have an average $\not\!\!E_t$ similar to that of simulated events from low mass leptoquarks. This is seen in a comparison between the $\not\!\!E_t$ distribution from simulated leptoquark events and the $\not\!\!E_t$ distributions in two samples of events from the data that are dominated by QCD multijet processes.

Two Samples Dominated by QCD Multijet Events

Non-isolated Lepton Sample: These events satisfy all the signal sample requirements before $\Delta\phi(\ell, \not\!\!E_t) < 50°$ (Sections 4.1-4.4) *except* that the lepton isolation requirement $I_{cal} < 0.1$ is replaced by $I_{cal} > 0.3$. This selects events having leptons with jet activity nearby.

QCD Jet Sample: A dijet sample is selected from events satisfying a Level 2 jet trigger. One of the jets chosen at random must satisfy the taujet selection criteria. A lepton is not required.

Figure 5.1 shows the $\not\!\!E_t$ distribution in (a) simulated leptoquark events ($M_{LQ} = 50$ GeV/c^2) and (b) in same-sign lepton + taujet events in the data ($Q_\ell \times Q_{\tau jet} = +1$). The events in both plots satisfy all leptoquark search requirements before the $\Delta\phi(\ell, \not\!\!E_t)$ requirement. The same-sign lepton + taujet data have a negligible $\tau^+\tau^-$ content by construction. These are compared with the $\not\!\!E_t$ distributions in the two samples dominated by QCD multijet events described above (Figures 5.1c-d). The $\not\!\!E_t$ distribution of the same-sign lepton + taujet sample contains a W-like component (cf. Figure 4.4) at high $\not\!\!E_t$ and component at low $\not\!\!E_t$ similar to $\not\!\!E_t$ distributions of the QCD multijet samples. The similarity at low $\not\!\!E_t$ between the two QCD-dominated samples

and the the same-sign lepton + taujet events in the leptoquark suggests a method for determining the fake backgrounds independent of Monte Carlo simulations.

The lepton plus taujet events before the $\Delta\phi(\ell, \not\!\!E_t)$ requirement contains 171 opposite-sign lepton + taujet events ($Q_\ell \times Q_{\tau jet} = -1$) and 56 same-sign events ($Q_\ell \times Q_{\tau jet} = +1$). Di-tau events and events from the fake sources enter the opposite-sign sample, whereas only the fakes enter the same-sign sample. If the fake sources populate the same- and opposite-sign samples with equal probability, the fake content in the opposite-sign sample can be estimated by the number of events in the same-sign sample. The contribution from the real lepton + taujet sources can be estimated from Monte Carlo simulations. Then the expected number of events in the opposite-sign sample is given by

$$\mathcal{N}_{OS}^{expect} = \mathcal{N}_{SS}^{data} + \sum_{real} \mathcal{N}_{OS}^{MC} \tag{5.1}$$

$\mathcal{N}_{SS}^{data}$ is the number of same-sign lepton + taujet events observed in the data, and $\sum \mathcal{N}_{OS}^{MC}$ is the number of opposite-sign events predicted from MC, summed over the real sources. The advantage of this method is that it yields an estimate from *all* fake sources combined, including QCD multijets, from events with the same characteristics as the $\tau^+\tau^-$ signal. This method relies on the assumption that the fake rate is same-sign/opposite-sign symmetric. This assumption is discussed and tested in Section 5.3.

5.2 Background Estimates from Monte Carlo Simulations

The expected event yields from real lepton plus taujet processes are estimated from Monte Carlo simulations as follows. Each physics process is modeled using a QCD shower Monte Carlo event generator (ISAJET [66], PYTHIA [82], HERWIG [104]) or a matrix element Monte Carlo in the case of the W/Z + multijet processes (VECBOS [105]). The parton shower Monte Carlos generate the initial hard scattering process

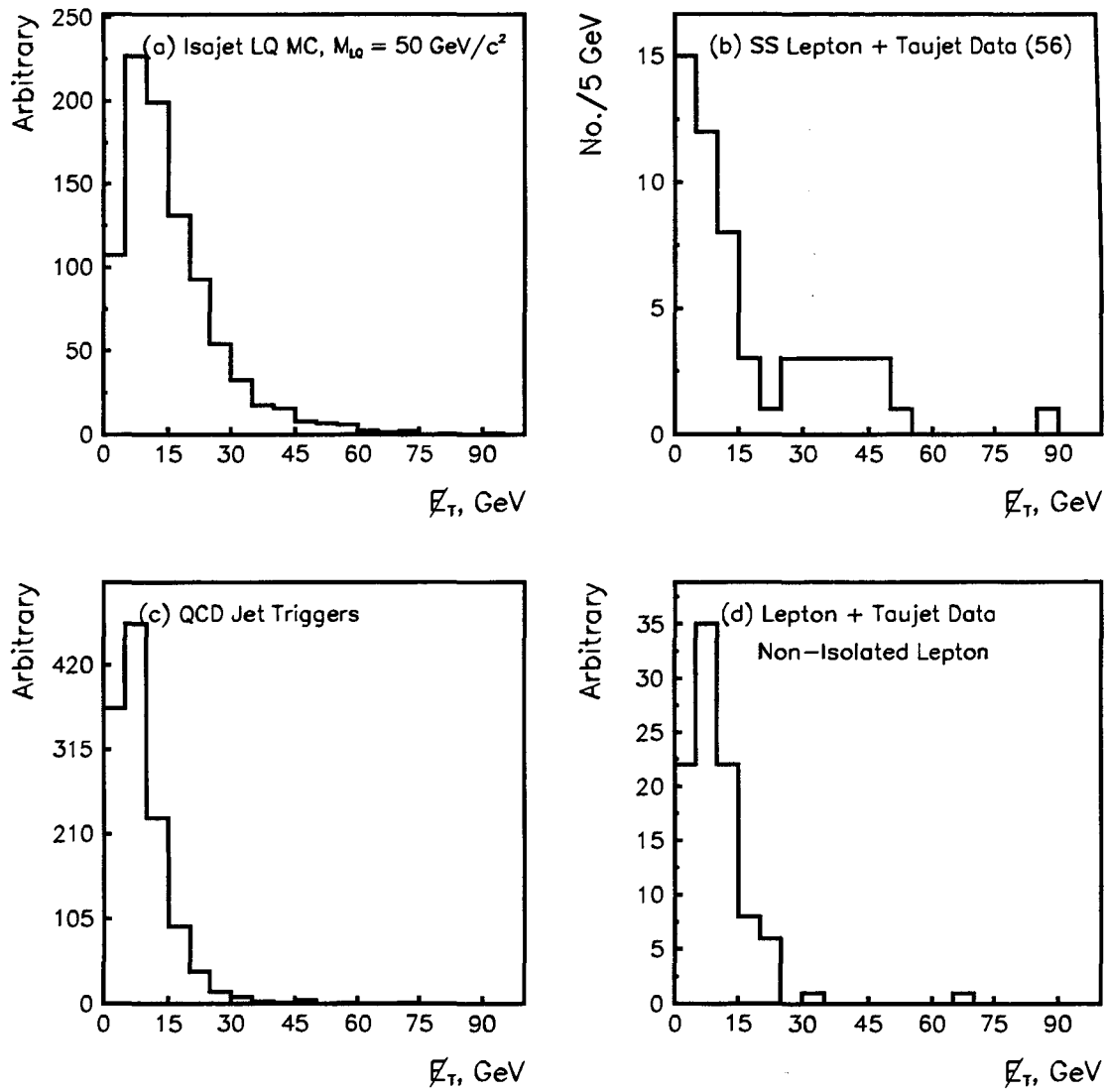

Figure 5.1: The $\not\!\!E_t$ distributions in (a) simulated leptoquark events, (b) SS lepton + taujet data, (c) events from QCD Jet triggers, and (d) lepton + taujet data (non-isolated lepton). Events in all plots except (c) satisfy all requirements before $\Delta\phi(\ell, \not\!\!E_t) < 50°$. The events in (d) contain leptons with $I_{cal} > 0.3$ instead of $I_{cal} < 0.1$.

(eg. $q\bar{q} \rightarrow Z$) according to tree level matrix elements. These are convoluted with the parton distribution functions (as in Equation 1.6). The initial and final state partons are incorporated into initial and final state parton shower cascades involving gluon and $q\bar{q}$ radiation [84]. Phenomenological models are used to describe the p and $\bar{p}$ remnants which do not participate in the hard scatter (the "underlying event"). The VECBOS Monte Carlo provides only the four momenta of the partons involved in the hard scatter. Therefore VECBOS is interfaced with a Monte Carlo based on HERWIG to generate the initial and final state parton shower cascades. The main difference between the Monte Carlo event generators is in the modeling of radiation processes. ISAJET uses an independent fragmentation model wherein radiation from each parton occurs independently from the rest of the event. HERWIG and PYTHIA both use a more realistic models of radiation in which color correlations between all partons in the initial and final state are taken into account. Next, unstable particles from the collision are decayed. Since each Monte Carlo program treats the decays of taus and b hadrons slightly differently, these particles are "re-decayed" using a consistent set of decay Monte Carlos. For tau decays, the TAUOLA decay libraries [91, 92] are used. The b hadrons are re-decayed using the QQ Monte Carlo [106], a library of routines developed by the CLEO Collaboration. The event is then are passed through a fast simulation of the CDF detector [67]. This simulation treats the calorimeter modules as homogeneous bodies rather than layers of active and absorber material. It uses parametrizations of the detector response derived from test beam data. This parametrization includes modeling of the detector response near calorimeter module boundaries, such as those in ϕ between the 15° central wedges and in η between the east and west halves of the central calorimeter.

For each primary lepton type, central electrons and central muons CMU/P μ, and CMX μ, the number of simulated Monte Carlo events, $\mathcal{N}_\ell$, satisfying the $\Delta\phi(\ell, \not\!\!E_t)$ and number-of-jets requirements is found as described in the next chapter. If a generated tau points to the taujet, the event is classified as real. This is for reals/fakes

bookkeeping purposes.

Next the integrated luminosity of each Monte Carlo sample is normalized to that of the data using the following relation

$$N_{exp} = \sum_{\ell\, types} \frac{\mathcal{N}_\ell \cdot \varepsilon(\ell ID) \cdot \varepsilon(\ell trg) \cdot \int \mathcal{L}dt(\ell\, data\, set)}{\int \mathcal{L}dt(MC\ sample)}, \quad \ell = e \text{ or } \mu \tag{5.2}$$

N_{exp} is the expected number of events passing the given requirement. The lepton data sets consist of Run 1A e's, Run 1B e's, Run 1A CMU/P μ's, Run 1B CMU/P μ's, and Run 1B CMX μ's, with luminosities listed in Table 4.1. The lepton trigger and identification efficiencies, $\varepsilon(trig)$ and $\varepsilon(\ell_{ID})$ are those determined from the data in Sections 3.3.5, 3.4.2, 6.1.3.

In the following estimates, a 10% uncertainty is assigned due to uncertainties in the calorimeter response. This is based on the results from Section 6.2.3.

5.2.1 $Z \rightarrow \tau\tau + \geq n$ Jets

Two Monte Carlos are used to simulate this process: ISAJET and VECBOS. A 500 pb^{-1} ISAJET Monte Carlo sample of $Z \rightarrow \tau\tau$ events is used to estimate the *inclusive* $Z+ \geq 0$ jets contribution in the data. The ISAJET cross section has been normalized to the CDF measurement, $\sigma \cdot B(Z \rightarrow e^+e^-) = 231 \pm 9$ pb (stat+syst) [69].

ISAJET uses the leading order matrix element calculations for the $Z+0$ jet process. Additional jets may emerge from the initial and final state parton showers. To better estimate the contribution from the $Z+ \geq 1$ jet and $Z+ \geq 2$ jet processes, the VECBOS Monte Carlo is used. VECBOS uses a leading-order matrix element calculation for the $Z+n$ parton process. The partons are fragmented using model based on the HERWIG Monte Carlo which takes into account color correlations between parton in the initial and final states. A 2800 pb^{-1} sample of events was generated. The VECBOS cross section has been scaled up by a K-factor of 1.73 ± 0.21 to account for next-to-leading order contributions. The K-factor is determined by comparing the observed rate of

$Z(\rightarrow e^+e^-)+ \geq 1$ jet events measured in the data with the cross section prediction from VECBOS [70]. The expected number of $Z \rightarrow \tau\tau$ events passing the $\Delta\phi(\ell, \not\!\!E_t)$ requirement are listed below. In 72 pb^{-1} of data, a total of 36.4 ± 4.7 events are expected, with 1.69 ± 0.36 events satisfying the $N_{jet} > 2$ requirement.

$$\begin{aligned} N(Z \rightarrow \tau\tau + \geq 0 \text{ jet}) &= 36.4 \pm 4.7 \text{ events, ISAJET} \\ N(Z \rightarrow \tau\tau + \geq 1 \text{ jet}) &= 7.9 \pm 1.5 \text{ events, VECBOS} \\ N(Z \rightarrow \tau\tau + \geq 2 \text{ jets}) &= 1.69 \pm 0.36 \text{ events, VECBOS} \end{aligned}$$

5.2.2 Drell Yan: $\gamma^* \rightarrow \tau\tau$

The Drell Yan production of tau pairs was also considered. A 315 pb^{-1} sample of $\gamma^* \rightarrow \tau\tau$ events was generated using the ISAJET Monte Carlo and the MRSA parton distribution functions. In 72 pb^{-1} of data, 0.8 ± 0.3 events are expected passing the $\Delta\phi(\ell, \not\!\!E_t)$ requirement.

Of these, $0^{+0.14}_{-0}$ passes the N_{jet} requirement.

$$\begin{aligned} N(\gamma^* \rightarrow \tau\tau + \geq 0 \text{ jet}) &= 0.8 \pm 0.3 \text{ events, ISAJET} \\ N(\gamma^* \rightarrow \tau\tau + \geq 1 \text{ jet}) &= 0.3 \pm 0.25 \text{ events, ISAJET} \\ N(\gamma^* \rightarrow \tau\tau + \geq 2 \text{ jets}) &= 0^{+0.14}_{-0} \text{ events, ISAJET} \end{aligned}$$

5.2.3 Top Quark Pair Production

With the data accumulated from the 1992-1995 Collider runs, the CDF and DØ Collaborations established the existence of the top quark [78, 79]. The CDF-measured top quark mass is $m_{top} = 175.6 \pm 9.1$ GeV determined from the lepton plus 4 jets channel [71]. Using this value of m_{top}, the combined cross section obtained from the

lepton plus jets and dilepton channels is $\sigma_{t\bar{t}} = 7.5^{+1.9}_{-1.6}\ pb$ [72]. In the leptoquark search, top events contribute as a real lepton plus taujet source primarily through leptonic decays of W's: $t\bar{t} \rightarrow Wb\ Wb$, $WW \rightarrow \ell\nu\ \tau\nu$, where $\ell = e, \mu, \tau$. Top events may also contribute as a fake source when a quark or gluon forms a taujet. To estimate both these contributions, a 1470 pb^{-1} sample of $t\bar{t}$ events was generated using the HERWIG Monte Carlo [104] with $m_{top} = 170$ GeV. The integrated luminosity of the MC sample has been corrected using the CDF-measured $t\bar{t}$ cross section. The $\not\!\!E_t$ in lepton + jets top events comes mainly from the neutrinos in W decays. In this case the $\not\!\!E_t$ and lepton are widely separated, so the $\Delta\phi(\ell, \not\!\!E_t)$ requirement suppresses the contribution from top events. The estimated numbers of top events passing the $\Delta\phi(\ell, \not\!\!E_t)$ requirement are listed below. Top pair production contributes 0.12 ± 0.07 events as a real source to the di-tau sample, independent of the number of jets. As a fake source, $t\bar{t}$ events are expected to contribute 0.08 ± 0.06 events, again independent of the number of jets.

$$N_{t\bar{t}} = 0.12 \pm 0.07 \text{ events, real, HERWIG}$$
$$N_{t\bar{t}} = 0.08 \pm 0.06 \text{ events, fake, HERWIG}$$

5.2.4 Diboson Production: WW, WZ, ZZ

Diboson production is a potential source of lepton plus taujet events. A next-to-leading order Standard Model calculation for diboson production at the Tevatron gives the following cross sections [73, 74, 75]

$$\sigma(p\bar{p} \rightarrow WW) = 9.5\ pb$$
$$\sigma(p\bar{p} \rightarrow WZ) = 2.5\ pb$$
$$\sigma(p\bar{p} \rightarrow ZZ) = 1.0\ pb$$

There is a 30% theoretical uncertainty associated with these cross sections.

The WW process can contribute as a real source in the di-tau sample through the decay mode $WW \to \ell\nu\ \tau\nu$, where $\ell = e, \mu, \tau$. The WW process may also contribute as a fake source when one W decays to hadron. To estimate both contributions, a sample of WW events was generated using the ISAJET Monte Carlo. This represents an integrated luminosity of 2500 pb^{-1} after correcting the cross section from ISAJET ($\sim 7\ pb$) to the next-to-leading order calculation above. A 30% theoretical uncertainty is assigned, but the total errors are dominated by the uncertainties from MC sample statistics.

$$\begin{aligned} N(WW+ \geq 0 \text{ jet}) &= 0.04 \pm 0.03 \text{ events (real), ISAJET} \\ N(WW+ \geq 1 \text{ jet}) &= 0.02 \pm 0.02 \text{ events (real), ISAJET} \\ N(WW+ \geq 2 \text{ jets}) &= 0.02 \pm 0.02 \text{ events (real), ISAJET} \\ N(WW) &= 0.02 \pm 0.02 \text{ events (fake), ISAJET} \end{aligned}$$

Monte Carlo samples of WZ and WZ events were generated using ISAJET with integrated luminosities of 2000 pb^{-1} and 2500 pb^{-1} respectively. As in the WW case, the ISAJET cross sections have been normalized to the next-to-leading order calculations above. The expected numbers of events in 72 pb^{-1} are listed below.

$$\begin{aligned} N(WZ) &= 0.02 \pm 0.02 \text{ events (real), ISAJET} \\ N(ZZ) &= 0.04 \pm 0.03 \text{ events (real), ISAJET} \end{aligned}$$

Only the MC statistical uncertainties are given.

5.2.5 Bottom Quark Pair Production

The production of $b\bar{b}$ pairs is another source electrons and muons in $p\bar{p}$ collisions. The CDF Collaboration has measured the cross section for centrally-produced b quarks with $p_t(b) > 21$ GeV/c to be $\sigma = 330\ nb$ [76]. The cross section times branching

fraction for $p\bar{p} \rightarrow Z \rightarrow \tau\tau$ is about 1000 times smaller. However, there are several effects which suppress the $b\bar{b}$ contribution in the leptoquark analysis. First, only $\sim$ 36% of the $b\bar{b}$ events contain a semileptonic b decay. Additionally, the lepton must carry most of the b-hadron energy and be well-separated from the other b decay products (see Figure 3.4). Plus the $\not\!\!E_t$ must satisfy the $\Delta\phi(\ell, \not\!\!E_t)$ requirement which would favor an energetic neutrino in $b \rightarrow \ell\nu\ X$. There must also be a jet in the event which forms an isolated taujet. Finally, there must be additional jet activity from higher-order QCD processes in order to satisfy the N_{jet} requirement. All of these effects act to reduce the chance that a $b\bar{b}$ event satisfies the di-tau or leptoquark selection criteria.

To make a quantitative estimate of the $b\bar{b}$ contribution, a sample of $b\bar{b} \rightarrow \mu X$ events was generated with the PYTHIA Monte Carlo [82]. The sample represents an integrated luminosity of 160 pb^{-1}. After applying the di-tau selection and a scale factor to account for $b \rightarrow e\nu X$, 1.0 ± 1.0 $b\bar{b}$ events are expected in the di-tau sample and 0^{+1}_{-0} events satisfying all leptoquark requirements. The uncertainties in the estimates are errors from the Monte Carlo statistics.

5.2.6 W + Jets Production, $W \rightarrow \ell\nu$

The study of the W + multijet events provides an insight to the theory of QCD. W + jets events also pose a significant background to measuring the t quark mass and $t\bar{t}$ production cross section [77, 78]. In this leptoquark search, W + multijet events are a source of fake lepton + taujet events when $W \rightarrow e\nu$ or $\mu\nu$, and an associated jet satisfies the taujet selection. Thus a $W + n$ jet event would be classified as lepton + taujet + $(n-1)$ jet event. The $\not\!\!E_t$ in these events is typically large, $\sim$ 40 GeV, and well-separated from the lepton. The latter feature was used in determining the $\Delta\phi(\ell, \not\!\!E_t)$ requirement (Section 4.5).

The VECBOS Monte Carlo was used to estimate the fake contribution from W + jets events. Samples of W + 1 jet and W + 3 jets events were generated, with

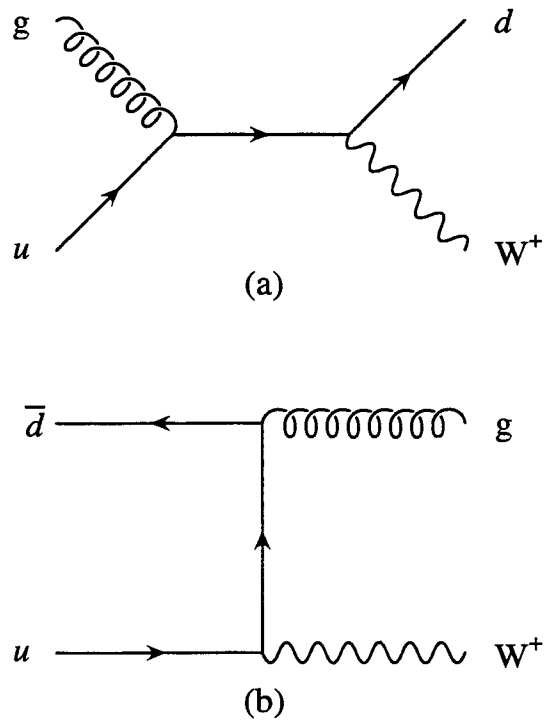

Figure 5.2: Two diagrams for $\mathcal{O}(\alpha_s)$ W production. The charge of the outgoing quark is opposite in sign to the W charge. In contrast, the charge of the jet produced by the gluon is uncorrelated with the W charge. On average, the q-W charge correlations create more opposite-sign lepton plus taujet pairs than same-sign pairs.

integrated luminosities of 480 pb^{-1} and 1800 pb^{-1} respectively. As in the case of VECBOS Z + jets, the partons from the matrix element calculation are transformed to jets using the fragmentation model which includes color coherence effects. The W cross sections have also been scaled by a K-factor determined from W + jets data ($W \rightarrow e\nu$) [80]. The estimates for W + jets events satisfying the $\Delta\phi(\ell, \not\!\!E_t)$ requirement are listed below. These events are fake lepton plus taujet events, and thus are not included in the estimate in Equation 5.1.

$$
\begin{aligned}
N(\ell + Taujet + \geq 0 \text{ jet}) &= 0.9 \pm 0.5 \text{ W+jets events, VECBOS} \\
N(\ell + Taujet + \geq 1 \text{ jet}) &= 0.5 \pm 0.3 \text{ W+jets events, VECBOS} \\
N(\ell + Taujet + \geq 2 \text{ jets}) &= 0.21 \pm 0.09 \text{ W+jets events, VECBOS}
\end{aligned}
$$

There is a 10% uncertainty associated with the K-factor, but the MC statistical errors dominate the total.

5.2.7 Summary of Backgrounds

The estimates for the expected numbers of events satisfying the $\Delta\phi(\ell, \not\!\!E_t)$ and N_{jet} requirements are presented in Table 5.2. The same-sign lepton + taujet event yield provides the estimate of the expected number of events from fakes sources. The predicted yields from the real sources estimated from simulation are added to the number of same-sign lepton + taujet events satisfying the respective requirements. This is the prescription for predicting the opposite-sign event yield (Equation 5.1). There are 44 opposite-sign lepton plus taujet events observed passing the $\Delta\phi(\ell, \not\!\!E_t)$ requirement, and 42 ± 5 opposite-sign lepton plus taujet events are predicted. No events are observed satisfying the number-of-jets requirement, while $1.9^{+1.2}_{-0.4}$ OS events are expected. There is good agreement between predicted and observed yields.

		Expected OS Events Passing	
		$\Delta\phi(\ell, \not\!\!E_t) < 50°$	$N_{jet} \geq 2$
Real	$Z \rightarrow \tau\tau$	36 ± 5	1.7 ± 0.4
	$\gamma^* \rightarrow \tau\tau$	0.8 ± 0.3	$0^{+0.1}_{-0}$
	Diboson	0.10 ± 0.05	0.08 ± 0.04
	$t\bar{t}$	0.12 ± 0.07	0.12 ± 0.07
Fake	W + jets, $W \rightarrow \ell\nu$	0.9 ± 0.5	0.21 ± 0.09
	Diboson	0.02 ± 0.02	0.02 ± 0.02
	$t\bar{t}$	0.08 ± 0.06	0.08 ± 0.06
	$b\bar{b}$	1 ± 1	0^{+1}_{-0}
	Observed events, SS Data	5	0
	$\sum_{real} N^{MC}_{OS}$	37.4 ± 5.2	1.9 ± 0.4
	Total OS Prediction	$\mathbf{42 \pm 5}$	$\mathbf{1.9^{+1.2}_{-0.4}}$
	Observed OS Yield	**44**	**0**

Table 5.2: The estimates for opposite-sign lepton plus taujet events passing the $\Delta\phi(\ell, \not\!\!E_t)$ requirement and all leptoquark criteria The prediction for the total OS yield is the predicted yield from simulation (top 4 rows) plus the number os same-sign lepton plus taujet events observed in the data.

5.3 Assumptions in the Method

The estimates presented in this chapter are meant to demonstrate that a di-tau signal exists in the data and that it is accounted for by known Standard Model physics. The most significant component in the di-tau candidate sample, $Z \rightarrow \tau\tau$, is expected to contribute 1.7 ± 0.4 events in the leptoquark signal region. The combined contribution from fake sources is estimated to be 0^{+1}_{-0} using the same-sign lepton plus taujet yield in the data. In this section, the validity of the method is discussed and tested.

There are two major assumptions behind the estimation method: 1) the fake lepton + taujet sources are equally likely to be same-sign or opposite-sign; and 2) the QCD multijet backgrounds in the opposite-sign sample are described by the same-sign sample.

At first glance, the first assumption seems invalid because charge is conserved. In

	$\not\!\!E_t < 25$ GeV		$\not\!\!E_t > 25$ GeV	
	OS	SS	OS	SS
$Z \to \tau\tau$	80 ± 11	—	2.6 ± 0.6	—
$\gamma^* \to \tau\tau$	1.1 ± 0.4	—	0.6 ± 0.3	—
W + jets	11 ± 2	2.2 ± 0.8	44 ± 5	11 ± 2
$t\bar{t}$	0.4 ± 0.1	—	1.8 ± 0.3	0.4 ± 0.1
$b\bar{b}$	1 ± 1	—	—	—
Diboson	0.28 ± 0.08	0.04 ± 0.03	1.1 ± 0.1	0.15 ± 0.07
$\sum$ (MC)	94 ± 11	2.3 ± 0.8	50 ± 5	12 ± 2
Data	124	39	47	17
OS Excess: MC	92 ± 11		38 ± 5	
OS Excess: Data	85 ± 13		30 ± 8	

Table 5.3: The excess of opposite-sign lepton + taujet events before the $\Delta\phi(\ell, \not\!\!E_t) < 50°$ requirement. The opposite-sign excess in the data is accounted for by the MC sources listed here. The MC estimates above include the contribution from fake taujets.

the cases where a quark jet satisfies the taujet selection, the charge of the taujet is correlated with that of the lepton. This is illustrated by the Feynman diagrams for the $W + 1$ jet process in Figure 5.2: the sign of the W charge is opposite that of the quark charge. There are similar correlations expected from fake lepton + taujets in W^+W^- and $t\bar{t}$ events. However, these fake processes make a negligible contribution after the $\Delta\phi(\ell, \not\!\!E_t) < 50°$ requirement is made (see Table 5.2). Furthermore, the Monte Carlo expectations discussed below and shown in Table 5.3 indicate that the same-sign rate for these processes *under estimates* their opposite-sign contributions. However, since there is no Monte Carlo estimate for the QCD multijet contribution, the same-sign/opposite-sign behavior of the QCD multijet process must be checked using the data.

To test the assumption that QCD multijet events are sign-symmetric, the predicted event yield *before* the $\Delta\phi(\ell, \not\!\!E_t)$ requirement is calculated. For this estimate, all Monte Carlo estimates discussed above are used: fake and real lepton + taujet

events. Additionally, the estimates at low $\not\!\!E_t$ and high $\not\!\!E_t$ are calculated separately. From the $\not\!\!E_t$ distributions in events from QCD jet triggers (see Figure 5.1c), virtually all of the QCD multijet contribution should enter at $\not\!\!E_t < 25$ GeV. The QCD multijet processes are expected to make up $\sim 5\%$ of the total sample for $\not\!\!E_t > 25$ GeV [81]. Table 5.3 lists the expected opposite-sign and same-sign lepton plus taujet yields estimated from Monte Carlo simulations and the yield observed in the data. If the QCD contribution is sign-symmetric, the opposite-sign excess in the data should be fully accounted for by the excess predicted by the Monte Carlos. For $\not\!\!E_t > 25$ GeV, the opposite-sign excess observed in the data is 30 ± 8 events. The excess estimated from Monte Carlo is 38 ± 5 events, mostly from W + jets production. This agreement is good, given that there are uncertainties expected in the W + jets prediction from uncertainties in the fragmentation modeling. This gives confidence that the W + jets estimate at low $\not\!\!E_t$ will be modeled reasonably well also. For $\not\!\!E_t < 25$ GeV, the opposite-sign excess observed in the data is 85 ± 13 events, and the excess expected from Monte Carlo is 92 ± 11 events. $Z \rightarrow \tau\tau$ is expected to contribute 80 ± 11 events. The agreement at low $\not\!\!E_t$ indicates that the QCD multijet contribution is sign-symmetric to a good approximation.

The studies in this chapter show that event yields from the fake lepton plus taujet backgrounds estimated from Monte Carlo simulations are small (and slightly sign-asymmetric) after the $\Delta\phi(\ell, \not\!\!E_t)$ requirement. The QCD multijet processes (for which no Monte Carlo estimates are made) are observed in the data to be sign-symmetric when the $\Delta\phi(\ell, \not\!\!E_t)$ requirement is removed. So, since the fake backgrounds from Monte Carlo simulation are small, and the QCD multijet is sign-symmetric, the same-sign lepton plus taujet event yield is a good estimate of the total yield from the fake backgrounds (Table 5.1) satisfying the $\Delta\phi(\ell, \not\!\!E_t)$ and number-of-jets requirements. Thus, the method for background estimation (Equation 5.1) presented in this chapter is sufficient to describe the fake and real lepton plus taujet backgrounds in the leptoquark search.

Chapter 6

Signal Efficiencies and Systematic Errors

The leptoquark signal efficiency, ε_{LQ}, relates the number of leptoquark events expected to satisfy the search criteria to the total number produced: $N_{LQ}^{expect} = \varepsilon_{LQ} \cdot \beta^2 \cdot \sigma \cdot \int \mathcal{L} dt$, where β is the branching ratio for LQ $\rightarrow \tau b$. The number of leptoquark pairs produced is $\sigma \cdot \int \mathcal{L} dt$ where σ is the theoretical cross section for leptoquark pairs and $\int \mathcal{L} dt$ is the integrated luminosity of the data sample. This expression for N_{LQ}^{expect} can be used to place bounds on the production cross section if no evidence for leptoquarks is found. This is discussed in detail in the next chapter. The calculation of the leptoquark signal efficiency and the systematic uncertainties which affect the leptoquark cross section bounds are presented here.

6.1 Signal Efficiency

The efficiency for detecting leptoquark pairs is expressed as following product for each lepton type, central electron, CMU-only muon, CMUP muon, and CMX muon:

$$\varepsilon_{LQ}^{i} = \mathcal{A}_{LQ}^{i} \cdot \varepsilon_{trig}^{i} \cdot \varepsilon_{\ell ID}^{i}, \quad i = \text{lepton type} \tag{6.1}$$

The lepton trigger and identification efficiencies, ε^i_{trig} and ε^i_{lID}, are estimated from real data. The acceptance for leptoquark pairs, $\mathcal{A}^i_{LQ}$, describes the efficiencies of the various geometric and kinematic requirements made to select leptoquark events. The efficiency ε^i_{LQ} is split by lepton type since the integrated luminosities, identification and trigger efficiencies vary slightly among the lepton types.

The acceptance $\mathcal{A}^i_{LQ}$ is determined as a function of M_{LQ} from Monte Carlo generated and simulated leptoquark events. $\mathcal{A}^i_{LQ}$ is separated into the following efficiencies

$$\mathcal{A}_{LQ} = \varepsilon_{sel} \cdot \varepsilon_{\ell isol} \cdot \varepsilon_{\tau isol} \cdot \varepsilon_{M\ell\ell} \cdot \varepsilon_{M\ell\text{-}trk} \cdot \varepsilon_{\Delta\phi(\ell,\not\!\!E_t)} \cdot \varepsilon_{Njet} \tag{6.2}$$

In the following discussion, the ε^i_{sel} are presented individually, while the remaining terms in Equation 6.2 are presented as combined efficiencies from all lepton types.

The ε's are defined conditionally on the previous one as follows:

$\varepsilon^i_{sel} \equiv$ the fraction of all generated leptoquark events with ≥ 1 fiducial lepton of type i with $p_t > 20$ GeV, $|z_{lep}| < 60$ cm and ≥ 1 jet with $E_t > 15$ GeV and $|\eta_d| < 1$ satisfying the taujet selection and fiducial requirements

$\varepsilon_{\ell isol} \equiv$ the fraction of events satisfying the requirements in ε^i_{sel} which also have a high-p_t lepton passing the isolation requirement, $I_{cal} < 0.1$.

$\varepsilon_{\tau isol} \equiv$ the fraction of events with an isolated lepton which also have a taujet satisfying the isolation requirement, $N_{isol} = 0$.

$\varepsilon_{M\ell\ell} \equiv$ the fraction of events surviving the lepton and taujet isolation requirements which also satisfy the Z removal requirement using the dilepton mass, $M_{\ell\ell}$: $M_{\ell\ell} < 70$ GeV/c^2 .or. $M_{\ell\ell} > 110$ GeV/c^2.

$\varepsilon_{M\ell\text{-}trk} \equiv$ the fraction of events surviving the $M_{\ell\ell}$ requirement which also satisfy the Z removal requirement using the mass formed by the lepton and leading track in the taujet, $M(\ell,trk)$: $M(\ell,trk) < 70$ GeV/c^2 .or. $M(\ell,trk) > 110$ GeV/c^2.

$\varepsilon_{\Delta\phi(\ell,\not\!\!E_t)} \equiv$ the fraction of events satisfying both Z removal requirements which also pass the di-tau requirement, $\Delta\phi(\ell,\not\!\!E_t) < 50°$

$\varepsilon_{Njet} \equiv$ the fraction of events satisfying the di-tau requirement which also have ≥ 2 jets with $E_t > 10$ GeV in addition to the lepton + taujet: $N_{jet} \geq 2$.

6.1.1 Acceptance for Scalar Leptoquarks Pairs

The ISAJET program [66] and a fast simulation of the CDF detector [67] were used to generate samples of scalar leptoquark events. There is no explicit scalar leptoquark mechanism in ISAJET. However ISAJET has the capability to generate squark-antisquark pairs ($\tilde{q}\bar{\tilde{q}}$). Squarks are spin-0 color triplet particles. Therefore pair production of squarks is the same as that of scalar leptoquark pairs, except that the t-channel the lepton exchange diagram (for leptoquarks) is replaced by a t-channel gluino exchange (for $\tilde{q}\bar{\tilde{q}}$). By setting the gluino mass to be very large, the contribution from the gluino exchange can be eliminated. Then the squark-antisquark process is the same as the leptoquark process in which the lepton exchange diagram is ignored. This is indeed what was argued in Section 1.2.7. Thus by forcing the squark to decay $\tilde{q} \to \tau b$, the $\tilde{q}\bar{\tilde{q}}$ process in ISAJET is identical to scalar leptoquark pair production.

The scalar leptoquark samples were generated with LQ masses ranging from 50 GeV to 250 GeV in intervals of 25 GeV. As seen later in this section, the detection efficiency increases sharply with larger LQ masses. Therefore the low mass sample sizes were quite large, several 100K events each, to give a statistical uncertainty in ε_{LQ} comparable to that of the high mass samples. The high mass sample sizes were typically $\sim$ 50K events each.

The lepton + taujet selection efficiency, ε_{sel}, for scalar leptoquarks is listed by lepton type in Table 6.1. The selection efficiency ranges from $(0.493 \pm 0.008)\%$ for $M_{LQ} = 50$ GeV/c^2 to $(12.2 \pm 0.1)\%$ for $M_{LQ} = 250$ GeV/c^2. The errors are statistical. The efficiencies of the other LQ requirements and the total acceptance can be found in Table 6.2. These are also plotted as a function of LQ mass in Figures 6.1–6.3. The

total acceptance for scalar leptoquark pairs, $\mathcal{A}_{LQ} \equiv \sum_i \mathcal{A}^i_{LQ}$ is $(0.039 \pm 0.002)\%$ for $M_{LQ} = 50$ GeV/c^2 and $(2.27 \pm 0.05)\%$ for $M_{LQ} = 250$ GeV/c^2.

6.1.2 Acceptance for Vector Leptoquarks Pairs

There is no such prescription for generating vector leptoquarks with the ISAJET program as there is for scalar leptoquark pairs. Instead the PYTHIA Monte Carlo generator [82] is interfaced with partonic cross sections for vector leptoquark pairs. The cross sections are discussed in Refs. [38, 39], and the calculations are supplied by the authors of Refs. [38, 39] [41].

The acceptances for the two cases of vector leptoquarks is estimated by scaling from the acceptances determined from the fully-simulated scalar LQ event samples. As discussed below, the acceptances for vector and scalar LQ pairs are the same to first order. The acceptance scaling takes into account the changes in acceptance that are attributable to the differences in the average LQ p_t and η for scalar and vector LQ pairs. This method was chosen because the scalar leptoquark event samples were quite large, and their generation and simulation were CPU-intensive.

The detection efficiency for leptoquark pairs is dominated by the kinematic requirements implicit in the leptoquark selection criteria. The detection efficiency is most strongly dependent on the p_t and η of the taus and b quarks. The tau η determines whether the tau decay products are detected in the central region. The p_t of the b quarks affect the jet multiplicity in the leptoquark event. The tau p_t affects whether the visible decay products, the hadrons or charged leptons, have sufficient p_t to satisfy the lepton or taujet selection. The tau p_t also influences the efficiency of the $\Delta\phi(\ell, \not\!\!E_t)$ requirement. High-p_t taus more readily decay to leptons with $\not\!\!E_t$ along the direction of the lepton.

There are two variables which affect the p_t of the taus and b quarks from leptoquark decays: the leptoquark mass and the leptoquark p_t. The generator-level p_t and η distributions for scalar and vector leptoquarks are compared in Figure 6.4. The

LQ Mass	CMU-τjet	CMX-τjet	CMUP-τjet	ELE-τjet	Total ℓ-τjet
50	0.043 (2)	0.055 (3)	0.126 (4)	0.269 (6)	0.493 (8)
75	0.162 (7)	0.189 (7)	0.46 (1)	0.93 (2)	1.74 (2)
100	0.32 (1)	0.36 (1)	0.94 (2)	1.86 (3)	3.47 (4)
125	0.45 (2)	0.54 (2)	1.46 (3)	2.92 (5)	5.37 (6)
150	0.61 (2)	0.74 (2)	1.98 (4)	3.78 (5)	7.12 (7)
175	0.84 (3)	0.90 (3)	2.40 (5)	4.57 (6)	8.71 (8)
200	1.01 (3)	1.08 (3)	2.93 (5)	5.09 (6)	10.12 (9)
225	1.14 (3)	1.19 (3)	3.26 (6)	5.91 (7)	11.5 (1)
250	1.23 (4)	1.28 (4)	3.49 (6)	6.24 (8)	12.2 (1)

Table 6.1: Lepton plus taujet selection efficiencies for scalar leptoquarks. The numbers in parentheses are the statistical uncertainties in the last digit.

LQ Mass	50	75	100	125	150	175	200	225	250
ℓ-τjet Selection	0.493	1.74	3.47	5.37	7.12	8.71	10.12	11.5	12.2
Lepton Isol	81.0	77.2	74.9	73.3	72.2	70.2	69.0	67.6	66.7
Taujet Isol	63.5	69.3	71.6	74.0	74.5	76.8	76.2	76.9	78.1
$M_{\ell\ell}$	96.6	96.1	95.2	94.3	94.3	93.8	92.7	92.7	92.5
M(ℓ,Lead Trk)	89.4	82.1	77.2	73.0	70.7	70.2	70.1	70.2	71.0
$\not\!\!E_t$ Direction	43	46.2	49.3	53.8	56.6	58.9	59.2	59.6	59.9
N_{jet}	42	64	76	82	88.8	88.6	88.3	91.2	90.7
Total, %	0.039 (2)	0.216 (8)	0.51 (1)	0.88 (3)	1.28 (3)	1.61 (4)	1.81 (4)	2.11 (5)	2.27 (5)

Table 6.2: The efficiencies of the leptoquark requirements from simulated scalar leptoquark events. The numbers in parentheses are the statistical uncertainties in the last digit.

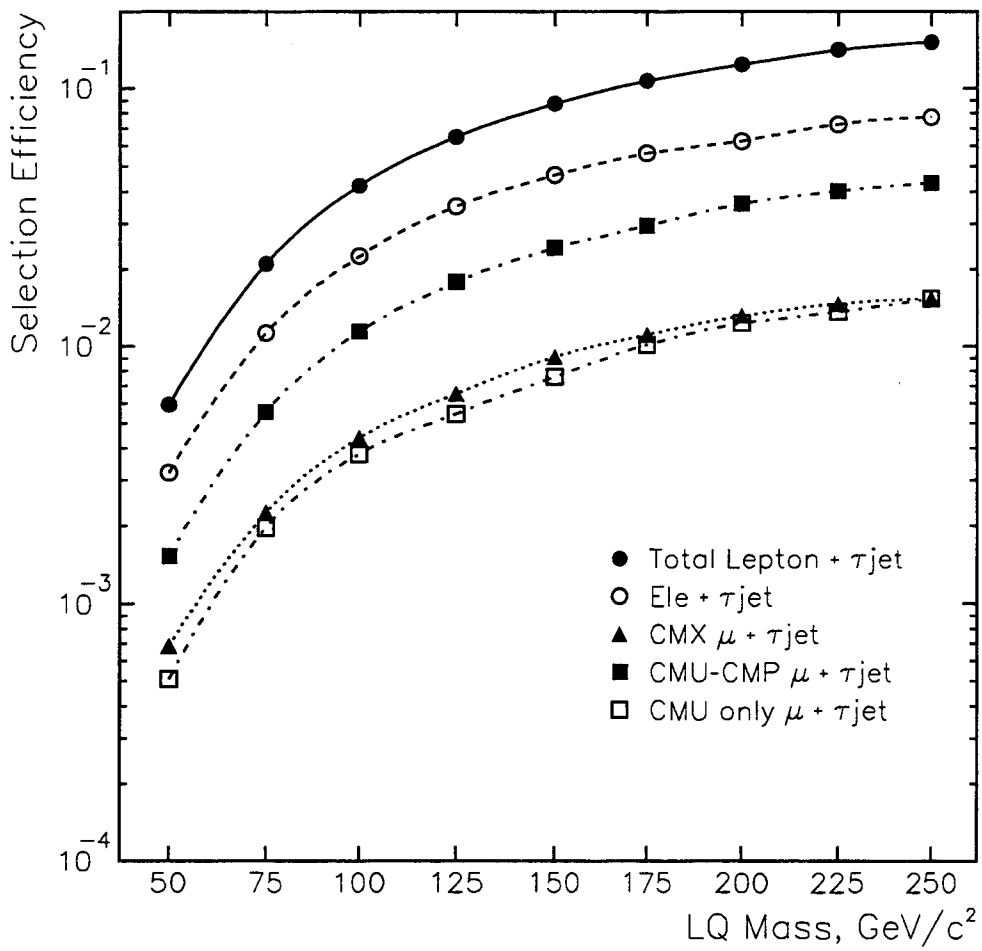

Figure 6.1: Lepton plus taujet selection efficiency for simulated scalar leptoquark pairs.

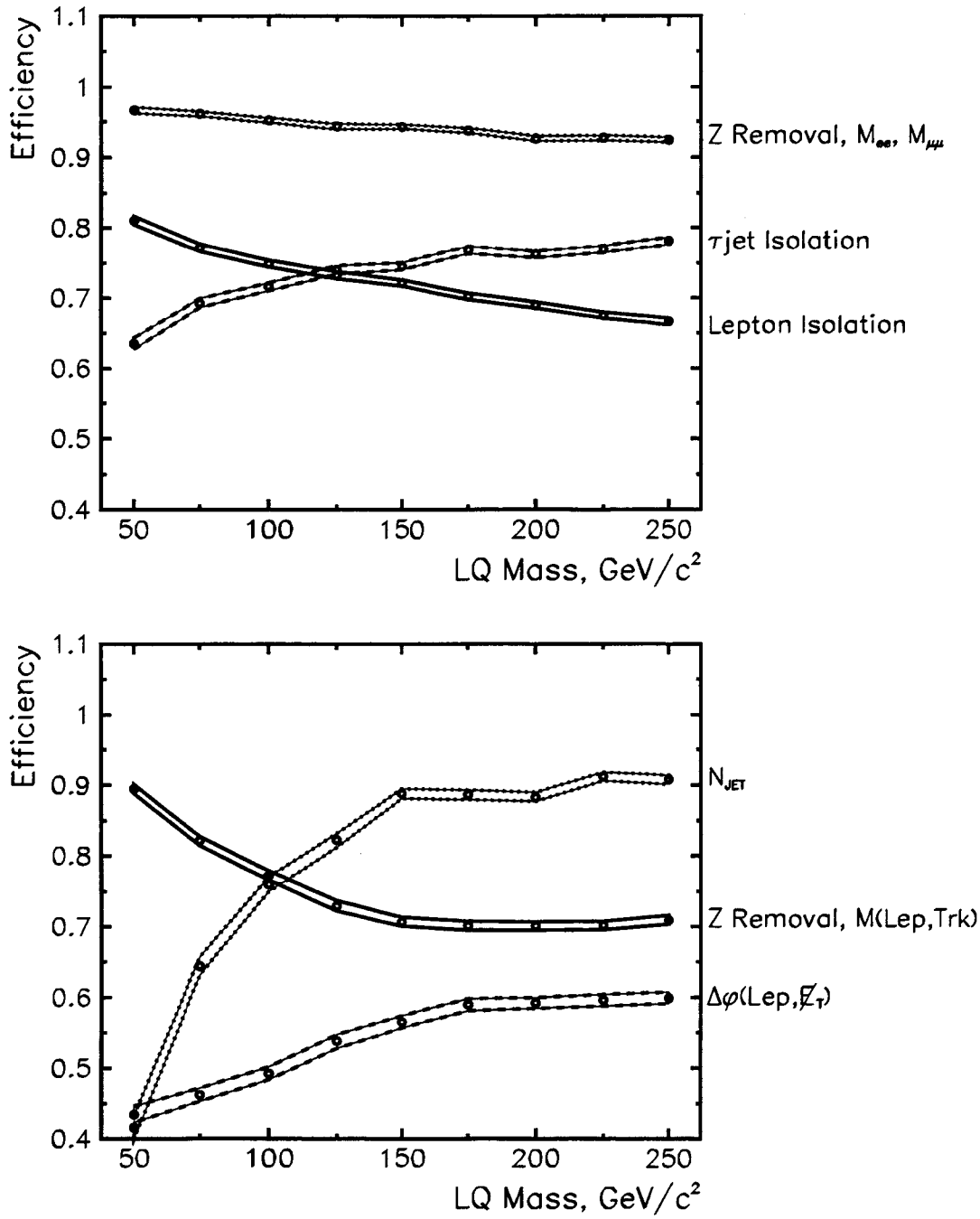

Figure 6.2: The efficiencies of the leptoquark selection criteria determined from simulated scalar leptoquark events

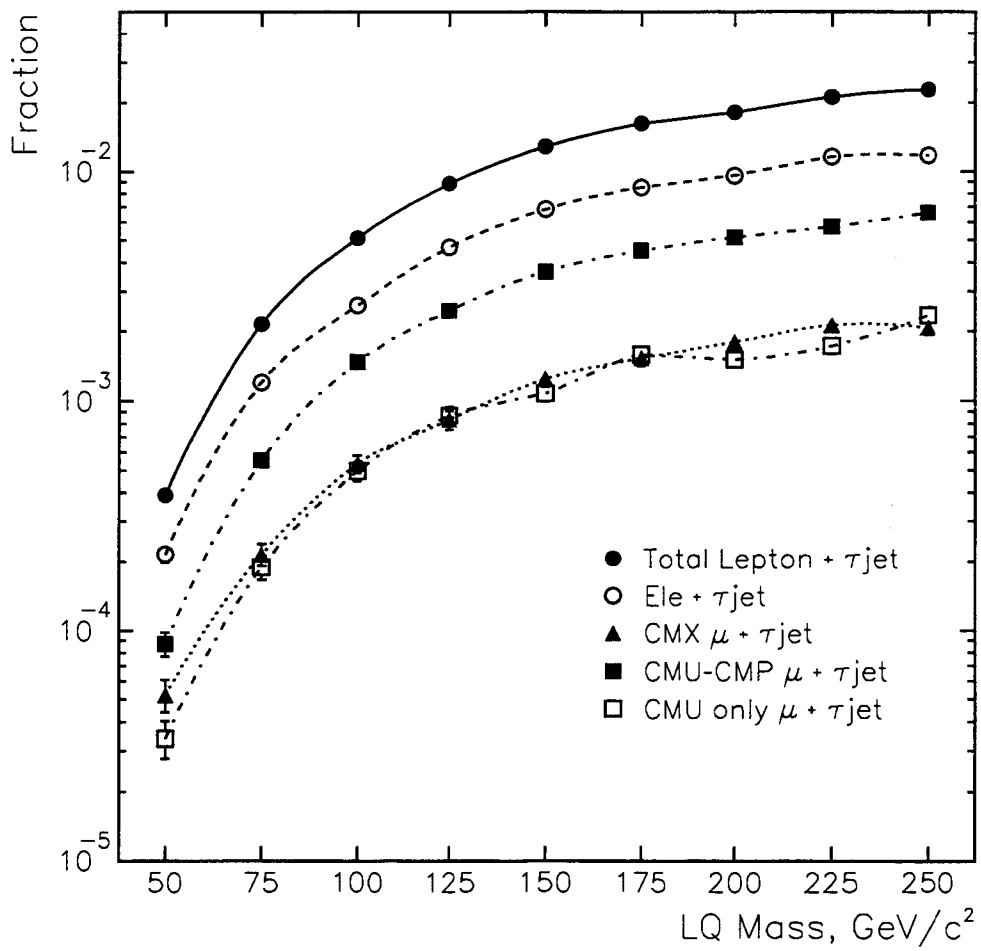

Figure 6.3: The total acceptance for scalar leptoquark pairs determined from simulated leptoquark events

events were generated with the PYTHIA Monte Carlo, but they contain no detector simulation. No requirements have been placed on the events. Two values of M_{LQ} are shown, 50 GeV/c^2 and 150 GeV/c^2, and both choices cases for the vector leptoquark anomalous coupling κ are presented. Scalar leptoquarks are produced more centrally than vector leptoquarks in all cases. But, the average p_t for both types of vector leptoquarks is larger than that of scalar leptoquarks. These differences in LQ p_t and η will cause the acceptance for vector leptoquark pairs to be different from that of scalar leptoquarks pairs.

The efficiencies for detecting vector leptoquarks estimated using the following relation:

$$\varepsilon_{LQ}(vector;\kappa) = \mathcal{R}(\text{GEN}) \cdot \varepsilon_{LQ}(scalar) \tag{6.3}$$

$$\mathcal{R}(\text{GEN}) = \frac{\varepsilon_{kin}(vector;\kappa)}{\varepsilon_{kin}(scalar)} \tag{6.4}$$

The factor $\mathcal{R}(\text{GEN})$ is the ratio of generator level kinematic acceptances, $\varepsilon_{kin}(vector;\kappa)$ and $\varepsilon_{kin}(scalar)$, for vector and scalar leptoquarks. $\varepsilon_{kin}(vector;\kappa)$ and $\varepsilon_{kin}(scalar)$ are defined as the fraction of events satisfying the following requirements:

- Lepton $p_t > 20$ GeV/c, $|\eta| < 1$, from $\tau \to \ell\nu\nu$
- Hadron $\sum p_t > 15$ GeV/c, $|\eta| < 1$, from $\tau \to hadrons\,\nu$
- $p_t(b) > 15$ GeV/c and $p_t(\bar{b}) > 15$ GeV/c

The event generator produces a the list of particles emerging from the hard collision and the associated 4-momenta. The p_t and η requirements are made on these unsimulated quantities. The 15 GeV/c threshold on the b quark p_t is appropriate since a b with $p_t \sim 15$ GeV/c typically produces a jet with $E_t \sim 10$ GeV in the calorimeter.

The qualitative behavior of $\mathcal{R}(\text{GEN})$ as a function of M_{LQ} can be deduced from the leptoquark p_t and η distributions in Figure 6.4. The kinematic acceptances for both types of vector leptoquarks will be larger than for scalar LQś at low mass. This is because vector leptoquarks have larger average leptoquark p_t for the lower

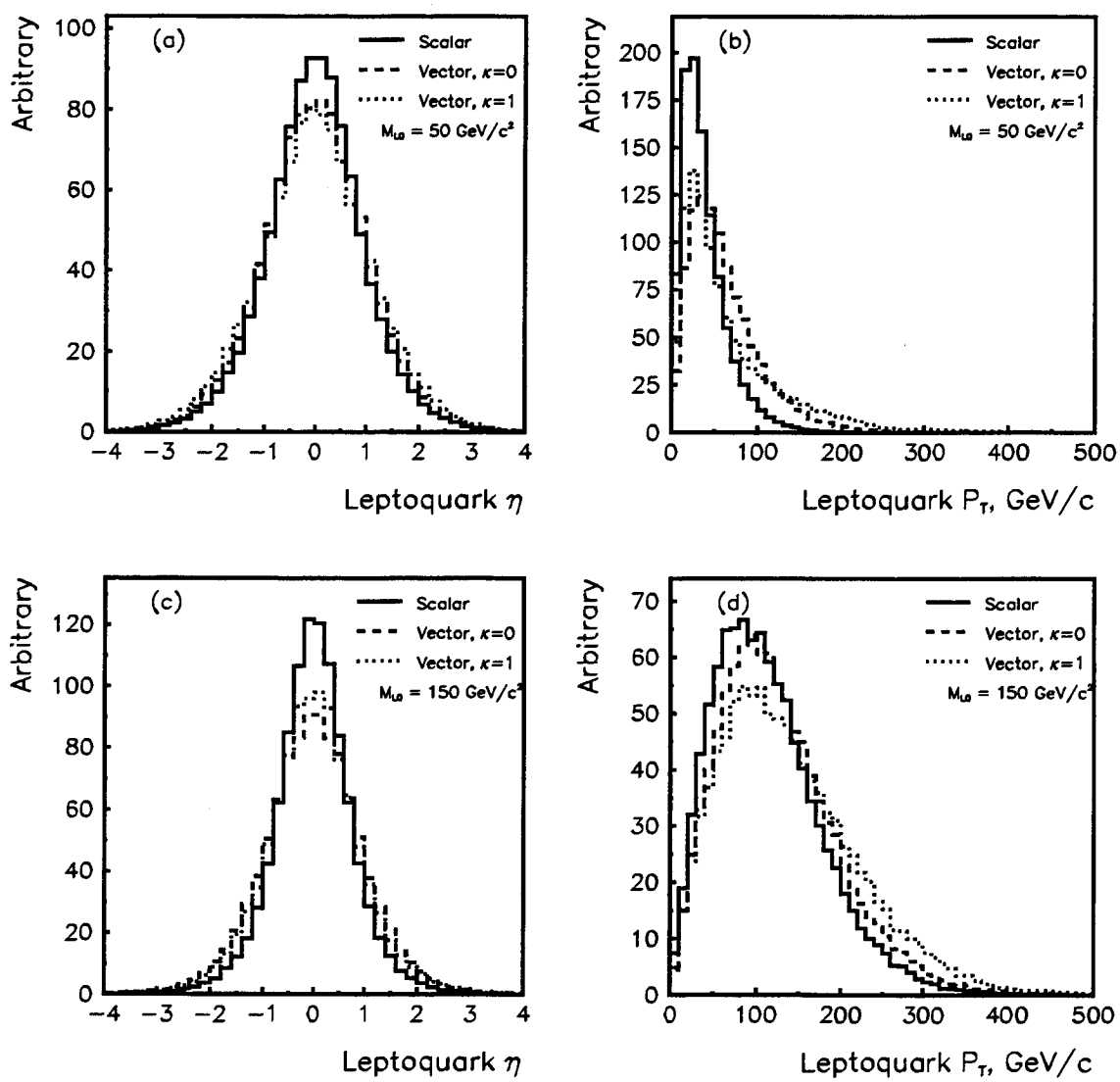

Figure 6.4: Generator-level η and p_t of scalar and vector leptoquarks. Plots (a) and (c) show the η distributions for scalar (solid), vector, $\kappa = 0$, (dashed), and vector, $\kappa = 1$, (dotted) leptoquarks. The p_t of the leptoquarks is shown in plots (b) and (d). Plots (a) and (b) are for $M_{LQ} = 50$ GeV/c^2, and (c) and (d) $M_{LQ} = 150$ GeV/c^2. No requirements have been applied. The Monte Carlos are described in the text.

masses. At higher masses, the difference in average p_t between scalars and vectors becomes less important. A modification to the leptoquark p_t distribution affects the detection efficiency less for high mass leptoquarks than for low mass leptoquarks. The leptoquark η then affects the differences in detection efficiencies between the scalar and vector cases. For all leptoquark masses, the scalar leptoquarks are produced more centrally ($\eta \sim 0$) than are vector leptoquarks. Thus the lepton and taujet are more likely to fall in the central region if the taus are from scalar leptoquark decays. For $M_{LQ} \sim 100(175)$ GeV/c^2 the detection efficiency for scalar leptoquarks is approximately equal to that of $\kappa = 0(1)$ vector leptoquarks. The values of $\mathcal{R}$(GEN) are listed in Table 6.3.

The acceptance-scaling procedure gives an estimate for the detection efficiencies for vector leptoquarks without resorting to regenerating and simulating 18 vector leptoquark samples ([2 values of κ] $\times$ [9 values of M_{LQ}]). However, the detection efficiencies derived from $\mathcal{R}$(GEN) do not include the non-kinematic effects such as taujet isolation and lepton isolation. Since these effects are neglected, there is an additional uncertainty in $\varepsilon_{LQ}(vector;\kappa)$ which does not exist for scalar leptoquarks. To estimate this uncertainty, 20K event samples of vector leptoquark ($\kappa = 0$ and 1) and scalar leptoquark events were generated with PYTHIA [1] for $M_{LQ} = 175$ GeV/c^2. These samples were then put through the full detector simulation, as was the case for the ISAJET leptoquark samples. $\mathcal{A}_{LQ}$ was determined for each sample separately. The ratios, $\mathcal{A}_{LQ}(vector;\kappa = 0)/\mathcal{A}_{LQ}(scalar)$ and $\mathcal{A}_{LQ}(vector;\kappa = 1)/\mathcal{A}_{LQ}(scalar)$ calculated using the 20K event samples were then compared to $\mathcal{R}$(GEN) . The difference between the fully-simulated and generator-level ratios was taken to be the systematic uncertainty associated with the acceptance-scaling procedure. The uncertainties were found to be 7% for $\kappa = 0$ and 10% for $\kappa = 1$ vector leptoquarks.

[1]This choice of M_{LQ} is appropriate because this is where the upper limit on the cross section for scalar leptoquark pairs is close to the theoretical cross section for vector leptoquark pairs. This is discussed in Chapter 7

	$\mathcal{R}$(GEN)	
LQ Mass	$\kappa = 0$	$\kappa = 1$
50	2.3 ± 0.1	3.1 ± 0.1
75	1.11 ± 0.03	1.32 ± 0.04
100	0.99 ± 0.02	1.11 ± 0.03
125	0.99 ± 0.02	1.06 ± 0.02
150	0.93 ± 0.02	1.01 ± 0.02
175	0.95 ± 0.02	1.00 ± 0.02
200	0.93 ± 0.02	1.00 ± 0.02
225	0.93 ± 0.02	0.96 ± 0.02
250	0.91 ± 0.02	0.94 ± 0.02

Table 6.3: Scale factors for vector leptoquark efficiencies. The listed uncertainties are statistical. We assign an additional systematic uncertainty to $\mathcal{R}$(GEN) of 7% for $\kappa = 0$ and 10% for $\kappa = 1$. These values of $\mathcal{R}$(GEN) are used to derive the vector leptoquark detection efficiencies from the relation $\varepsilon_{LQ}(vector; \kappa) = \mathcal{R}(\text{GEN}) \cdot \varepsilon_{LQ}(scalar)$.

	Muons	Electrons
Run 1A	$\varepsilon_{\ell ID} = (90 \pm 2)\%$, CMU/P	$\varepsilon_{\ell ID} = (83 \pm 1)\%$
Run 1B	$\varepsilon_{\ell ID} = (89 \pm 1)\%$, CMU/P $\varepsilon_{\ell ID} = (91 \pm 2)\%$, CMX	$\varepsilon_{\ell ID} = (80.0 \pm 0.9)\%$

Table 6.4: Identification efficiencies for isolated leptons determined from $Z \to \ell\ell$ data

6.1.3 Lepton Identification and Trigger Efficiencies

The lepton identification and trigger efficiencies are applied as probabilities for MC events passing the N_{jet} requirement to satisfy the lepton identification and trigger requirements.

The identification efficiencies for isolated leptons are measured from $Z \rightarrow ee$ and $Z \rightarrow \mu\mu$ data. The efficiencies can be found in Table 6.4. Taking the average efficiency over all detector components weighted by the relative acceptances yields $\varepsilon_{tID} = 85 \pm 0.6\%$ for leptons $p_t > 20$ GeV.

The Level 2 triggers used in this analysis are listed in Table 6.5. The plateau efficiencies have been determined from real data. The efficiencies of the inclusive muon triggers have been determined using $Z \rightarrow \mu\mu$ and $W \rightarrow \mu\nu$ data [60, 61]. For Run 1B data, muon + jet triggers are used to avoid a malfunctioning Level 2 muon trigger processor [62]. The efficiency of each muon + jet trigger is taken to be the inclusive muon trigger efficiency times the Level 2 jet trigger efficiency: $\varepsilon_{\mu jet} = \varepsilon_{\mu} \times \varepsilon_{jet}$. Here ε_{jet} is the probability that the Level 2 jet hardware cluster finder finds at least one jet with $E_t(\mathrm{L2}) > 15$ GeV.

The efficiency for the jet trigger requirement is estimated using the probability to find a Level 2-clustered jet with $E_t(\mathrm{L2}) > 15$ GeV associated with a offline-clustered jet. The probability is computed from a sample of events collected with an inclusive muon trigger and is plotted as a function of offline jet E_t in Figure 6.5 [63]. The efficiency for at least one jet in the leptoquark event satisfy the Level 2 jet requirement is expressed as the following probabilities:

$$\begin{aligned} \varepsilon_{jet} &= 1 - \mathrm{Prob}(\text{all jets fail Level 2 requirement}) \\ &= 1 - \prod_i (1 - \mathcal{P}^i_{pass}) \end{aligned} \tag{6.5}$$

Each term in the product is the probability that jet i fails the Level 2 jet requirement. This is related to the Level 2 jet trigger efficiency curve in Figure 6.5: $\mathcal{P}^i_{pass} = \varepsilon_{L2}(E^i_t)$.

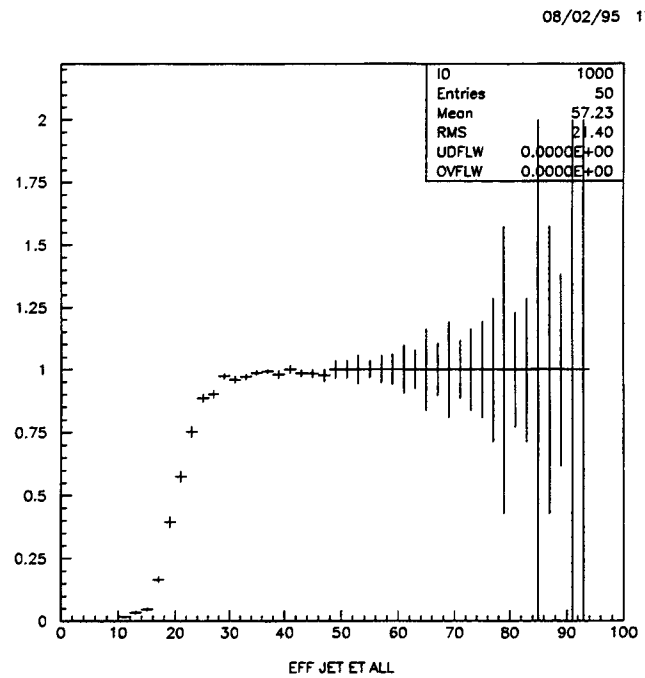

Figure 6.5: The efficiency, $\varepsilon_{L2}(E_t)$, for finding Level 2 jet $E_t > 15$ GeV as a function of offline jet E_t. This is convoluted with the jet E_t distributions from simulated leptoquark events to estimate the efficiency for the Level 2 muon+jet trigger.

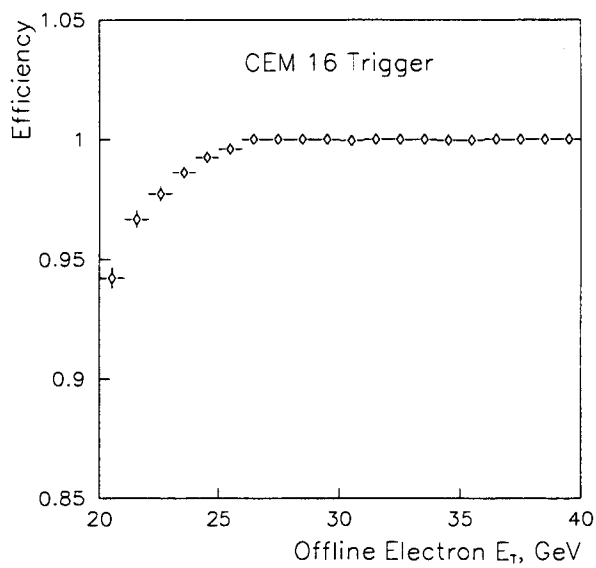

Figure 6.6: The clustering efficiency for the Level 2 16 GeV central electron trigger (CEM_16) as a function of offline electron E_t. This is determined from the data.

	Run 1A Muon Triggers	ε_{trig}, %		
Level 2	CMNP_CFT_9_2			
	CMU_CMP_CFT_9_2			
	CMUP_CFT_9_2		88.7	
	Run 1B Muon Triggers	$\varepsilon_\mu \times$	$\varepsilon_{jet}=$	ε_{trig}
Level 2	CMNP_JET_15_CFT_12			
	CMUP_JET_15_CFT_12	86.1	98	84.4
	CMX_JET_15_CFT_12	69.6	98	68.2
	Run 1A Electron Trigger		ε_{trig}	
Level 2	CEM_9_CFT_9_2		91.5	
	Run 1B Electron Trigger		ε_{trig}	
Level 2	CEM_16_CFT_12		93.2	

Table 6.5: Level 2 Lepton Triggers. The efficiency of the Level 2 jet trigger requirement, ε_{jet}, is shown for $M_{LQ} = 50$ GeV/c^2. In the trigger names, the number following "CFT" indicates the CFT track p_t threshold. For the electron triggers, the number following "CEM" denotes the Level 2 EM cluster E_t threshold. The efficiency for the CEM_16_CFT_12 trigger is the plateau value. The non-CMX muon trigger efficiencies are combined into a single efficiency. The triggers are described in Section 2.6.

The μ + jets simulated leptoquark events which satisfy the N_{jet} requirement are used to calculate ε_{jet}. For $M_{LQ} = 50$ GeV/c^2, $\sim$ 98% of the events passing all requirements also have at least one Level 2-clustered jet with $E_t(L2) > 15$ GeV. For larger leptoquark masses, the efficiency is $\geq$ 99%.

The Level 2 electron triggers used in the leptoquark search require a track found by the CFT and an EM cluster found by the hardware cluster finders. The efficiency of this trigger is the convolution of the CFT track finding efficiency and the cluster finding efficiency. The Level 2 central electron trigger during Run 1A has a plateau efficiency of 91.5 ± 0.3% [68]. The Level 2 CFT track and CEM cluster p_t thresholds are 9.2 GeV/c and 9 GeV respectively, so electrons with offline $E_t > 20$ GeV are well above the efficiency turn-on curve [65]. For Run 1B data taking, the track and cluster thresholds were increased to 12 GeV/c and 16 GeV respectively. The plateau

efficiency for this trigger is determined by the CFT efficiency to find a track with $p_t > 12$ GeV/c. This efficiency is measured using a sample of electrons which satisfy a Level 2 $\not\!\!E_t$ trigger – an independent trigger with no tracking requirements. The average efficiency is determined to be $93.2 \pm 0.2\%$. However, the EM cluster cluster requirement does not become fully efficient until $\sim$ 27 GeV. This was due to the efficiency turn-on the Level 2 CEM cluster requirement, shown in Figure 6.6. To account for this the electron E_t in simulated leptoquark events is convoluted with the efficiency curve in Figure 6.6. For $M_{LQ} = 50$ GeV/c^2, 98.8% of the events passing the $N_{jet} \geq 2$ requirement also satisfy the Level 2 16 GeV CEM cluster requirement.

The combined Level 2 trigger efficiency weighted by the relative acceptances for each detector component is 86.2 % (88.0%) for $M_{LQ} = 50$ GeV/c^2(150 GeV/c^2) respectively.

The Level 3 lepton trigger efficiencies measured in Run 1A data are $(98.6^{+0.8}_{-1.3})\%$ for muons [47], $(98.2 \pm 0.1)\%$ for electrons [68] The Level 3 efficiencies measured in Run 1B data are $(97.0 \pm 0.7)\%$ and $(98.7 \pm 0.3)\%$ for muons and electrons respectively [64]. The acceptance-weighted average is $(98.0 \pm 0.3)\%$

The lepton trigger and identification efficiencies measured from the data, and the scalar leptoquark acceptances determined from simulated leptoquark events are combined into average leptoquark detection efficiencies in Table 6.6. The average detection efficiency for scalar leptoquark pairs is 0.0286% (0.962%) for $M_{LQ} =$ 50 GeV/c^2(150 GeV/c^2). The detection efficiencies for vector leptoquark pairs are are given by the product of efficiencies in Table 6.6 and the scale factors given in Table 6.3. The uncertainties in the leptoquark detection efficiencies are discussed in the next section.

LQ Mass	50	75	100	125	150	175	200	225	250
Average ε_{LQ}, %	0.0286	0.160	0.380	0.657	0.962	1.21	1.35	1.57	1.69

Table 6.6: The detection efficiency for scalar leptoquarks. The detection efficiency shown here is the luminosity-weighted average of the ε^i_{LQ} since the CMX detector is used only for Run 1B data. The uncertainties in ε_{LQ} are discussed in the systematic errors section.

6.2 Systematic Errors

The leptoquark detection efficiencies are only estimates based on quantities determined from simulated leptoquark event samples or measured from data. Any uncertainties in ε_{LQ} and the integrated luminosity measurement affect the bounds on the leptoquark pair production cross section discussed in the next chapter. In the remainder of this chapter, the most significant uncertainties in total acceptance $\mathcal{A}_{LQ}$ are estimated.

6.2.1 Initial State Radiation

The number of jets requirement reduces the background from $Z \rightarrow \tau\tau$ while accepting a large fraction of leptoquark events. Presumably the extra jets are arise from the hadronization of the two b quarks from the leptoquark pair decays. However, the radiation of gluons from the initial or final state partons can increase the jet multiplicity and thus increase the efficiency of the number of jets requirement. However, the presence of additional jets can increase the probability of accidental overlap of a jet and the lepton or taujet. This can change the efficiency of the isolation requirements.

ISAJET simulates the initial state radiation using a phenomenological model developed by Sjöstrand [84, 85]. This model gives the procedure for embedding the

hard scattering partons, gg or $q\bar{q}$, into the $p\bar{p}$ pair. It employs the so-called *backward evolution* prescription to generate a parton shower cascade. The systematic uncertainty associated with this model is estimated by regenerating leptoquark samples with no initial state radiation. To determine the 95% confidence level bounds on the cross section for leptoquark pairs, the average acceptance, $\mathcal{A}_{avg}$, of the nominal ISAJET sample (radiation ON) and of the radiation-off sample is used. The systematic uncertainty is taken to be half of the difference in acceptances between the nominal ISAJET and radiation-off samples. This ranges from 10.5% for 50 GeV LQ's to around 4% at high mass.

The uncertainties associated with the initial state radiation modeling are expected to be larger than that of the final state radiation [86], so only the former is considered here.

6.2.2 Choice of Q^2 Scale

In the leptoquark simulation, the Q^2 scale enters in the structure functions and the matrix element $\alpha_s(Q^2)$. Also the Q^2 scale affects the amount of radiation in the initial state parton cascade. For the $2 \rightarrow 2$ process here, ISAJET takes as the nominal Q^2 the expression in Equation 6.6:

$$Q_0^2 = \max\left(\frac{2\,\hat{s}\,\hat{t}\,\hat{u}}{\hat{s}^2+\hat{t}^2+\hat{u}^2}, 4M_{LQ}^2\right) \tag{6.6}$$

where $\hat{s}$, $\hat{t}$, and $\hat{u}$ are the Mandelstam variables associated with the hard scatter. The numerical results become less sensitive to the particular choice of Q^2 scale when higher order calculations are used. The acceptances here can depend on the Q^2 choice since the cross section calculation for this process in ISAJET is only leading order. The systematic uncertainty for the choice of Q^2 scale is estimated by determining the acceptance from leptoquark samples generated with two other Q^2 choices: $Q_0^2 \times 4$ and $Q_0^2 \div 4$. The uncertainty is taken to be the maximum change in acceptance from the

samples generated with the nominal choice of Q_0^2. This systematic is 18.6% (2.5%) for 50 GeV/c^2 (250 GeV/c^2) mass leptoquarks.

6.2.3 Energy Scale Uncertainty

The calorimeter response to single particles – electrons and charged hadrons – has been calibrated at dedicated test beams, and *in situ* during the collider runs. These calibrations are used to set the response in the simulation and to determine the absolute energy scales applied to the data during reconstruction. Uncertainties in the calorimeter energy scale propagate to uncertainties in the leptoquark detection efficiency.

In this analysis the response to hadrons impacts not only the taujet E_t and jet multiplicity requirements, but also the measurement of $\phi(\not\!\!E_t)$ and $\Delta\phi(\ell, \not\!\!E_t)$. Therefore to estimate this uncertainty each leptoquark Monte Carlo sample (ISAJET samples with nominal initial state radiation) is resimulated in two additional passes, increasing and decreasing the calorimeter response within the one sigma upper and lower uncertainties in the detector response to single charged particles. The systematic uncertainty is taken to be the average change in acceptance between nominal and the $\pm 1\sigma$ samples. This systematic is 13.8(3.5)% for a 50(175) GeV/c^2 leptoquark. The 175 GeV/c^2 systematic as the systematic for the higher masses.

6.2.4 Integrated Luminosity

The uncertainties in the total integrated luminosity translate to an uncertainty in the number of expected leptoquark events. For Run 1A the uncertainty in $\int \mathcal{L} dt$ is 3.6% [96]. The best estimate for the uncertainty on $\int \mathcal{L} dt$ for Run 1B is 8% [97]. The luminosity weighted average of 3.6% and 8% is 6.9%, and this is taken to be the systematic uncertainty due to the luminosity uncertainty.

6.2.5 Structure Functions

The choice of structure functions affects the total cross section, the relative contributions from the gg and $q\bar{q}$ subprocesses, and the development of the initial state parton shower. This systematic uncertainty is estimated from the structure functions systematic in the CDF second generation leptoquark search (Table 15 from Ref. [30]), $\sim 3\%$ at low mass to $\sim 1\%$ at high mass. The structure function systematic uncertainties in Ref. [30] were determined by comparing the leptoquark detection efficiencies obtained using the CTEQ2pM and MRS(A) structure functions.

6.2.6 Tau Branching Ratios

The uncertainties in the tau branching ratios can affect the uncertainty in acceptance. To investigate the size of this effect, we run 10K experiments for each leptoquark mass and decay mode where for each trial we modify the branching ratios according to a Gaussian distribution centered on the nominal value with a width given by the errors from the Particle Data Group world averages [40]. We use the distribution of decay modes passing all leptoquark requirements to recalculate the acceptance for each trial. We fit the distribution of the new acceptances to Gaussian, and take the largest width to be the systematic error. This systematic uncertainty amounts to 0.3%.

6.2.7 Sample Statistics

There is a statistical uncertainty in the acceptance from the limited Monte Carlo sample sizes. In this analysis the average acceptance of nominal radiation and radiation-off ISAJET leptoquark samples is used as the central value for the acceptance. The associated statistical uncertainty is then

$$\delta\mathcal{A}_{avg}^{stat} = \frac{1}{2}\sqrt{(\delta\mathcal{A}_{nom}^{stat})^2 + (\delta\mathcal{A}_{off}^{stat})^2} \tag{6.7}$$

where $\delta\mathcal{A}_{nom}^{stat}$ and $\delta\mathcal{A}_{off}^{stat}$ are the statistical uncertainties in the nominal and radiation-off acceptances estimated from the ISAJET leptoquark samples. This systematic ranges from 5.9% for the 50 GeV/c^2 sample to 2.3% for the high mass samples.

6.2.8 ε-Scaling Procedure for Vector Leptoquarks

The efficiencies for vector leptoquarks have been scaled from the scalar leptoquark efficiencies using ratios of generator-level acceptances. The systematic associated with this procedure is estimated by comparing the generator-level results with the results from smaller but fully-simulated samples. The size of the systematic is 7% for $\kappa = 0$ (non-gauge) vector leptoquarks and 10% for $\kappa = 1$ (gauge) vector leptoquarks. This is added in quadrature with the statistical uncertainties on the generator-level ratios to get the additional systematic error in the vector leptoquark detection efficiencies.

6.2.9 Total Systematic Error

The total systematic error for scalar leptoquarks is obtained by adding in quadrature the errors in rows 1–7 of Table 6.7. The systematic error ranges from 27% for $M_{LQ} =$ 50 GeV/c^2 to around 10% at high mass.

The systematic uncertainties in rows 1–7 are taken to apply to the vector leptoquarks as well. This is a reasonable assumption since the systematic errors decrease in general with increasing leptoquark mass. The average leptoquark p_t, $< p_t >$, scales with leptoquark mass. The $< p_t >$ for vector leptoquarks is larger than that of scalar leptoquarks with the same mass (Figure 6.4). Therefore the uncertainties listed in rows 1–7 are conservative estimates for the vector leptoquark uncertainties. For a given leptoquark mass, the total systematic uncertainties for the vector leptoquarks are obtained by adding in quadrature the scalar leptoquark systematic uncertainty and the efficiency scaling systematic for the appropriate vector leptoquark. These are listed in Table 6.7.

Systematic Uncertainties, %									
LQ Mass	50	75	100	125	150	175	200	225	250
1) Initial State Rad.	10.5	8.6	6.4	0.1	3.6	4.0	3.7	3.2	4.5
2) Q^2 Scale	18.6	5.5	9.5	7.5	2.8	5.5	2.5	5.6	2.3
3) Calor. Response	13.8	8.3	11.1	10.9	6.0	3.5	3.5	3.5	3.5
4) Luminosity	6.9	6.9	6.9	6.9	6.9	6.9	6.9	6.9	6.9
5) Structure Function	3.4	3.0	0.5	1.3	1.0	0.7	1.3	1.3	1.3
6) τ Branching Ratios	0.3	0.3	0.3	0.3	0.3	0.3	0.3	0.3	0.3
7) MC Statistics	5.6	3.4	2.8	2.8	2.3	2.3	2.1	2.1	2.2
8) Vector ε Scaling, $\kappa = 0$	13.0	7.6	7.3	7.3	7.3	7.3	7.3	7.3	7.3
9) Vector ε Scaling, $\kappa = 1$	17.2	10.8	10.4	10.2	10.2	10.2	10.2	10.2	10.2
Total, Scalar	27.1	15.5	17.6	15.2	10.5	10.6	9.2	10.4	9.6
Total, Vector, $\kappa = 0$	30.1	17.3	19.1	16.9	12.8	12.8	11.8	12.7	12.1
Total, Vector, $\kappa = 1$	32.2	18.9	20.5	18.3	14.7	14.7	13.8	14.6	14.0

Table 6.7: The percent systematic uncertainties in the the experimental cross section for leptoquark pair production. The top rows (1 – 7) are the systematics common to scalar and vector leptoquarks. The "ε scaling" systematics apply only to vector leptoquarks.

Chapter 7

Results

The search described in Chapter 4 results in zero candidate events passing the leptoquark selection criteria. With no events observed, upper bounds on leptoquark pair production cross section times branching fraction can be derived. Using these bounds and the theoretical predictions for leptoquark pair production, limits are placed on the leptoquark mass.

7.1 Bounds on Leptoquark Cross Section

The 95% confidence level (C.L.) upper limit on the leptoquark pair production cross section, σ_{LQ} is given by

$$\sigma_{LQ} = \frac{N_{95\%}}{\beta^2 \times \sum_i \varepsilon^i_{LQ} (\int \mathcal{L} dt)^i} \tag{7.1}$$

where $\beta = \mathrm{BR}(\mathrm{LQ} \rightarrow \tau b)$. ε^i_{LQ} is the total efficiency for detecting leptoquark pair events which produce a high-p_t lepton. The superscript i represents central electrons, CMU-only muons, CMUP muons, and CMX muons. The $(\int \mathcal{L} dt)^i$'s are the integrated luminosities of the lepton data sets used. The $(\int \mathcal{L} dt)^i$'s vary slightly among the different lepton types due to the removal of runs with detector or trigger problems. Also high-p_t CMX muons from Run 1A are not used. $N_{95\%}$ is the 95% C.L. upper limit on the mean number of leptoquark events expected given zero events observed

in the data. Since each ε^i_{LQ} depends on the leptoquark mass, spin, and κ in the case of vector leptoquarks, σ_{LQ} will depend on these parameters too.

In the absence of systematic uncertainties, $N_{95\%}$ is given by Poisson statistics: $N_{95\%} = 3.0$. Since there are uncertainties in the detection efficiencies $\sum_i \varepsilon^i_{LQ}$ and the $(\int \mathcal{L}dt)^i$, there is an associated uncertainty in the mean number of leptoquark events expected. This acts to increase the upper limit $N_{95\%}$.

The procedure for extracting $N_{95\%}$ in the presence of systematic uncertainties is as follows. The total uncertainties listed in Table 6.7 are taken to be the systematic error in $\sum_i \varepsilon^i_{LQ}(\int \mathcal{L}dt)^i$. For a given mass and leptoquark type, the total systematic uncertainty, $\mathcal{U}$, is used as the fractional standard deviation of a modified Gaussian distribution, $G(x;\mu,s)$. The mean of the Gaussian, μ, is the the upper limit $N_{95\%}$. The standard deviation is $s \equiv \mathcal{U} \times \mu$. This represents the uncertainty in the mean number of leptoquark events expected. The distribution $G(x;\mu,s)$ is given by

$$G(x;\mu,s) = A(\mu,s)\exp\left[-\frac{(x-\mu)^2}{2s^2}\right] \tag{7.2}$$

where the term $A(\mu,s)$ is chosen to fix the normalization of G:

$$\int_0^\infty G(x;\mu,s)dx = 1 \tag{7.3}$$

The distribution $G(x;\mu,s)$ is convoluted with the Poisson probability distribution, $\mathcal{P}(x,\mathcal{N}_{obs})$, for the number of events observed, $\mathcal{N}_{obs}$.

$$\mathcal{P}(x;\mathcal{N}_{obs}) = \sum_{n=0}^{\mathcal{N}_{obs}} \frac{x^n}{n!}e^{-x} \tag{7.4}$$

The convolution of the two distributions yields the modified Poisson probability distribution, $\mathcal{P}_{mod}$, in Equation 7.5 [87, 88].

$$\mathcal{P}_{mod} = \int_0^\infty G(x;\mu,s)\sum_{n=0}^{\mathcal{N}_{obs}} \frac{x^n}{n!}e^{-x}dx \tag{7.5}$$

The convolution smears the mean of $\mathcal{P}(x;\mathcal{N}_{obs})$ by the modified Gaussian $G(x;\mu,s)$ where $s = \mathcal{U} \times N_{95\%}$ and $\mu = N_{95\%}$. Equation 7.5 can be used to numerically determine the upper limit for an arbitrary confidence level [89]. $N_{95\%}$ is found by setting $\mathcal{P}_{mod} = 1 - \text{C.L.} = 0.05$

The upper limit $N_{95\%}$ depends only on the systematic uncertainties in the detection efficiencies and in the integrated luminosity. The uncertainties in detection efficiencies depend on the type of leptoquark (scalar or vector) and the leptoquark mass. The total systematic uncertainties and values for $N_{95\%}$ are listed in Table 7.1. A total uncertainty of 30% (10%) yields a 95% C.L. upper limit of 3.53 (3.04) events for zero events observed in the data.

The upper limits on the leptoquark production cross section times β^2 ($\beta = BR(\text{LQ} \to \tau b)$) are calculated using Equation 7.1. The results are listed in Table 7.1 for the three types of leptoquarks considered: scalar, vector $\kappa = 0$, and vector $\kappa = 1$.

7.2 Bounds on Leptoquark Mass

Also listed in Table 7.1 are the theoretical cross sections for leptoquark pair production, σ_{th}. These cross section calculations were discussed in Chapter 1. The scalar leptoquark pair cross sections are calculated with the ISAJET Monte Carlo program using the the Q^2 scale from Equation 6.6 in α_s and the parton distribution functions. This is the default choice in ISAJET. The vector leptoquark cross sections are calculated using partonic cross sections supplied by the authors of Ref. [38, 39]. The partonic cross sections are integrated using the PYTHIA program [82] using the $Q^2 = \hat{s}$ as the momentum transfer in the calculation of α_s and the parton distribution functions. The CTEQ2L[90] parton distribution functions were used in the cross section calculations shown in Table 7.1 and Figures 7.1–7.2.

The 95% C.L. upper limits on the cross section for leptoquark pair production are shown in Figure 7.1 assuming a branching ratio $\beta = 100\%$. The theoretical

SCALAR LEPTOQUARKS									
LQ Mass	50	75	100	125	150	175	200	225	250
σ_{th}, pb	315	44	9.8	2.9	1.0	0.39	0.16	0.070	0.031
N_{exp}	6.3	4.9	2.6	1.3	0.67	0.33	0.15	0.077	0.037
Syst. Err, %	27.2	15.5	17.6	15.2	10.5	10.6	9.3	10.4	9.6
$N_{95\%}$	3.42	3.11	3.15	3.10	3.05	3.05	3.03	3.04	3.04
$\beta^2 \times \sigma_{LQ}$, pb	172	27.8	11.8	6.73	4.52	3.60	3.22	2.76	2.56
$\beta_{95\%}^{min}$	0.74	0.79	1	1	1	1	1	1	1

VECTOR LEPTOQUARKS, $\kappa = 0$									
LQ Mass	50	75	100	125	150	175	200	225	250
σ_{th}, pb	3750	422	84	23	7.6	2.8	1.1	0.47	0.20
N_{exp}	170	52	22	11	4.7	2.2	0.97	0.48	0.22
Syst. Err, %	30.1	17.3	19.1	16.9	12.8	12.8	11.8	12.7	12.1
$N_{95\%}$	3.55	3.14	3.18	3.13	3.07	3.07	3.06	3.07	3.07
$\beta^2 \times \sigma_{LQ}$, pb	77.4	25.3	12.1	6.86	4.89	3.81	3.49	2.99	2.83
$\beta_{95\%}^{min}$	0.14	0.24	0.38	0.55	0.80	1	1	1	1

VECTOR LEPTOQUARKS, $\kappa = 1$									
LQ Mass	50	75	100	125	150	175	200	225	250
σ_{th}, pb	19450	2440	506	138	44	16	6.2	2.5	1.0
N_{exp}	1210	361	149	67	30	13	5.9	2.7	1.2
Syst. Err, %	32.2	18.9	20.5	18.3	14.7	14.7	13.8	14.6	14.0
$N_{95\%}$	3.65	3.17	3.21	3.16	3.09	3.09	3.08	3.09	3.09
$\beta^2 \times \sigma_{LQ}$, pb	58.6	21.4	10.9	6.46	4.54	3.65	3.27	2.93	2.76
$\beta_{95\%}^{min}$	0.055	0.094	0.15	0.22	0.32	0.48	0.73	1	1

Table 7.1: A summary of results for leptoquark pair production for each leptoquark type: scalar, non-gauge vector ($\kappa = 0$), and gauge vector ($\kappa = 1$). The theoretical pair production cross section, σ_{th}, is described in the text. The number of events expected in 72 pb^{-1} to satisfy the search criteria, N_{exp}, are shown assuming a branching fraction $\beta = BR(\text{LQ} \rightarrow \tau b) = 100\%$. The systematic uncertainties in the leptoquark detection efficiencies and integrated luminosity are taken from Table 6.7 and are used to calculate $N_{95\%}$, the 95% C.L. upper limit on the mean number of leptoquark events given no candidate events observed in the data. The 95% C.L. experimental bounds on the pair production cross section times branching fraction, $\beta^2 \times \sigma_{LQ}$, are calculated using Equation 7.1, and the 95% C.L. bounds on the branching fraction for LQ $\rightarrow \tau b$, $\beta_{95\%}^{min}$, are calculated using Equation 7.6.

cross sections for the pair production of scalar and vector ($\kappa = 0$ and $\kappa = 1$) leptoquarks are overlaid in this figure. The intersection of the scalar leptoquark theoretical cross section and the corresponding cross section limit gives the mass bounds for scalar leptoquarks assuming $\beta = 100\%$. The scalar leptoquark is constrained to have $M_{LQ} > 94$ GeV/c^2 at the 95% C.L.. The crossing point of the $\kappa = 0$ ($\kappa = 1$) vector leptoquark theoretical cross section and the corresponding cross section upper limit gives the mass bounds for the vector leptoquarks. For $\kappa = 0$ vector leptoquarks, $M_{LQ} > 165$ GeV/c^2 at the 95% C.L. assuming $\beta = 100\%$. For $\kappa = 1$ vector leptoquarks, $M_{LQ} > 220$ GeV/c^2 at the 95% C.L. assuming $\beta = 100\%$. If one leptoquark candidate were observed, the mass bounds on the vector leptoquarks would each be reduced by approximately 10 GeV/c^2 with no background subtraction. In this case, the scalar cross section limits for $M_{LQ} = 50$ GeV/c^2(75 GeV/c^2) would be within $\sim 10\%(5\%)$ of corresponding theoretical cross section. Therefore a background subtraction would be necessary to place more conclusive limits on the scalar leptoquark mass.

The analysis here is based on 72 pb^{-1} of data collected through February, 1995. However the Run 1B data taking period extended through July, 1995, giving a total integrated luminosity of 110 pb^{-1} for Run 1A and Run 1B combined. If this data is included in the leptoquark search and no candidate events are found, then the mass limits for each leptoquark type are expected to increase by 15 GeV/c^2.

Figure 7.2 shows the cross section 95% C.L. upper limits for scalar and both types of vector leptoquarks, assuming $\beta = BR(\text{LQ} \rightarrow \tau b) = 50\%$. The 95% C.L. mass limits for $\kappa = 0$ and $\kappa = 1$ vector leptoquarks are $M_{LQ} > 120$ GeV/c^2 and $M_{LQ} > 178$ GeV/c^2, respectively, for $\beta = 50\%$. In this case, the cross section limit for scalar leptoquark pair production is larger than the corresponding theoretical cross section. Therefore the scalar leptoquark masses are not constrained by this analysis for $\beta = 50\%$. The results for $\beta = 50\%$ listed above assume that the competing leptoquark decay mode(s) is not detected in the $\tau^+\tau^-$ *jet jet* search channel. But

LQ $\rightarrow \tau b$ is the only decay channel available for third generation leptoquarks with $M_{LQ} < M_{top}$. Therefore in the mass range $M_{LQ} < M_{top}$, the branching fraction for LQ $\rightarrow \tau b$ is expected to be 100%[1]. For $M_{LQ} > M_{top}$, the decay channel LQ $\rightarrow \nu_\tau t$ is kinematically accessible, but phase-space suppressed for M_{LQ} near M_{top}.

The cross section limit σ_{LQ} for $\beta = 100\%$ represents the strongest bound on the cross section for leptoquark pairs for a fixed M_{LQ}. Smaller values of β give larger values for the experimental leptoquark pair cross section. Setting $\sigma_{LQ} = \sigma_{th}$ in Equation 7.1 and solving for β gives the minimum branching fraction for which leptoquark pair production is excluded at the 95% C.L. This is given by

$$\beta_{95\%}^{min} = \min\left\{1, \left[\frac{\sigma_{LQ}(\beta = 100\%)}{\sigma_{th}}\right]^{\frac{1}{2}}\right\} \tag{7.6}$$

where $\sigma_{LQ}(\beta = 100\%)$ is the cross section limit from Equation 7.1 with $\beta = 100\%$ and σ_{th} is the theoretical cross section for the same leptoquark type and mass. As mentioned above, the decay LQ $\rightarrow \tau b$ is the only channel available for charge-$\frac{2}{3}$ or charge-$\frac{4}{3}$ third generation leptoquarks with $M_{LQ} < M_{top}$. But for completeness, the values of $\beta_{95\%}^{min}$ as a function of leptoquark mass are listed in Table 7.1 for the three types of leptoquarks considered.

[1]This may be circumvented if the leptoquark couples to more than one quark generation, eg. through CKM mixing. This does not affect the results of this analysis since the mass limits are given for an *assumed* branching fraction.

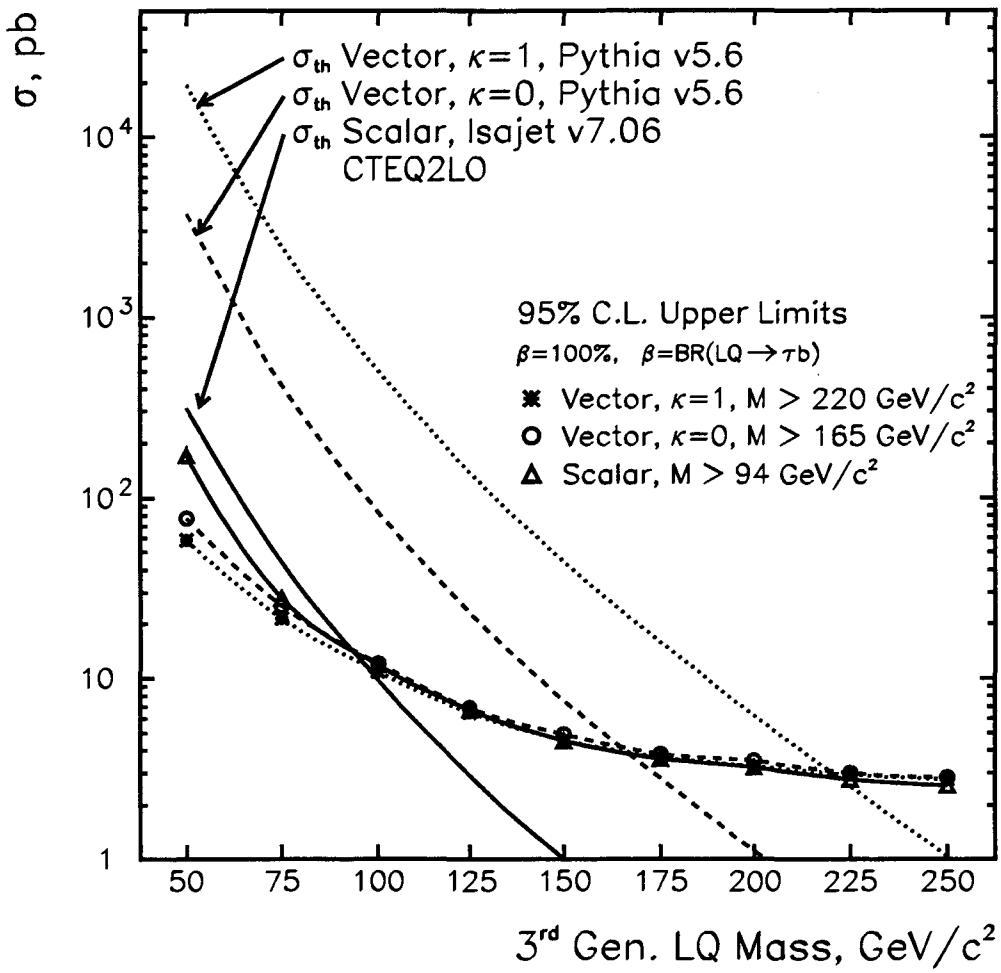

Figure 7.1: The 95% confidence level upper limits on the leptoquark pair production cross section, σ_{LQ}, for $\beta = 100\%$ where $\beta = \mathrm{BR}(\mathrm{LQ} \to \tau b)$. The crossing points of the theoretical cross sections (indicated by the arrows) and experimental cross section bounds (denoted by the symbols) determine the mass limits for each leptoquark type. A charge-$\frac{4}{3}$ leptoquark decaying to $\tau^- \bar{b}$ cannot decay to any other combination of third generation lepton-quark pairs. Also for $M_{LQ} < M_{top}$, $\mathrm{LQ} \to \tau^- b$ is the only decay mode kinematically accessible to a charge-$\frac{2}{3}$ third generation leptoquark. Therefore in both of these two cases, $\beta \equiv 100\%$ is expected. However for $M_{LQ} > M_{top}$, the decay channel $\mathrm{LQ} \to \tau^- b$ is kinematically allowed, but is phase-space suppressed for the leptoquark mass range applicable to this analysis. If the leptoquark quantum numbers and couplings permit the decay $\mathrm{LQ} \to \tau^- b$, then the branching fraction $\beta = \mathrm{BR}(\mathrm{LQ} \to \tau b)$ is expected to be larger than 50% due to the phase-space suppression, but less than 100%.

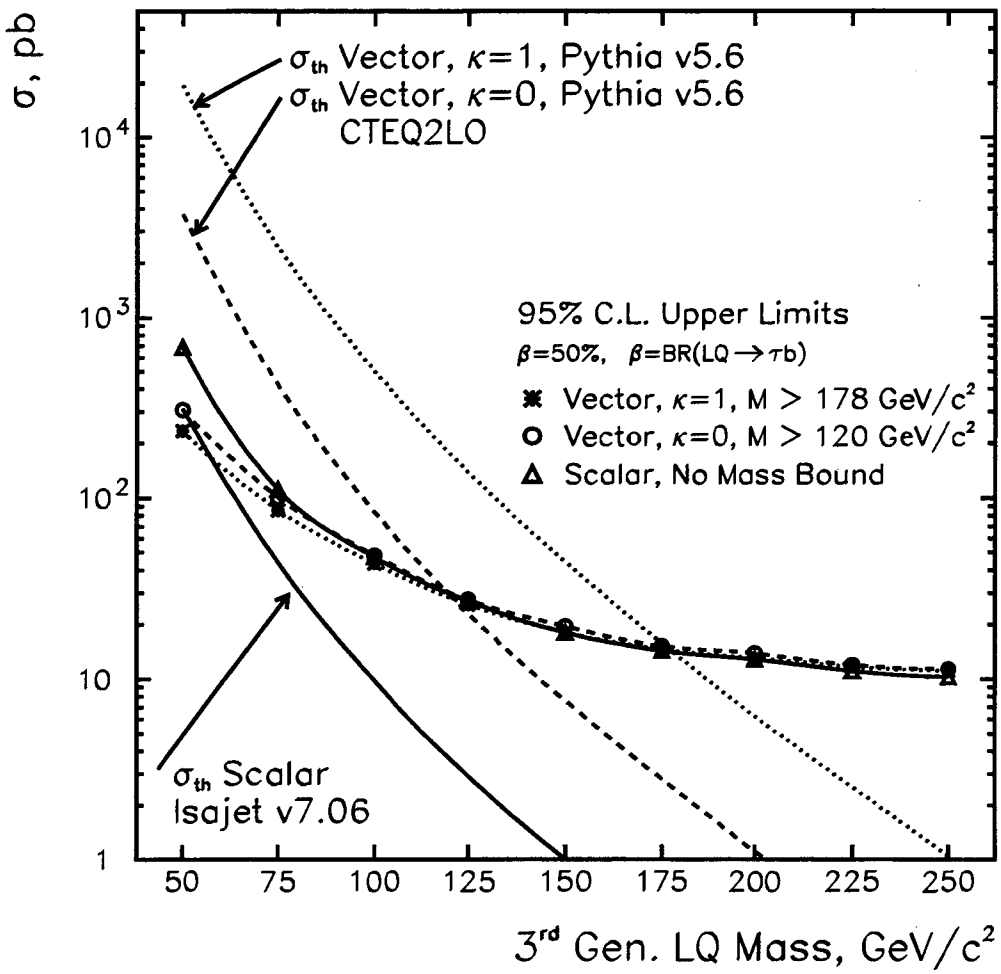

Figure 7.2: The 95% confidence level upper limits on the leptoquark pair production cross section, σ_{LQ}, for β = 50% where β = BR(LQ → τb). The crossing points of the theoretical cross sections (indicated by the arrows) and experimental cross section bounds (denoted by the symbols) determine the mass limits for each leptoquark type. In general, β = 100% is expected for $M_{LQ} < M_{top}$. However, if the leptoquark quantum numbers permit the decay LQ → νt and $M_{LQ} > M_{top}$, then it is expected that 50% < β < 100%. The branching fraction β is not 50% due to phase space suppression of the νt decay channel.

Chapter 8

Conclusions

In summary, a search for third generation leptoquarks has been made using 72 pb^{-1} of data collected with the CDF detector during the 1992–1995 Collider runs. No evidence was found for leptoquarks pair in the $\tau^+\tau^-$ *jet jet* channel. With this result, 95% C.L. upper limits are placed on the pair production cross section times branching fraction for scalar, gauge vector ($\kappa = 1$), and non-gauge vector ($\kappa = 0$) leptoquarks. These limits are summarized in Table 7.1. Using the corresponding theoretical cross sections for pair production, mass limits are placed on each leptoquark type considered. Assuming the branching fraction into τb is 100% ($\beta = \mathrm{BR}(\mathrm{LQ} \to \tau b) = 100\%$), the 95% C.L. masses bounds are: $M_{LQ} > 94$ GeV/c^2 for scalar leptoquarks; $M_{LQ} > 165$ GeV/c^2 for non-gauge ($\kappa = 0$) vector leptoquarks; and $M_{LQ} > 220$ GeV/c^2 for gauge ($\kappa = 1$) vector leptoquarks.

This analysis is the first search for third generation leptoquarks in $p\bar{p}$ interactions. The results for $\beta = 100\%$ represent the highest mass limits on leptoquarks coupling to third generation fermions from a direct search. The mass limits above are expected to increase by $\sim$ 15 GeV/c^2 if the full 110 pb^{-1} of the Run 1A and Run 1B data sets are included and no leptoquark candidate events are observed. Moreover, the results of this search can constrain certain theories of technicolor. In these models, third generation leptoquark pairs may be produced through a resonance in hadron

collisions. This production mechanism is not present in e^+e^- collisions. If this resonance mechanism is incorporated into the present search, the CDF data can provide valuable direct constraints on these models of technicolor.

Bibliography

[1] See for example R. D. Field, *Applications of Perturbative QCD* (Addison–Wesley, Redwood City, 1989)

[2] S.L. Glashow, *Nucl. Phys.* **B22** 579 (1961)

[3] S. Weinberg, *Phys. Rev. Lett.* **19** 1264 (1967)

[4] A. Salam, in *Elementary Particle Theory*, edited by N. Svartholm (Almquist and Wiskell, Stockholm, 1968), p.367

[5] See for example I. J. R. Aitchison and A. J. G. Hey, *Gauge Theories in Particle Physics* (Adam Hilger, Bristol, 1989)

[6] P. Higgs, *Phys. Rev.* **145** 1156 (1966)

[7] J.C. Pati, A. Salam, *Phys. Rev.* **D8** 1240 (1973); J.C. Pati, A. Salam, *Phys. Rev. Lett.* **31** 661 (1973); J.C. Pati, A. Salam, *Phys. Rev.* **D10** 275 (1973)

[8] H. Georgi, S.L. Glashow, *Phys. Rev. Lett.* **32** 438 (1974)

[9] B. Schrempp and F. Schrempp, *Phys. Lett.* **B153** 101 (1985)

[10] L. F. Abbott and E. Farhi, *Phys. Lett.* **B101** 69 (1981)

[11] J. C. Pati, *Phys. Lett.* **B228** 228 (1989)

[12] E. Farhi, L. Susskind, *Phys. Rep.* **74** 277 (1981)

[13] E. Eichten, I. Hinchliffe, K.D. Lane, C. Quigg, *Phys. Rev.* **D34** 1547 (1986)

[14] S. F. King, *Rep. Prog. Phys.* **58**, 263, (1995)

[15] G. Bhattacharyya, J. Ellis, K. Sridhar, *Phys. Lett.* **B336** 100 (1994); (E) **B338**, 522, (1994)

[16] J. K. Mizukoshi, O. J. P. Èboli, M. C. Gonzalez-Garcia, *Nucl. Phys.* **B444** 20 (1995); O. J. P. Èboli, hep-ph/9508342

[17] S. Davidson, D. Bailey, B. A. Campbell, *Zeit. fur Physik* **C61** 613 (1994)

[18] W. Buchmüller, D. Wyler, *Phys. Lett.* **B177** 37 (1986)

[19] G. Valencia and S. Willenbrock, *Phys. Rev.* **D50** 6843 (1994)

[20] S. Abachi, *et al.* (DØ Collaboration), *Phys. Rev. Lett.* **72** 965 (1994)

[21] S. Abachi, *et al.* (DØ Collaboration), *Phys. Rev. Lett.* **75** 3618 (1995)

[22] F. Abe, *et al.* (CDF Collaboration), *Phys. Rev.* **D48** 3939 (1993)

[23] S. Park, (CDF Collaboration), Report No. Fermilab-Conf-/95/155-E, (1995)

[24] M. Derrick, *et al.* (ZEUS Collaboration), *Phys. Lett.* **B306** 173 (1993)

[25] S. Aid, *et al.* (H1 Collaboration), *Phys. Lett.* **B369** 173 (1996)

[26] B. Adeva, et al. (L3 Collaboration), *Phys. Lett.* **B261** 169 (1991)

[27] G. Alexander, et al. (OPAL Collaboration), *Phys. Lett.* **B263** 123 (1991)

[28] P. Abreu, et al. (DELPHI Collaboration), *Phys. Lett.* **B316** 620 (1993)

[29] D. Decamp, et al. (ALEPH Collaboration), *Phys. Rep.* **216** 253 (1992)

[30] S. Park, CDF Note 2648, version 3.5, (1995)

[31] W. Buchmüller, R. Rückl, D. Wyler, *Phys. Lett.* **B191** 442 (1987)

[32] M. Leurer, *Phys. Rev.* **D49** 333 (1994)

[33] M. Leurer, *Phys. Rev.* **D50** 536 (1994)

[34] J. L. Hewett, S. Pakvasa, *Phys. Rev.* **D37** 3165 (1988)

[35] J. L. Hewett, T. G. Rizzo, *Phys. Rev.* **D36** 3367 (1987)

[36] G. V. Borisov, Yu. F. Pirogov, K. R. Rudakov, *Zeit. fur Physik* **C36** 217 (1987)

[37] J. E. Cieza Montalvo, O. J. P. Éboli, *Phys. Rev.* **D50** 331 (1994)

[38] J. L. Hewett, T. G. Rizzo, S. Pakvasa, H. E. Haber, A. Pomarol, Report No. ANL-HEP-CP-93-52 (hep-ph/9310361), (1993)

[39] A. Djouadi, J. Ng, T. G. Rizzo, Report No. SLAC-PUB-95-6772 (hep-ph/9504210), (1995)

[40] L. Montanet, et al., *Phys. Rev.* **D50** 1173 (1994), and 1995 off-year partial update for the 1996 edition (URL: http://pdg.lbl.gov/)

[41] T. Rizzo, private communication

[42] F. Abe, *et al.*, (CDF Collaboration), *Nucl. Instr. and Meth.* **A 271**, 387, (1988) and references therein.

[43] F. Snider, *et al.*, *Nucl. Instr. and Meth.* **A 268**, 75, (1988) This is the reference for the previous generation of this device. The replacement for Run 1A and Run 1B data taking has more modules (28 rather than 8), each with a shorter drift length, but is similar otherwise.

[44] D. Amidei, *et al.*, *Nucl. Instr. and Meth.* **A 350**, 73, (1994)

[45] D. Amidei, *et al.*, *Nucl. Instr. and Meth.* **A 360**, 137, (1995)

[46] F. Bedeschi, *et al.*, *Nucl. Instr. and Meth.* **A 268**, 50, (1988)

[47] W. F. Badgett, Ph.D. dissertation, University of Michigan, (1994)

[48] L. Balka, *et al.*, *Nucl. Instr. and Meth.* **A 267**, 272, (1988)

[49] S. Bertolucci, *et al.*, *Nucl. Instr. and Meth.* **A 267**, 301, (1988)

[50] F. Abe, *et al*, (CDF Collaboration) *Phys. Rev.* **D52** 4784 (1995).

[51] Y. Fukui, *et al.*, *Nucl. Instr. and Meth.* **A 267**, 280, (1988)

[52] W. Carithers, *et al.*, *Procedings of the Gas Sampling Calorimetry Workshop II*, Batavia, Illinois, (1985)

[53] G. Brandenburg, *et al.*, *Nucl. Instr. and Meth.* **A 267**, 257, (1988)

[54] S. Cihangir, *et al.*, *Nucl. Instr. and Meth.* **A 267**, 249, (1988)

[55] K. Byrum, *et al.*, *Nucl. Instr. and Meth.* **A 268**, 46, (1988)

[56] G. Ascoli, *et al.*, *Nucl. Instr. and Meth.* **A 268**, 33, (1988)

[57] F. Abe, *et al*, (CDF Collaboration) *Phys. Rev.* **D50** 5518 (1994)

[58] F. Abe, *et al*, (CDF Collaboration) *Phys. Rev.* **D50** 5535 (1994)

[59] F. Abe, *et al*, (CDF Collaboration) *Phys. Rev.* **D50** 5550 (1994)

[60] T. LeCompte, T. Liss, A. Martin, CDF Note 2367, (1993)

[61] D. Glenzinski, P. Schlabach, CDF Note 2954, (1995)

[62] T. LeCompte, D. Glenzinski, CDF Note 2985, (1995)

[63] C. Campagnari, CDF Note 2821, (1994)

[64] R. Roser, T. Liss, CDF Note 3442, (1996)

[65] K. Byrum and A. B. Wicklund, CDF Note 3120, (1995)

[66] F. Paige and S.D. Protopopescu, BNL Report No. 38034, (1986) ISAJET V7.06 (corrected) is used; F. Paige, private communication.

[67] M. Shapiro, et al., CDF Note 1810, (1992)

[68] F. Abe, *et al*, (CDF Collaboration) *Phys. Rev.* **D52** 2624 (1995)

[69] F. Abe, *et al*, (CDF Collaboration), *Phys. Rev. Lett.* **76** 3070 (1996)

[70] S. A. Hauger, Ph.D. dissertation, Duke University, (1995)

[71] N. Eddy, *et al.*, CDF Note 3608, (1996)

[72] T. Liss and R. Roser, CDF Note 3481, (1996)

[73] J. Ohnemus, *Phys. Rev.* **D44** 1403 (1991)

[74] J. Ohnemus, *Phys. Rev.* **D44** 3477 (1991)

[75] J. Ohnemus and J. F. Owens, *Phys. Rev.* **D43** 3626 (1991)

[76] F. Abe, *et al*, (CDF Collaboration), *Phys. Rev. Lett.* **71** 2396 (1993)

[77] F. Abe, *et al*, (CDF Collaboration), *Phys. Rev.* **D50** 2966 (1994)

[78] F. Abe, *et al*, (CDF Collaboration), *Phys. Rev. Lett.* **74** 2626 (1995)

[79] S. Abachi, *et al*, (DØ Collaboration), *Phys. Rev. Lett.* **74** 2632 (1995)

[80] Fotis Ptohos, private communication

[81] F. Abe, *et al*, (CDF Collaboration), *Phys. Rev. Lett.* **70** 4043 (1993)

[82] T. Sjöstrand, Report No. CERN-TH-6488/92 (1992) (URL: http://wwwcn.cern.ch/asdoc/pythia_html3/pythia57.html) PYTHIA V5.6 is used.

[83] G. Altarelli and G. Parisi, *Nucl. Phys.* **B127** 298 (1977)

[84] T. Sjöstrand, *Phys. Lett.* **B157** 321 (1985)

[85] M. Bengtsson, T. Sjöstrand, M. van Zijl, *Zeit. fur Physik* **C32** 67 (1986)

[86] Top Cross Sections and Branching Ratios Working Group, CDF Note 3403, (1995)

[87] G. Zech, *Nucl. Instr. and Meth.* **A 277**, 608, (1989)

[88] T. Chikamatsu, *et al.*, CDF Note 1975, (1993)

[89] The 95% C.L. upper limits $N_{95\%}$ are calculated using FORTRAN routines supplied by S. Park.

[90] James Botts et al. (CTEQ Collaboration), *Phys. Lett.* **B304** 159 (1993)

[91] C. Loomis, CDF Note 2796, (1994)

[92] J. Jadach, J.H. Kuhn, Z. Was, *Comput. Phys. Commun.* **64**, 275, (1991)

[93] A. J. Roodman, Ph.D. dissertation, University of Chicago, (1991)

[94] C. P. Jessop, Ph.D. dissertation, Harvard University, (1993)

[95] F. Abe, *et al.*, Report No. FERMILAB-PUB-96/004-E., (1996), submitted to Phys. Rev. D

[96] S. Belforte, P. Derwent, J. Marriner, C. Grosso-Pilcher, CDF Note 2361, (1994)

[97] Grosso-Pilcher, D. Cronin-Hennessy, A. Beretvas, A. Byon-Wagner, CDF Note 3021, (1995)

[98] G. Ascoli, *et al.*, *Nucl. Instr. and Meth.* **A 269**, 63, (1988)

[99] D. Amidei, *et al.*, *Nucl. Instr. and Meth.* **A 269**, 51, (1988)

[100] G. W. Foster, *et al.*, *Nucl. Instr. and Meth.* **A 269**, 93, (1988)

[101] J. T. Carrol, *et al.*, *Nucl. Instr. and Meth.* **A 300**, 552, (1991)

[102] M. Gold, CDF Note 912, (1989)

[103] D. Gerdes, CDF Note 2903, (1995)

[104] G. Marchesini and B. R. Webber, *Nucl. Phys.* **B238** 1 (1984); G. Marchesini and B. R. Webber, *Nucl. Phys.* **B310** 461 (1988)

[105] F. A. Berends, W. T. Giele, H. Kuijf, and B. Tausk, *Nucl. Phys.* **B357** 32 (1991)

[106] J. Lewis and P. Avery, CDF Note 2724 (1994)